THE COMMISSIONING OF FTS-2

SHERIF ABDELAZIM
Bachelor of Science, Cairo University, 2007

A Thesis
Submitted to the School of Graduate Studies
of the University of Lethbridge
in Partial Fulfillment of the
Requirements for the Degree

MASTER OF SCIENCE

Department of Physics and Astronomy
University of Lethbridge
LETHBRIDGE, ALBERTA, CANADA

THE COMMISSIONING OF FTS-2

SHERIF ABDELAZIM

Date of Defence: December 12, 2014

Dr. David A. Naylor Supervisor	Professor	Ph.D.
Dr. Adriana Predoi-Cross Thesis Examination Committee Member	Professor	Ph.D.
Dr. René T. Boeré Thesis Examination Committee Member	Professor	Ph.D.
Dr. Behnam Sayed-Mahmoud Chair, Thesis Examination Committee	Associate Professor	Ph.D.

Dedication

To whom my life is devoted, and existence lies therein.

Abstract

Despite that over half the energy emitted by the universe falls in the sub-millimetre wavelength region, and the fact that sub-millimetre astronomy enables the study of star formation, it remains an unexplored field. This is due to the low transmittance of the atmosphere and the complexity of the instrumentation. However, recent advances in technology have resulted in instruments that can explore this waveband. One such instrument, FTS-2, is a Fourier transform spectrometer that has been developed for use with a new bolometric camera SCUBA-2. FTS-2 will provide wide field imaging spectroscopy at sub-millimetre wavelengths.

This thesis presents the current performance of FTS-2 based on the results obtained from commissioning. As with the application with any new technology, unforeseen issues emerged. The thesis identifies several issues and introduces potential solutions. Although limited astronomical data were obtained, spectra of Venus have been analysed, and provide an indication of the potential of FTS-2.

Acknowledgments

There are number of people whom I would like to thank. First and foremost Dr. David Naylor for taking a chance on a stranger and offering me to be a graduate student under his tutelage, which afforded me the opportunity to grow as a critical thinker and a dedicated student. I am also grateful for his patience and for the endless hours he spent proofreading for this thesis to turn out the way it did, which was not easy.

I must thank the remainder of my committee members as well, Dr. Adriana Predoi-Cross and Dr. René. Boeré, who were very supportive, understanding and encouraging over the course of my program.

I must also thank the FTS-2 group members, Brad Gom for his guidance and for imparting to me some of his vast knowledge of IDL, and Matt Sherwood for his patience and cooperation.

I would also like to thank my friends and colleagues, whom will be ordered not according to their significance in my life: Gibion Makiwa for all his help and advice even before I come here from his help in finding me a home to proofreading my thesis, Ian Veenendaal, Matthijs van der Wiel and Grace Trimboli for being great friends to me and introducing me to different aspects of life, Vince Weiler, and Abenezer for their support.

I would also like to thank my comrade Tanner Heggie for his help and support, who was an ideal friend to work with, and I was lucky to share the office with him. At last but not the least, I thank my friend Mohamed Hassan for being there for me since I came here. Finally I am especially grateful for my family, Marwa and my parents, for all the support that they gave me, and for being by my side throughout the whole journey and for what is yet to come, especially with the new member of the family, Sirage.

Contents

Approval/Signature Page ii

Contents vi

List of Tables viii

List of Figures x

Acronyms xvii

1 Introduction 1
- 1.1 Sub-millimetre astronomy . . . 1
- 1.2 The James Clerk Maxwell Telescope . . . 8
- 1.3 Sub-millimetre Common-User Bolometer Array-2 . . . 9
- 1.4 Bolometer . . . 11
- 1.5 Transition Edge Sensor (TES) . . . 13
- 1.6 Superconducting Quantum Interface Device (SQUID) . . . 15
- 1.7 Fourier transform spectrometer (FTS-2) . . . 17

2 Data Processing Challenges 22
- 2.1 Overview . . . 22
- 2.2 Data calibration . . . 23
  - 2.2.1 Non-linearity . . . 23
  - 2.2.2 Calibration procedure . . . 27
  - 2.2.3 Results . . . 28
  - 2.2.4 Data calibration challenges . . . 29
- 2.3 Cosmic rays . . . 31
  - 2.3.1 Introduction . . . 31
  - 2.3.2 Procedure . . . 32
  - 2.3.3 Results . . . 33
  - 2.3.4 The challenges of cosmic rays correction . . . 34
- 2.4 Flux jumps . . . 34
  - 2.4.1 Introduction . . . 34
  - 2.4.2 Procedure . . . 36
  - 2.4.3 Results . . . 40
  - 2.4.4 Challenges to the flux jump correction . . . 41
- 2.5 Conclusions . . . 44

3 The Spectral Response of SCUBA-2 **46**
3.1 Introduction . . . 46
3.2 Determining the Spectral Response of SCUBA-2 . . . 49
3.3 SCUBA-2 bias settings . . . 51
3.3.1 The first set of observation . . . 51
3.3.2 The second set of observation . . . 53
3.3.3 Non-linearity . . . 54
3.3.4 The signal-to-noise ratio . . . 58
3.4 Determining the spectral response function . . . 60
3.4.1 Procedure . . . 60
3.4.2 Spectral Response Stability . . . 64
3.4.3 Comparison of the measured Spectral Response Function (SRF) with the theoretical predictions . . . 66
3.5 Application of the spectral response function . . . 68
3.6 Conclusion . . . 72

4 FTS-2 Observation of Venus **73**
4.1 Introduction . . . 73
4.2 Venus temperature . . . 78
4.3 Using Venus to probe the atmosphere of Earth . . . 82
4.3.1 Absorption Lines . . . 82
4.3.2 Ozone and molecular oxygen column abundance in the atmosphere 86
4.4 Venus absorption lines . . . 95
4.4.1 Introduction . . . 95
4.4.2 Absorption features of Venus . . . 98
4.4.3 Carbon monoxide in the Venusian atmosphere . . . 101

5 Conclusion and Future Work **104**
5.1 Future work . . . 105

A Physical constants **106**

Bibliography **107**

List of Tables

1.1 The properties of Submillimetre Common-User Bolometer Array (SCUBA) and Submillimetre Common-User Bolometer Array-2 (SCUBA-2), which show the increase in number of bolometers, sensitivity and faster response from SCUBA to SCUBA-2. The Noise Equivalent Power (NEP) and time constant are from (Rogalski, 2010) 10
1.2 The interferogram orientations in output ports for the 850 μm, which depend on the input ports 19

2.1 Properties of the non-physical spectral features 24
2.2 A comparison of the first and second degree fits of the calibration ramps, observation (s8c20130907_002) bolometer (10, 27). The low values of reduced Chi-squared show that they were good fits. 28
2.3 A summary of the procedures, which were made to invistigate the relation between the input signal and the detectors readout, and for flux jumps and cosmic rays corrections, showing the purposes and the challenges of each procedure. 45

3.1 Specifications of the SCUBA-2 filters (from the Joint Astronomy Centre JAC). 49
3.2 Specification of the SCUBA-2 diachronic filter (from the Joint Astronomy Centre JAC). 49
3.3 Observing parameters for the first set of observations, where the black body in port s8d was held at constant temperature, while the second in port s8c was operated at different temperatures with an uncertainty of $\pm0.5\,^{\circ}$C. . . . 51
3.4 Observing parameters for the second set of observations, where the black body in port s8d was held at constant temperature, while the second in port s8c was operated at three temperatures with an uncertainty of $\pm0.5\,^{\circ}$C . . . 54
3.5 A statistical comparison between the first and second sets, where scans with no data are those filled with (NaN; not a number), the bad scans are those with signal-to-noise ratio less than the threshold (30). 54
3.6 A statistical comparison between the first and second sets, where scans with no data are those filled with (NaN; not a number), the bad scans are those with signal-to-noise ratio less than the threshold (30). 64

4.1 The geocentric positions of the Sun and Venus at 2013/08/14, (Ephemeris). 73
4.2 The m values for some molecular species (Chapman, 2003) 89

4.3 The values of the properties of the ozone lines, where the spectral line strength, energy of the lower level of transition and HWHM obtained from High-resolution Transmission molecular absorption database (HITRAN), the equivalent width is calculated using FTfitter, and the spectral line strength corrected for the temperature and pressure of ozone using Equation 4.6 (Rothman et al., 2013). 90
4.4 The values of the properties of CO line at 11.53 cm^{-1} at T_0 and P_0 101

List of Figures

1.1 The properties of the electromagnetic spectrum (MicroWorlds). 2
1.2 The atmosphere transmission versus the wavelength of the electromagnetic radiation, and the locations generally used to observe in different wavelengths (Wikimedia). 3
1.3 Models of the transmission of the atmosphere of Earth under three different conditions as computed using the Blue Sky Spectroscopy Transmission and Radiance Atmospheric Model (BTRAM) (Chapman, Naylor, Gom, Querel & Davis-Imhof, Chapman et al.). The two bands of SCUBA-2 the 450 µm and 850 µm are shown in blue and red, respectively. (A): excellent observing condition (Precipitable Water Vapour (PWV) = 0.5 mm), (B): average observing condition (PWV = 1 mm), (C): poor observing conditions (PWV is 1.82 mm). 4
1.4 The ground and near space places, which are suitable to perform observations in the sub-millimetre bands (Tremblin et al., 2012). 5
1.5 The PWV of the different places, that are suitable for performing observations in the sub-millimetre band (Tremblin et al., 2012). 6
1.6 A picture of the James Clerk Maxwell Telescope (JCMT) in Mauna Kea, Hawaii (from the the Joint Astronomy Centre JAC). 8
1.7 A diagram showing the basic components of a bolometer (the absorptive element, the thermal link and the thermal reservoir) the light is absorbed in the absorptive element, which can be measured by a thermometer attached to the absorptive element. 12
1.8 The relation between the temperature and the resistance for superconductors (Abazajian et al., 2013). 13
1.9 A Transition Edge Sensor (TES) schematic showing the pairing between TES as a bolometer coupled with a Superconducting Quantum Interface Device (SQUID) used to read out the TES signal indirectly through the change in the magnetic field caused by the change in the current (Wikipedia). 14
1.10 In the presence of an increasing external flux Φ, as shown (a), the current induced in the loop and it increases with the external magnetic field till it flips and start again (b), the induced flux inside the loop (c) that serves to digitize the total flux to the nearest quanta (d) (Clarke, 1993). 16
1.11 The sinusoidal relation between the flux and the output voltage (Wikimedia), which takes such a relation because of the modulations of the absolute values of the current as shown in Figure 1.10 (B). 16

1.12 A diagram showing the Mach-Zehnder configuration (Naylor et al., 2013). The beams are split by the input beam-splitter, then directed to the moving mirror, where a difference in the optical path length is shown in the two beams by a translation of the moving mirror. Finally the beams are recombined by the output beam-splitter. 18
1.13 image of the SCUBA-2 footprint with the four sub-arrays of the 450 µm band labelled, where the dead bolometers are shown in white. Fourier transform spectrometer-2 (FTS-2) only uses the two sub-arrays s4a and s4b (from the Joint Astronomy Centre JAC). 19
1.14 image of the SCUBA-2 footprint with the four sub-arrays of the 850 µm band labelled, where the dead bolometers are shown in white. FTS-2 only uses the two sub-arrays s8c and s8d (from the Joint Astronomy Centre JAC). 20
1.15 A diagram showing the relations between the output ports of FTS-2, where ports A and B share the 450 µm band, ports C and D share the 850 µm band. 20

2.1 The locations of the coefficients of the non-linear response described in Equation 2.2 (Jones, 2010). 24
2.2 A spectrum obtained with FTS-2 showing non linearity features, observation s8c20130813_00080 bolometer (25,29). 25
2.3 The calibration ramps of observation 20130907_007 bolomter (20, 20), superimposed with an interferogram. 25
2.4 Shows the first and second degree polynomial fit to the first calibration ramp of observation (s8c20130907_0007) bolometer (20, 20); the insert shows a magnified region. It is clear that there is no significant difference and the bolometer exhibited a linear response 26
2.5 The calibration ramps of observation (s8c20130907_0007) bolometer (18, 23), where each ramp is identified from one another, taking a different colour, so a polynomial can be fitted to each one later on. The interferogram of the same bolometer is superimposed, with two horizontal dotted lines specifying the power range of analysis. 27
2.6 A raw interferogram with a flux jump in the zero path difference (ZPD) region exhibiting as non-linearity, Observation (s8c20130813_00080) bolomter (25, 29). 29
2.7 The calibration ramps with a flux jump outside the range of interferogram signal, where the analysis is limited to the interferogram range. Observation s8c20130907_0007 bolometer (26, 22). 30
2.8 The calibration ramps with a flux jump inside the range of the interferogram signal precluding further analysis. Observation s8c20130907_0007 bolometer (20, 27). 30
2.9 The relation between the counting rate of cosmic rays and the altitude (Nave, 2012). 31
2.10 An interferogram with a cosmic ray at about 26.2 cm, observation (s8c20131119_00081) bolometer (10, 27). 32

2.11 The derivative of the cosmic ray region in the interferogram. The sudden change in the interferogram caused by a cosmic ray is clearly shown at about 26 cm. 33
2.12 The figure in the top shows the interferogram before (black) and after cosmic rays correction (blue), where at about -35 cm there is an instability region in a flux jump, and at about 26 cm there is a cosmic ray. The figure in the bottom left is a zoom in on the flux jump instability region, and the figure in the bottom right is a magnified region showing the instability in the neighbourhood of a flux jump, while the figure at bottom right is a magnification of the cosmic ray region. Observation (s8c20131119_00081) bolometer (10, 27) 35
2.13 The interferogram with flux jumps at about -35 cm and 30 cm on the left. The obtained spectrum before correcting the flux jumps in the interferogram on the right. Observation (s8c20131119_00081) bolometer (10,27). 36
2.14 The derivative of the interferogram obtained from the first step, where the flux jumps appear as spikes. 37
2.15 The different identified regions (before flux jump, the non-linearity, and after the non-linearity region) of the interferogram, observation (s8c20131119_00081) bolometer (10, 27). The regions that need to be corrected are the non-linearity region in blue, and the flux jump in black. 38
2.16 The different identified regions of the interferogram and the fits to each region, observation (s8c20131119_00081) bolometer (10, 27). The legend shows the region of the raw interferogram (*nonlinear* in blue) and the fitted polynomials (b, a and nf in magenta, cyan and orange, respectively), which will be used in Equation 2.4. 39
2.17 The different identified regions of the interferogram and the fits to each region around the second flux jump, observation (s8c20131119_00081) bolometer (10, 27). The legend shows the region of the raw interferogram (*nonlinear* in blue) and the fitted polynomials (b, a and nf in magenta, cyan and orange, respectively), which will be used in Equation 2.4. 40
2.18 The raw interferogram in blue and the corrected one superimposed in green, and it is obvious that the correction procedure succeeded in retrieving the interferogram. 41
2.19 The spectrum after correcting the flux jumps in the interferogram (red), superimposed by the spectrum before the correction procedure (black), the atmospheric transmission obtained from BTRAM (blue), and a typical spectrum obtained with FTS-2 (green). The retrieved spectrum resembles the typical spectra obtained using FTS-2, and the presence of the line of molecular oxygen at 12.291 78 cm^{-1} can be seen. 42

2.20 Different types of interferograms from observation (s8c20131119_00081), where (a) in green is a very good interferogram obtained from bolometer (11, 24), (b) is the interferogram from bolometer(24, 26) having flux jumps at about -50 cm and 50 cm that can be corrected. On the other hand (c) in black and (d) in red are examples of those interferograms that cannot be corrected because, in (c) there are more than two flux jumps in the interferogram bolometer (24, 32), while (d) is an interferogram with flux jumps and non-linearity in the ZPD region bolometer (17, 27). 43
2.21 An interferogram with more than flux jump two flux jumps but the interferogram can be trimmed to certain range from -80 cm to 80 cm, then the flux jumps at -50 cm and 50 cm can be corrected, observation (s8c20131119_00081) bolometer (13, 19). 44

3.1 The theoretical atmospheric transmission above Mauna Kea for 0.5 mm PWV produced by BTRAM (Chapman, Naylor, Gom, Querel & Davis-Imhof, Chapman et al.). The blue and red regions represent the 450 µm and 850 µm bands of high atmospheric transmission. 47
3.2 The individual spectral profiles of the optical components within SCUBA-2 (Holland et al., 2013). 47
3.3 Schematic of the filters installed in SCUBA-2 and their operating temperatures; BP, LP and HP represent band-pass, low-pass and high-pass, respectively (Holland et al., 2013). 48
3.4 The raw interferogram of the 850 µm band port (C) bolometer (19, 20) showing the baseline drift/low frequency oscillation, observation s8c20131203 – 00011 – 0301. 52
3.5 The raw interferogram of the 850 µm band port (C) pixel (25, 22) showing the presence of a flux jump. 52
3.6 The interferogram of the 850 µm band port (C) bolometer (20, 20), having a flux jump in the zero path difference region. 53
3.7 The number of bolometers versus the percentage of the integrals of the area of the harmonic to that of the band, for temperature 16.8 °C. 55
3.8 The number of bolometers versus the percentage of the integrals of the area of the harmonic to that of the band, for temperature 25.3 °C. 55
3.9 The number of bolometers versus the percentage of the integrals of the area of the harmonic to that of the band, for temperature 34 °C. 56
3.10 A histogram showing the ratio between the root mean square of the harmonic to that of the noise versus the frequency of bolometers for port (C) in the 850 µm band for temperature 16.8 °C. 57
3.11 A histogram showing the ratio between the root mean square of the harmonic to that of the noise versus the frequency of bolometers for port (C) in the 850 µm band for temperature 25.3 °C. 57
3.12 A histogram showing the ratio between the root mean square of the harmonic to that of the noise versus the frequency of bolometers for port (C) in the 850 µm band for temperature 34 °C. 58

3.13 A histogram showing the frequency of pixels versus the signal-to-noise ratio, for the data with the old settings, port (C) the 850 µm band. 59
3.14 A histogram showing the frequency of pixels versus the signal-to-noise ratio, for the data with the new settings, port (C) the 850 µm band. 59
3.15 A phase corrected interferogram of the 850 µm band port (C) bolometer (19, 17) near the ZPD region. 60
3.16 An example of a bad interferogram that did not pass the signal-to-noise condition, 850 µm band port (C) bolometer (18, 18). 61
3.17 The mean spectrum across different scans for bolometer (19, 22) in the 850 µm band port (C) for temperature 34 °C (red), and the mean spectrum across scans for the same bolometer for temperature 16.8 °C (blue). 62
3.18 The Planck functions for the corresponding temperatures, 34 °C (red) and 16.8 °C (blue). 62
3.19 The spectral response function of bolometer (19, 22) in the 850 µm band port (C). 63
3.20 The normalized average spectral response function across the sub array (C) in the 850 µm band (blue), and the standard deviation (red). 63
3.21 The average spectral response function for the four SCUBA-2 sub-arrays used by FTS-2 (thick blue line). Also shown are the SRF as determined from averages of the sub-regions of each sub-array (thin lines). 65
3.22 Comparison between the predicted (solid red) and the measured (dash-dot green: *s*4*b*, dashed blue: *s*4*a*) 450 µm spectral response functions. 66
3.23 Comparison between the predicted (solid red) and the measured (dash-dot green: *s*8*c*, dashed blue: *s*8*d*) 850 µm spectral response functions. 67
3.24 Comparison between the predicted (solid red) with a shift factor of (1.00147), and the measured (dash-dot green: *s*4*b*, dashed blue: *s*4*a*) 450 µm spectral response functions. 67
3.25 Comparison between the predicted (solid red) with a shift factor of (1.01006), and the measured (dash-dot green: *s*8*c*, dashed blue: *s*8*d*) 850 µm spectral response functions. 68
3.26 Retrieval of the black-body temperature for bolometer (19,22) when using the SRF derived from the same bolometer (lower spectrum), the average of 2×2 neighbouring bolometers (second lowest spectrum), the average of 3×3 neighbouring bolometers (third lowest spectrum) and the average of all the active bolometers (top spectrum). The flat line shows the actual temperature measured on the black-body heater (25.3 °C). Curvature in the retrieved temperature indicates poor characterization of the SRF. It can be clearly seen that the more bolometers included in determining SRF, the increasingly further the retrieved temperature is from the actual one. 70

3.27 A comparison between the application of various spectral response functions on the observations of bolometer (19,22), where the Planck function is shown in blue, and the retrieved is in black, which is the division of the observation spectrum by the SRF. Applying the SRF derived from the same bolometer (top left), the average of 2×2 neighbouring bolometers (top right), the average of 3×3 neighbouring bolometers (bottom left) and the average of all the active bolometers (bottom right). Superimposed is the Planck function of the third temperature (T_{A_3}). It can be clearly seen that, the more bolometers are included in determining SRF, the increasingly poorer the fits are to the Planck function. 71

4.1 A portion of the sub-array of port C in the 850 µm band in observation 20130814 scan 001, in which Venus is illuminating four bolometers. The insert shows a zoom of the four bolometers on Venus, and bolometer (14,26) was chosen because it has high signal. 74
4.2 A diagram of the positions of the inner planets at the day of observation 2013-08-14, with the sun at the centre (Wolfram—Alpha, 2014). 75
4.3 A diagram of the phases of Venus in the heliocentric system (Mcclung, 2003). 75
4.4 The distances and angles between the Sun, Venus and Earth at the time of observation. 76
4.5 The atmospheric transmission at the observation date obtained by BTRAM using the PWV given by the Water Vapour Monitor (WVM), where the PWV was 1.82 mm. The 850 µm band in blue and the 450 µm band in red . 77
4.6 The change in temperature and pressure at different altitudes in the atmosphere of Venus (Noel, 2012) 78
4.7 The normalized spectral response function of bolometer (14, 26) port C in the 850 µm band. 80
4.8 The spectrum of Venus obtained from bolometer (14, 26) port C in the 850 µm band, where the slight imbalance between the ports is the reason that the molecular oxygen absorption line (at 12.29 cm^{-1}), which is known to be a saturated line, does not reach zero. 80
4.9 Retrieval of Venus temperature for bolometer (14, 26), when using atmospheric transmission and the SRF derived from the same bolometer, as showed in Equations 4.1 and 4.2 yielding a value of mean temperature (blue) 275.26 K with an uncertainty of ±0.5K, which by looking at Figure 4.6 this indicates that FTS-2 probes a height in the Venusian atmosphere of about 65 km. Since the layers above this height are colder, so the species in higher altitudes will be seen through their absorption lines. 81
4.10 An illustration of the process leading to the presence of absorption lines . . 83
4.11 A diagram of a photon absorbed by a molecule, the molecule gets excited from energy level E_1 to E_2. 84

4.12 A diagram of the absorption of light, when passing through an absorbing material, where, n, is the number density of the absorbing molecule (in molecules cm^{-3}), dz is the thickness of the layer (in cm), both can be related to the column density, u, as $u = ndz$, and k_σ is the absorption coefficient (in cm^2 molecules^{-1}) . . . 84
4.13 A diagram show how the equivalent width is found, where the area of the rectangle is equal to that of the line profile (Rieke, 2002) . . . 86
4.14 The spectrum of Venus obtained from bolometer (14,26) port C in the 850 μm band, the baseline was brought to zero and then the spectrum was normalized. . . . 87
4.15 Using FTfitter gui, an Interactive Data Language (IDL) program written by Brad Gom, to measure the equivalent width of spectral lines, and here we show how it works on the ozone line at 12.157 cm^{-1}, where the blue line denotes the centre of the line, the red line is the continuum, the black is the spectrum, and the green is fitted to the absorption line. . . . 88
4.16 The spectrum of Venus from bolometer (14,26). The vertical lines show absorption lines of ozone included in this analysis . . . 91
4.17 The relation between the equivalent width of each of the absorption lines of ozone as calculated using FTfitter gui and the corrected spectral line strength calculated by Equation 4.2 using HITRAN database and BTRAM. A line is fitted to the data points with a slope of $l = 8.3 \pm 0.5 \times 10^{18}$ cm^{-2} molecules, and intersects the y axis at $-2.2 \pm 0.6 \times 10^{-4}$ cm^{-1}. . . . 92
4.18 The daily ozone column estimate for a 1 x 1 degree area (at Latitude 19.5°, Longitude −155.5°. Taken from the Ozone Mapper and Profiler Suite (OMPS) data set. . . . 93
4.19 The relation between temperature and pressure of the Earth atmosphere in the tropical regions, the data were obtained using BTRAM. . . . 94
4.20 The middle and lower atmospheres of Venus. . . . 96
4.21 The composition of sulfuric species in the atmosphere of Venus (Zhang et al., 2012) . . . 97
4.22 The details of the observed absorption lines and the theoretical absorption lines of five molecules (Rothman et al., 2013). . . . 99
4.23 The retrieved Venus spectrum (red) normalized to the Earth atmospheric transmission profile (black). The vertical lines are the absorption lines of S_2O, ozone, SO_2, SO and CO, which are thought to match what is seen as absorption lines in the retrieved Venus spectrum of bolometer (14, 26). . . . 100
4.24 Using FTfitter gui, an IDL program written by Brad Gom, to measure the equivalent width of spectral lines, and here we show how it is used on the carbon monoxide line, where the blue line denotes the centre of the absorption line, the red line is the continuum, the black is the spectrum, and the green is fitted to the absorption line . . . 102

Acronyms

AIG	Astronomy Instrumentation Group. 11, 17
ALMA	Atacama Large Millimetre Array. 5
APEX	Atacama Pathfinder Experiment. 5
AST/RO	Antarctic Sub-millimetre Telescope and Remote Observatory. 7
BLAST	Balloon-borne Large Aperture Sub-millimetre Telescope. 7
BTRAM	Blue Sky Spectroscopy Transmission and Radiance Atmospheric Model. x, xii, xiii, xv, xvi, 4, 42, 47, 77, 89, 92, 94
CASA	Common Astronomy Software Applications. 82
CSO	California Sub-millimetre Observatory. 7
FLL	Flux-Locked Loop. 17, 34
FTS-2	Fourier transform spectrometer-2. xi, xii, xiv, xv, 11, 17–21, 23, 25, 34, 36, 41, 42, 44, 46, 49, 65, 72, 73, 78, 79, 81, 82, 90, 95, 98, 104, 105

GEISA Gestion et Etude des Informations Spectroscopiques Atmosphriques. 85

HARP Heterodyne Array Receiver Programme. 9, 17

HITRAN High-resolution Transmission molecular absorption database. ix, xvi, 85, 89, 90, 92, 93, 101

IDL Interactive Data Language. xvi, 32, 36, 86, 88, 102

JAC Joint Astronomy Centre. 53

JCMT James Clerk Maxwell Telescope. x, 7–10, 19, 73, 79

JPL Jet Propulsion Laboratory. 85

NEP Noise Equivalent Power. viii, 10

OMPS Ozone Mapper and Profiler Suite. xvi, 90, 93

OPD optical path difference. 23, 38

PWV Precipitable Water Vapour. x, xiii, xv, 4–6, 47, 76, 77

SCUBA Submillimetre Common-User Bolometer Array. viii, 9, 10

SCUBA-2	Submillimetre Common-User Bolometer Array-2. viii, x, xi, xiii, xiv, 4, 9–12, 17–20, 23, 24, 46–51, 64–66, 72, 73, 93, 104, 105
SOFIA	Stratospheric Observatory for Infra-red Astronomy. 7
SQUID	Superconducting Quantum Interface Device. x, 14, 15, 17
SRF	Spectral Response Function. vii, xiv, xv, 65, 66, 69–71, 81
SWAS	Sub-millimetre Wave Astronomy Satellite. 8
TES	Transition Edge Sensor. x, 10, 13–15, 17, 19, 23, 34, 53, 104
WVM	Water Vapour Monitor. xv, 76, 77, 79
ZPD	zero path difference. xi, xiii, xiv, 28, 29, 34, 36, 37, 41, 43, 53, 58, 60

Chapter 1

Introduction

1.1 Sub-millimetre astronomy

Light is radiant energy with measurable properties composed of photons, whose energy is quantized. It has brightness and colour (as seen by human eyes), where the brightness is an indicator of the number of photons, and the colour is a measure of the energy of the photon. The energy of a photon is inversely proportional to its wavelength, as they are related by the Planck-Einstein relation which is represented by (French & Taylor, 1979)

$$E = \frac{hc}{\lambda}, \quad \text{(J)} \tag{1.1}$$

where E denotes the energy, h denotes Planck's constant, c the speed of light and λ denotes wavelength. The values for all physical constants used in this thesis are given in Appendix A. Human eyes are able to detect photons with wavelengths from about 390 nm to 700 nm (Starr et al., 2010), a range that is called the visible spectrum. In this region, red photons have the lowest energy and violet photons have the highest. Outside of the visible range, the electromagnetic spectrum extends from very low energy photons in the radio range to the high energy gamma rays, Figure 1.1 shows a schematic diagram of the electromagnetic spectrum.

When we use instruments to look outside the visible range, we explore different physical conditions of the astronomical sources under investigation. For example when we view the universe in the X-ray range we see emission from such things as active galactic nuclei,

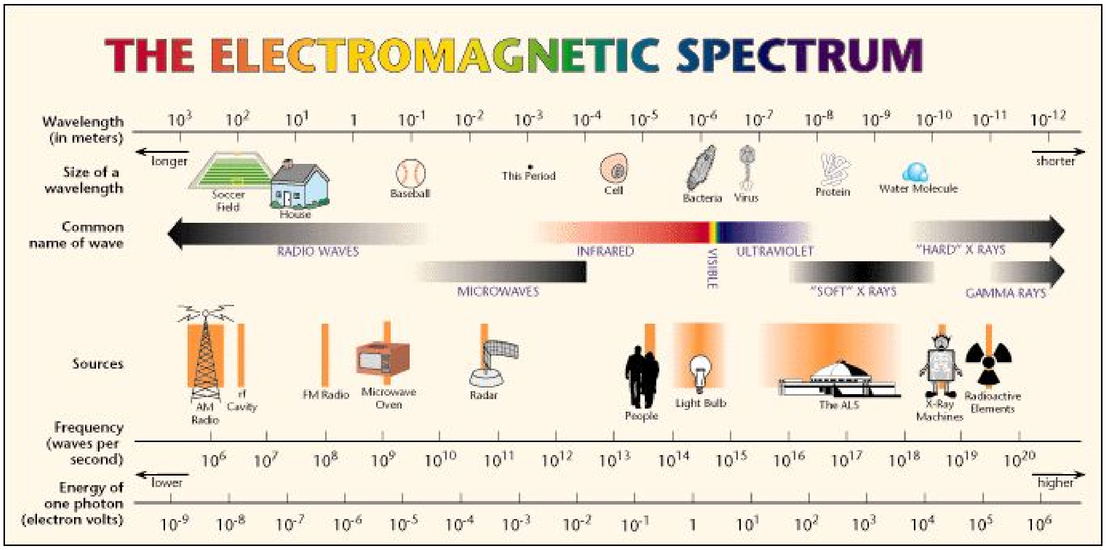

Figure 1.1: The properties of the electromagnetic spectrum (MicroWorlds).

accretion discs around black holes and other high energetic sources. On the other hand, long wavelength observations probe obscured structures in the universe, such as cold dark molecular clouds, from which short wavelength cannot emerge due to Rayleigh scattering.

Sub-millimetre observations contain a wealth of information, which can be used to study low temperature regions in the universe, where stars are typically formed. By analysing sub-millimetre observations of molecular clouds and dark cloud cores, one can determine their atomic and chemical abundances and also study cooling mechanisms in these regions. Sub-millimetre observations can also be used to study high red shift objects, due to the fact that the expansion of the universe results in light emitted at shorter wavelength in the rest frame appearing as longer wavelength in the observation frame.

Sub-millimetre astronomy is one of the last frontiers in astronomy. This is due to the fact that observing in the sub-millimetre wavelengths range (from 200 µm to 1000 µm) is challenging, not only because the transmission of the earth atmosphere is generally low, as shown in Figure 1.2, but also the low energies of the photons in this spectral range. This leads to the necessity of cooling the detectors to cryogenic temperatures, which introduces additional complexities. Figure 1.3 shows the transmission of the atmosphere of Earth under three different conditions.

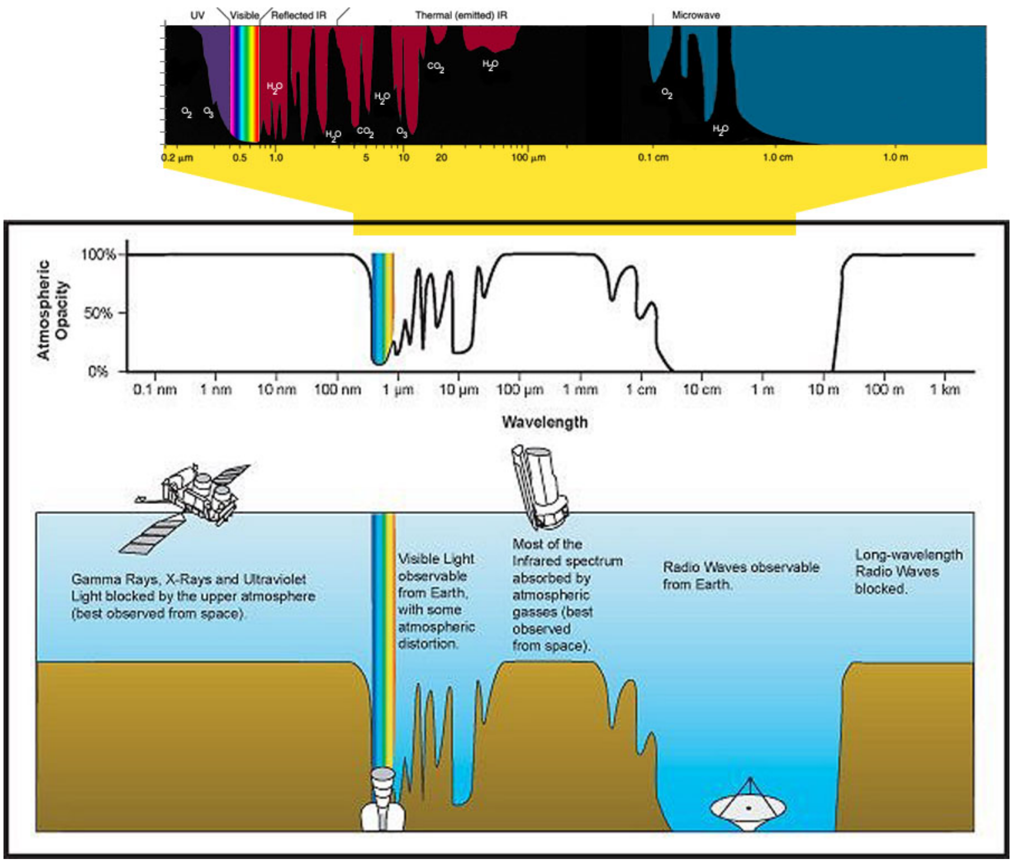

Figure 1.2: The atmosphere transmission versus the wavelength of the electromagnetic radiation, and the locations generally used to observe in different wavelengths (Wikimedia).

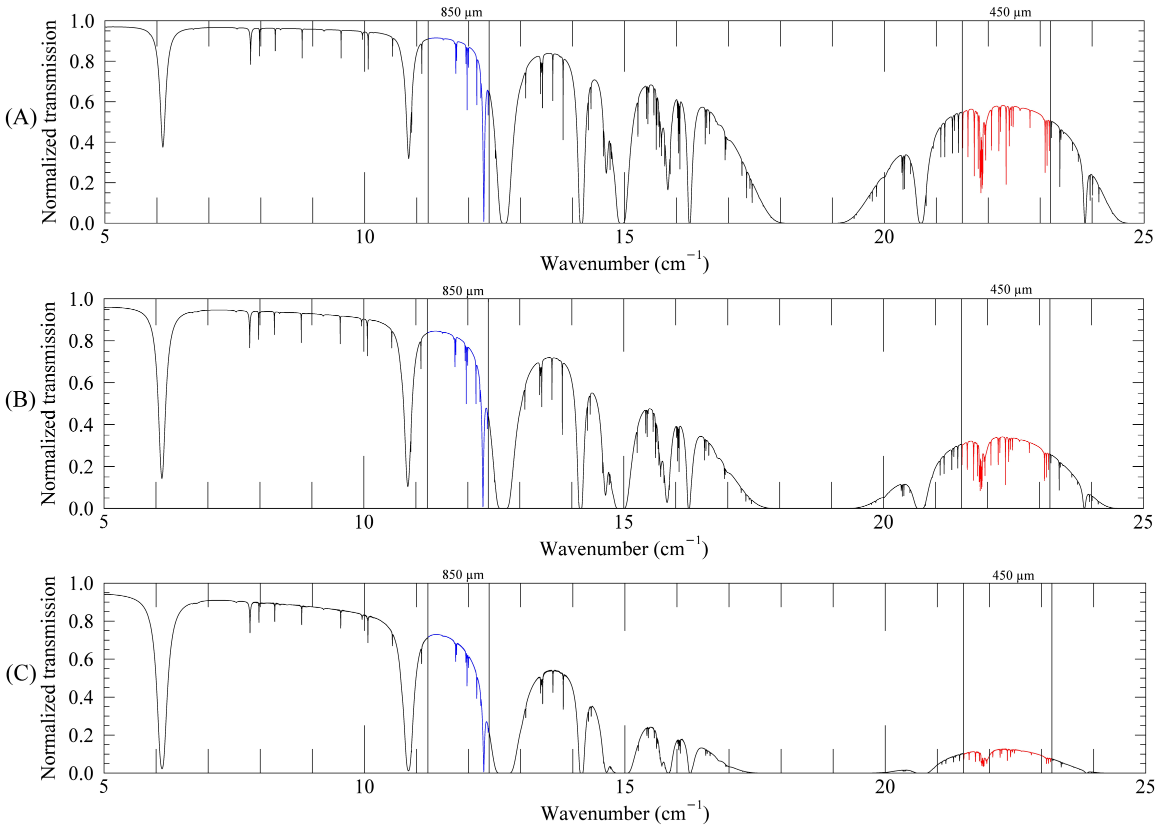

Figure 1.3: Models of the transmission of the atmosphere of Earth under three different conditions as computed using the BTRAM (Chapman, Naylor, Gom, Querel & Davis-Imhof, Chapman et al.). The two bands of SCUBA-2 the 450 µm and 850 µm are shown in blue and red, respectively. (A): excellent observing condition (PWV = 0.5 mm), (B): average observing condition (PWV = 1 mm), (C): poor observing conditions (PWV is 1.82 mm).

The low atmospheric transmission at sub-millimetre wavelengths is primarily due to absorption by atmospheric water vapour. Observations in this region are therefore carried out from high altitude mountains or from space where PWV is as low as possible. Sub-millimetre astronomy can be categorized into three categories, according to the location from which the observations are performed;

1. Ground-based observations

   Observing in the sub-millimetre range from the ground is performed from a small number of places, which are dry and have high altitudes, in order to overcome the limited transmission of the atmosphere. Such places are shown in Figure 1.4, and their cumulated PWV from 2008 to 2010 is shown in Figure 1.5. They include:

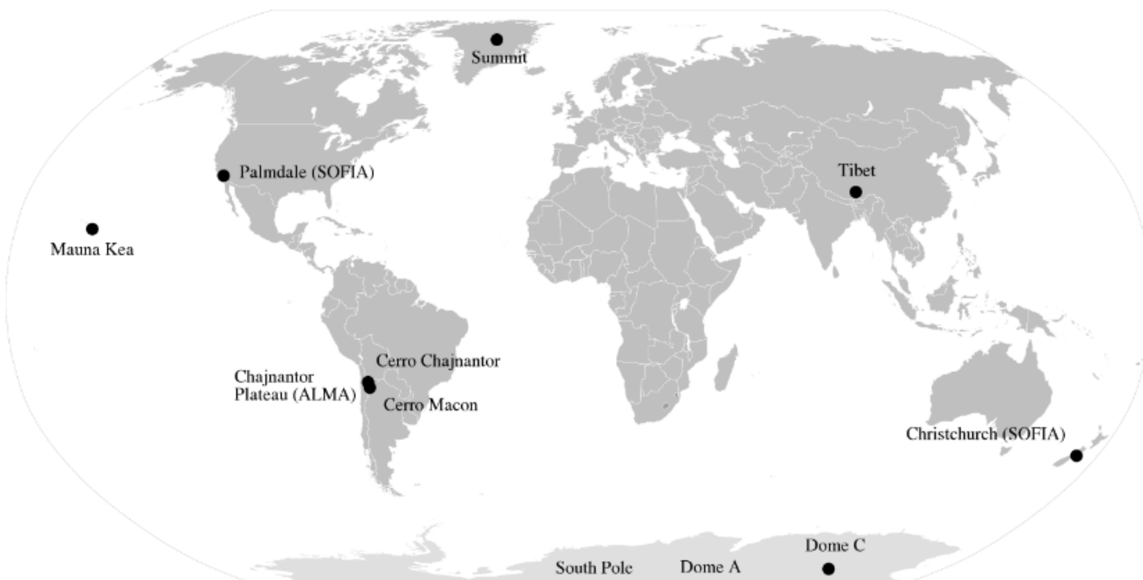

Figure 1.4: The ground and near space places, which are suitable to perform observations in the sub-millimetre bands (Tremblin et al., 2012).

- The Llano de Chajnantor Observatory on the Atacama Plateau (Chile) hosts the Atacama Pathfinder Experiment (APEX), which is the largest sub-millimetre telescope in the southern hemisphere with a primary reflector of 12 m (Güsten et al., 2006), and the Atacama Large Millimetre Array (ALMA), which consists of 50, 12 m antennas (Turner, 2006).

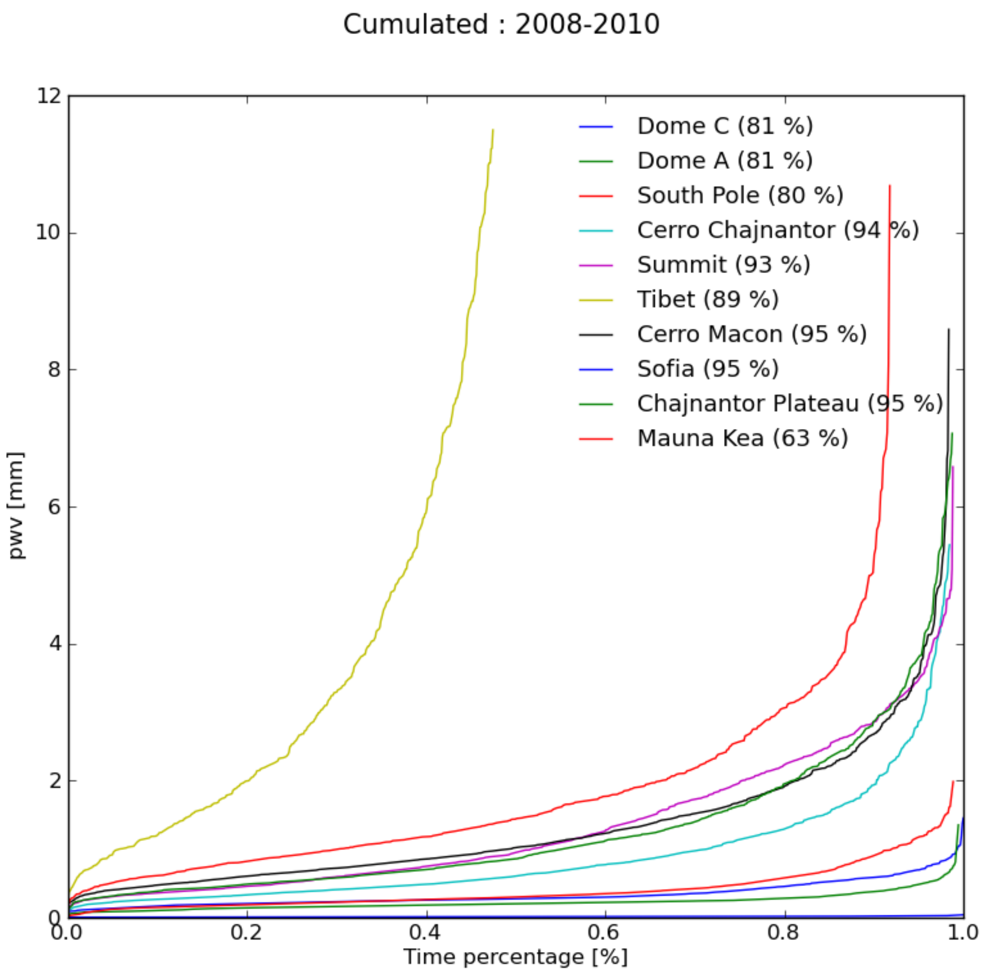

Figure 1.5: The PWV of the different places, that are suitable for performing observations in the sub-millimetre band (Tremblin et al., 2012).

- Mauna Kea (Hawaii) hosts the JCMT which is the largest sub-millimetre telescope with a 15 m primary mirror (Economou et al., 2006). The JCMT will be discussed in more detail in the next section.
- Mauna Kea also hosts the California Sub-millimetre Observatory (CSO) which is a 10.4 m diameter telescope (Murdin, 2000).
- The South Pole hosts the Antarctic Sub-millimetre Telescope and Remote Observatory (AST/RO), a 1.7 m diameter telescope that operates at wavelengths between 200 µm and 2000 µm (Stark et al., 2001).

2. Near space observations

   In this case, the telescope is deployed at a high altitude from 18 km to 37 km using aircraft and balloons, respectively. Unlike ground based telescopes, which can be made very large, near space telescopes are relatively small. Examples of telescopes that perform sub-millimetre observations from near space are;

   - The Balloon-borne Large Aperture Sub-millimetre Telescope (BLAST). It has a 2 m primary mirror and operates at 250 µm, 350 µm and 500 µm (Pascale et al., 2008).
   - The Stratospheric Observatory for Infra-red Astronomy (SOFIA) is a 2.7 m diameter reflecting telescope on an aircraft, and operates at wavelengths from 0.3 µm to 1.6 mm (Young et al., 2012).

3. Space observations

   In this case, the telescope is launched into space to completely escape the opaqueness of the atmosphere of Earth. for practical reasons the size of primary mirrors for space telescopes are generally much smaller, being similar to the near space and airborne counterparts. Examples for the sub-millimetre space telescopes in space are:

- The Sub-millimetre Wave Astronomy Satellite (SWAS), which is in a low Earth orbit and was launched in 1998. The size of its primary mirror is 54×68 cm, with two heterodyne receivers operating at frequencies of 487 GHz, 492 GHz, 557 GHz, 551 GHz and 548 GHz (Melnick et al., 2000).

- The Herschel space observatory occupied with the largest primary mirror launched into space to date. It has a 3.5 m primary mirror, and operates in a spectral range from 55 µm to 671 µm. The Herschel Space Observatory is in a Lissajous orbit around the second Lagrangian point of the Earth-Sun system (Pilbratt et al., 2010).

1.2 The James Clerk Maxwell Telescope

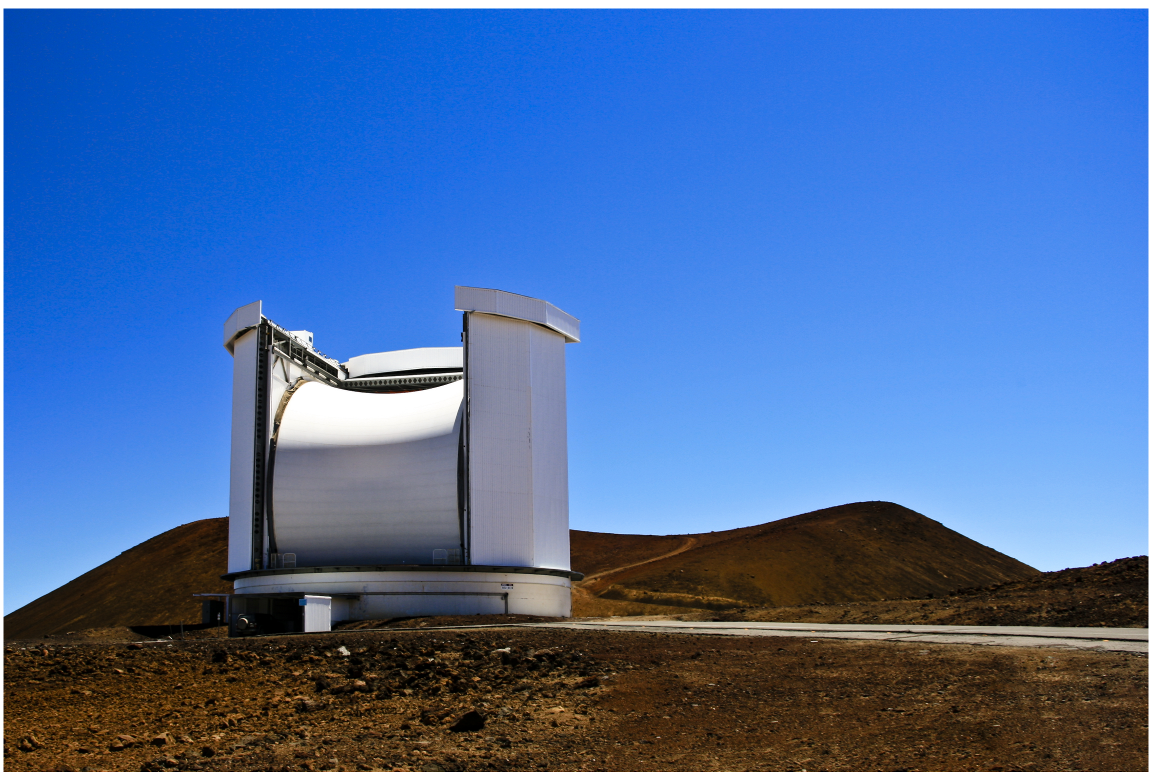

Figure 1.6: A picture of the JCMT in Mauna Kea, Hawaii (from the the Joint Astronomy Centre JAC).

The James Clerk Maxwell Telescope named in honour of mathematical physicist James

Clerk Maxwell (1831 1879), who gave us a fundamental understanding of electricity and magnetism. The JCMT is located atop Mauna Kea, Hawaii at an altitude of 4092 m; its 15 m primary mirror provides a spatial resolution of 7.5″ for the 450 µm band, and 14″ for the 850 µm band (Johnstone & Bally, 1999). The JCMT was initially funded by a several countries, the United Kingdom, Canada and the Netherlands. The JCMT is operated by the Joint Astronomy Centre (JAC). Two kinds of observations are conducted by the JCMT:

- Heterodyne spectral line detection is made possible by the Heterodyne Array Receiver Programme (HARP). It has 16 pixels, and operates at frequency range from 325 GHz to 375 GHz. It performs narrow-band high spectral resolution observations (up to 1.9 GHz of bandwidth with a resolution of 0.977 MHz) (Smith et al., 2008). Its primary objective is searching for emission lines from molecular and atomic species. The spectral line observations can be used to identify the atomic and molecular abundances, identifying particular elements in molecular clouds, and studying the velocities gradient across astronomical objects using Doppler effect.

- Broad band continuum observations made by the SCUBA-2, whose primary objective is to probe continuum emission. The continuum observations are used in the study of star formation, the evolution of galaxies and dust emission associated with planet forming solar systems, which will be discussed in more detail in the next section.

1.3 Sub-millimetre Common-User Bolometer Array-2

SCUBA-2 is an innovative camera designed to work on the JCMT and replace its predecessor, the highly successful sub-millimetre camera, SCUBA, which was operational from 1996 to 2005 (Holland et al., 1998). The main scientific goals behind designing SCUBA and SCUBA-2 are to carry out large-scale surveys of the sub-millimeter sky, and high resolution imaging of selected regions observable from location of the JCMT (Holland et al., 2003).

SCUBA had 128 detectors, individually constructed semi-conductor bolometers, divided into two wavelength arrays (bolometers will be discussed in more details in Section 1.4) with 91 bolometers in the short-wavelength array (SW), and 37 bolometers in the long-wavelength array (LW). The SW array was optimized for the 450 µm band, and the LW array was optimized for the 450 µm band (Holland et al., 1999). SCUBA bolometers were cooled to a temperature of 100 mK, and employed semi-conductor thermometers to measure small temperature changes (Holland et al., 1996).

SCUBA-2 consists of super conducting transition edge sensors operating at 450 µm and 850 µm, which can be fabricated in large format, such that SCUBA-2 has large arrays (10 240 bolometers covering both bands 450 µm and 850 µm, which enables it to perform wide field observations). Table 1.1 compares the NEP, time constants and number of bolometers for SCUBA and SCUBA-2.

Table 1.1: The properties of SCUBA and SCUBA-2, which show the increase in number of bolometers, sensitivity and faster response from SCUBA to SCUBA-2. The NEP and time constant are from (Rogalski, 2010)

Instrument	**The Noise Equivalent Power NEP (W Hz$^{-1/2}$)**	**Time constant (ms)**	**Number of Bolometers**	**Comments**
SCUBA	1.5×10^{-16}	6	128	Semiconductor bolometers
SCUBA-2	7×10^{-17}	$1-2$	10240	Superconducting bolometers

SCUBA-2 was designed to exploit the large field of view provided by the JCMT ($43' \times 43'$) (Dempsey et al., 2012). The larger sub-arrays of the new TES bolometers, their lower operating temperature and the requirement to cool the final imaging mirror of 1.2 m diameter to 4 K, resulted in a significantly larger cryostat, 2.3 m high, 1.7 m wide and 2.1 m long (Holland et al., 2013).

The cryostat is made of a series of sub-systems, which consists of (from the outside to the inside of the cryostat) vacuum vessel, insulating blanket, radiation shield operating at 60 K, and a main optics box, which houses the cold re-imaging mirrors (three cold mirrors are operating at 4 K) and the 1 K box. coated with a high magnetic permeability material to eliminate magnetic fields. The cryostat also houses the two focal plane units that contain the cold electronics and the arrays of the superconducting transition edge sensors, which are cooled to less than 100 mK. The optics box and the radiation shield are cooled by a pair of pulse tube coolers (Holland et al., 2006).

While SCUBA-2 produces photometric images at two wavelength bands, two additional instruments were proposed to extend the capabilities of SCUBA-2, so that it can perform polarimetric imaging and spectroscopic imaging. The polarimetric imaging is performed using POL-2, manufactured at the University of Montreal (Bastien et al., 2011), and the spectroscopic imaging is performed using FTS-2, manufactured by the Astronomy Instrumentation Group (AIG) at the University of Lethbridge. This thesis presents results from the early phase commissioning of FTS-2.

1.4 Bolometer

A bolometer is a device that measures the power of incident electromagnetic radiation. The word 'bolometer' comes from the Greek word (bolē) which means ray of light, and the English word (meter). A bolometer measures the power of the incident light by first absorbing the incident light, which raises the temperature of the bolometer. A schematic of the bolometer is shown in Figure 1.7. It consists of an absorptive element whose temperature changes with the amount of incident light, attached to a thermometer. Once calibrated the absorbed power can be determined from measuring the change in temperature.

The change in temperature of the thermometer can be measured indirectly by measuring the change in resistance, as the resistance of an element is related to its temperature. Historically, semi-conductors have been used as thermometers, where the temperature dependence of semiconductor resistance for cryogenic temperatures is given by

$$R = R_0 \left(\frac{T}{T_0} \right)^{-4}, \qquad (\Omega) \qquad (1.2)$$

where R_0 is the resistance at reference temperature T_0, and R is the resistance at temperature

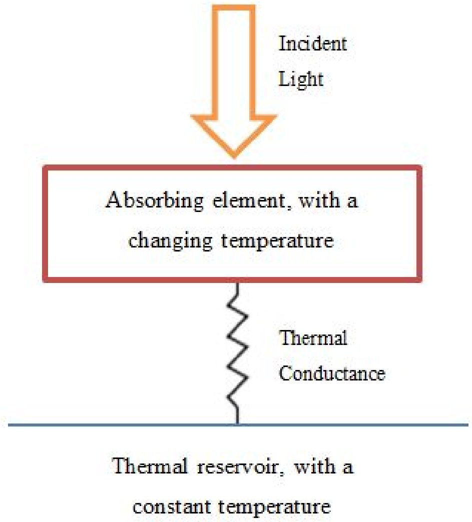

Figure 1.7: A diagram showing the basic components of a bolometer (the absorptive element, the thermal link and the thermal reservoir) the light is absorbed in the absorptive element, which can be measured by a thermometer attached to the absorptive element.

T (Rogalski, 2010).

Nowadays many bolometers use superconductors as absorptive elements providing greater sensitivity. This is made possible because the change in temperature has a greater effect on the resistance of superconductors than semiconductors, enabling the detection of small changes in temperature. Furthermore, unlike semiconductors, superconductor bolometers can be mass-produced, and be used in the manufacturing of large bolometers arrays.

Since the Johnson noise, which is the electronic noise generated by thermal agitation, is given by

$$V_n = \sqrt{4k_B TRB}, \qquad (\mathrm{VHz}^{-1/2}) \qquad (1.3)$$

where k_B denotes Boltzmann's constant, T is the temperature, R is the resistance and B is the bandwidth (Engelberg, 2006). Thus in order to achieve the sensitivity required for submillimetre observations, bolometers must be cooled down to a fraction of a degree above absolute zero, typically from 300 mK to 50 mK and having a low impedance is preferred. SCUBA-2 bolometers are cooled down to less than 100 mK. Since SCUBA-2 is the first in the breed of a new type of detector, which exploits large arrays (32×40 bolometers) of superconductor bolometers, which will be discussed in more detail in the next section.

1.5 Transition Edge Sensor (TES)

A superconductor bolometer is a type of bolometer called TES, which exploits the temperature-resistance relation of the superconducting transition, see Figure 1.8.

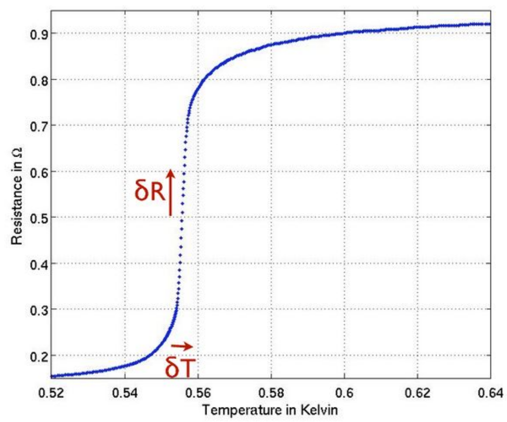

Figure 1.8: The relation between the temperature and the resistance for superconductors (Abazajian et al., 2013).

The sensitivity of TESs can be up to two orders of magnitude better than that for the semiconductor bolometer (Irwin & Hilton, 2005a). The TES sensitivity is due to the narrow width of the transition shown in Figure 1.8, such that a temperature change of about 0.02 mK can give a change in resistance of 20 mΩ (Irwin & Hilton, 2005a). The change in temperature is related to the change in resistance by:

$$\alpha = \frac{1}{R}\frac{dR}{dT}, \qquad (\mathrm{K}^{-1}) \qquad (1.4)$$

where α is the temperature coefficient of resistance, R (Jones, 2010). As seen in Figure 1.8 superconductors exhibit a large positive $\frac{dR}{dT}$ at the superconducting transition. Absorption of light leads to small change in temperature, which leads to an increase in the resistance. Since the TES is voltage biased by driving a current source I_{bias} through a load resistor R_L, the increase in resistance will decrease the Joule power since

$$P = \frac{V^2}{R}. \qquad \text{(W)} \quad (1.5)$$

The decrease in Joule heating will drive the device back to its original temperature. This is known as negative electro-thermal feedback as the change in Joule heating opposes the change in temperature. Also the increase in resistance will decrease the current, which can be measured indirectly through the change in the magnetic field that it produces.

Although the potential of the measurement of superconducting transition was first demonstrated in the 1940s (Andrews et al., 1942), the TESs were seldom used as detectors due to the challenge associated with operating them within the narrow superconductivity transition region. In addition to the difficulty of reading out the change in the resistance or in the current, because the TESs generally have low resistance, a few mΩ, standard operational amplifier based readout electronics cannot be used (Irwin & Hilton, 2005b).

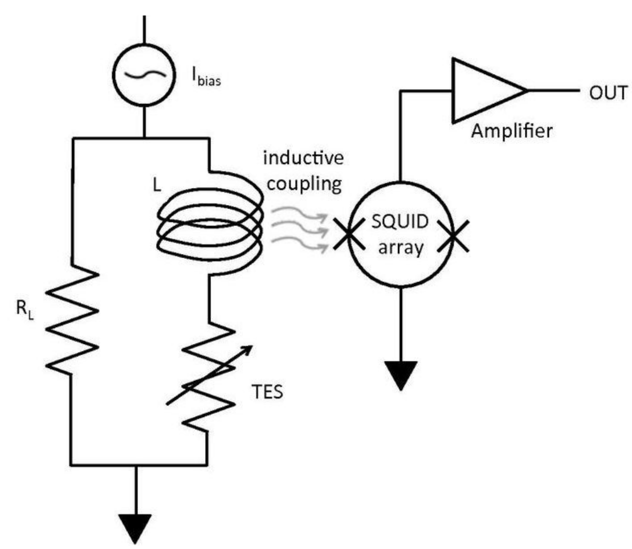

Figure 1.9: A TES schematic showing the pairing between TES as a bolometer coupled with a SQUID used to read out the TES signal indirectly through the change in the magnetic field caused by the change in the current (Wikipedia).

In order to read out the signal from the low impedance detector a SQUID is used to measure the change in magnetic field resulting from the change in the detector current, see

Figure 1.9. The TES is operated in series with the input coil which is inductively coupled to a SQUID, so a change in TES current manifests as a change in the input flux read by the SQUID, which will be discussed in more detail in the next section.

1.6 Superconducting Quantum Interface Device (SQUID)

SQUIDs rely on the quantization of magnetic flux, which is the fact that the flux going through the loop of superconducting material can only take on discrete values, where the fundamental flux quantum is given by:

$$\Phi_0 = \frac{h}{2e} \simeq 2 \times 10^{-15}, \qquad \text{(Wb)} \qquad (1.6)$$

where h is the Planck constant, e is the electron charge and the factor of 2 is accounting for the fact that electrons travel in pairs (Cooper, 1956).

If there is a superconducting loop in the presence of an increasing external flux Φ, a current is induced in the loop (because of superconductivity the current will continue to flow till the flux changes). The current then induces a flux inside the loop, which serves to digitize the total flux to the nearest quanta. In this way the overall flux always jumps in discrete steps of Φ_0 from one flux level to the higher, as shown in Figure 1.10 (d).

Thus by monitoring the number of times it makes discrete jumps one can measure the flux quanta, while the fractions can be measured by monitoring the current (because it is induced by the fraction of flux), this serves to make it possible to measure precisely external magnetic field that is induced in the inductive coil of the TES circuit, leading to the measurement of the incident light on the bolometer.

Since the relation between the applied flux and the output voltage is sinusoidal, see Figure 1.10 (B) and Figure 1.11 (because the current keeps increasing with the increase of the external magnetic field till it reaches a certain value then it flips, making its absolute value decreases with the increasing magnetic field), the output response is not related except

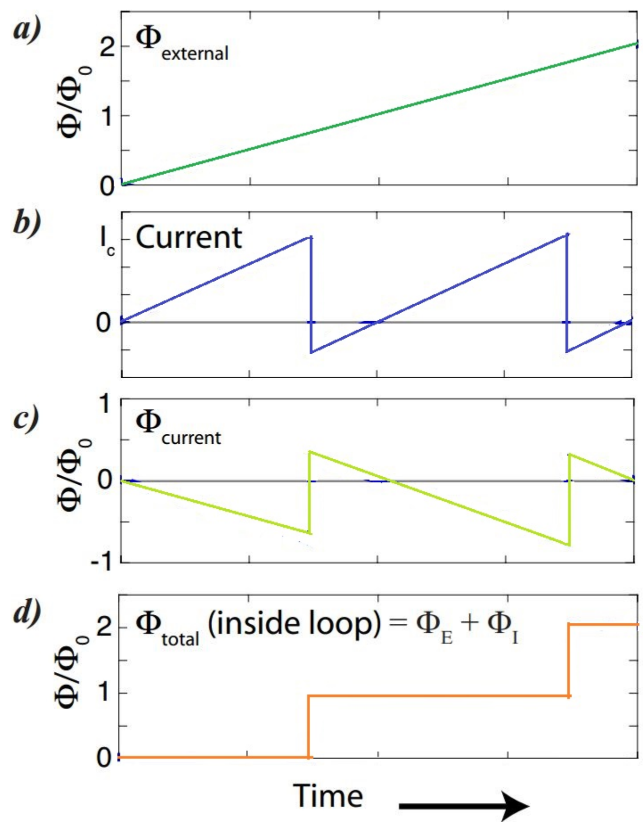

Figure 1.10: In the presence of an increasing external flux Φ, as shown (a), the current induced in the loop and it increases with the external magnetic field till it flips and start again (b), the induced flux inside the loop (c) that serves to digitize the total flux to the nearest quanta (d) (Clarke, 1993).

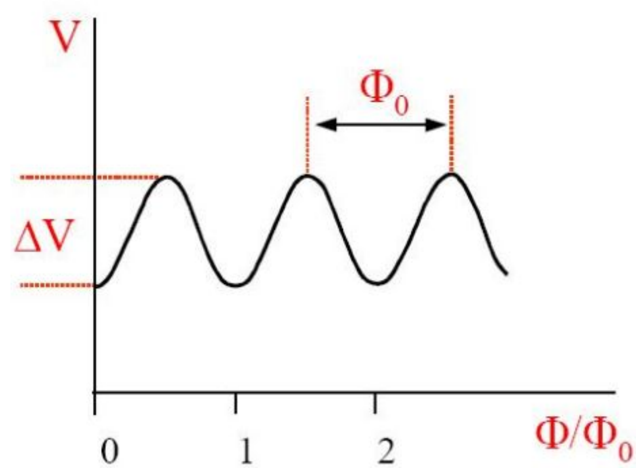

Figure 1.11: The sinusoidal relation between the flux and the output voltage (Wikimedia), which takes such a relation because of the modulations of the absolute values of the current as shown in Figure 1.10 (B).

for the fractions of quanta. To resolve this problem, and to monitor the number of flux quanta, so that it is possible to precisely measure the magnetic flux, the SQUID is usually operated (at constant flux) in a Flux-Locked Loop (FLL), where a feedback loop generates a flux on SQUID that is equal and opposite to the external magnetic flux. Each time the range of SQUID is exceeded, the feedback is reset to zero and a flux quantum are counted together with a fraction of a flux quantum, using a FLL also linearises the output signal.

Flux jumps typically occur when the rate of flux change is too large, where the FLL loses its lock and then recovers at a different quantum level miscounting the number of flux quanta (Foley et al., 2004). Changing (increasing) the voltage bias in the TES decreases the number of flux jumps in the data, because the responsivity of the TES (the rate of flux change in SQUIDs) is simply the inverse of the bias voltage (Lee et al., 1996).

In the context of signal recorded by interferometer, any abrupt changes in the recorded signal, upon Fourier transform lead to spectral artefacts in the reconstructed spectrum as will be discussed in the next chapter. Therefore, flux jumps are of particular concern to a Fourier transform spectrometer. Methods for their identification and mitigation are discussed in Section 2.4.

1.7 Fourier transform spectrometer (FTS-2)

A Fourier transform spectrometer was designed by the AIG at the University of Lethbridge in a Mach-Zehnder configuration, see Figure 1.12. FTS-2 fills a niche between the SCUBA-2 continuum images and the higher spectral resolution with limited size images obtained by HARP. The FTS-2 can gather information about planets in the solar system, and it can operate as a galactic spectrometer, mapping spectral index of molecular clouds in nearby galaxies, and distant galaxies. FTS-2 should provide a spectral resolution of $0.1\,\mathrm{cm}^{-1}$ to $0.006\,\mathrm{cm}^{-1}$, which can be used to gather information about (Gom & Naylor, 2004):

- Interstellar medium, where FTS-2 will provide spectral line mapping.

- Planetary atmospheres, where FTS-2 can provide a continuum from which the temperature can be retrieved, and spectral lines from which the elements abundances can be mapped.

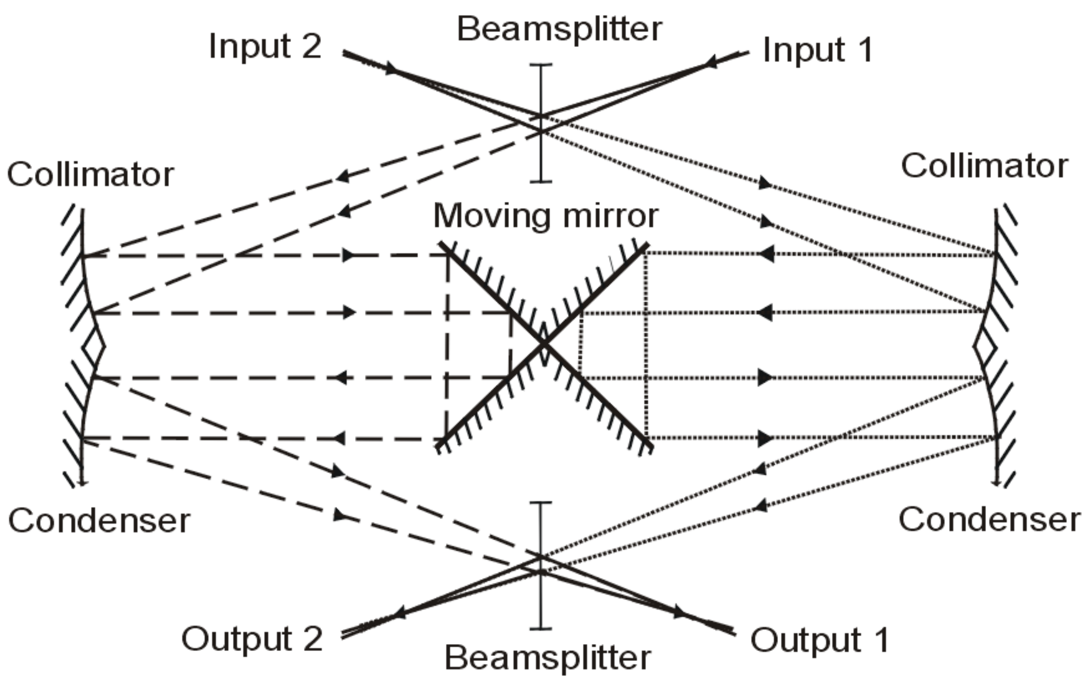

Figure 1.12: A diagram showing the Mach-Zehnder configuration (Naylor et al., 2013). The beams are split by the input beam-splitter, then directed to the moving mirror, where a difference in the optical path length is shown in the two beams by a translation of the moving mirror. Finally the beams are recombined by the output beam-splitter.

Since FTS-2 was designed in a Mach-Zehnder configuration, it provides access to both input ports and both output ports, which in principal enables for atmospheric cancellation. This is because each observation is a differential measurement of the two input ports, where an input port points at the astronomical source and sky, while the other is only observing the sky emission alone. Thus because the background is common in both ports, by taking differential measurement the background is cancelled out in real time.

FTS-2, like SCUBA-2, operates simultaneously at two bands, 450 µm and 850 µm. However, unlike SCUBA-2, limitations in the size of the optics of FTS-2 dictated that FTS-2 is only able to use half of the arrays. Figures 1.13 and 1.14 show the bolometers arrays

Table 1.2: The interferogram orientations in output ports for the 850 μm, which depend on the input ports

	Output port C	**Output port D**
Input port C	Upright	Inverted
Input port D	Inverted	Upright

for the 450 µm and 850 µm bands, respectively. Thus FTS-2 is only using two sub-arrays

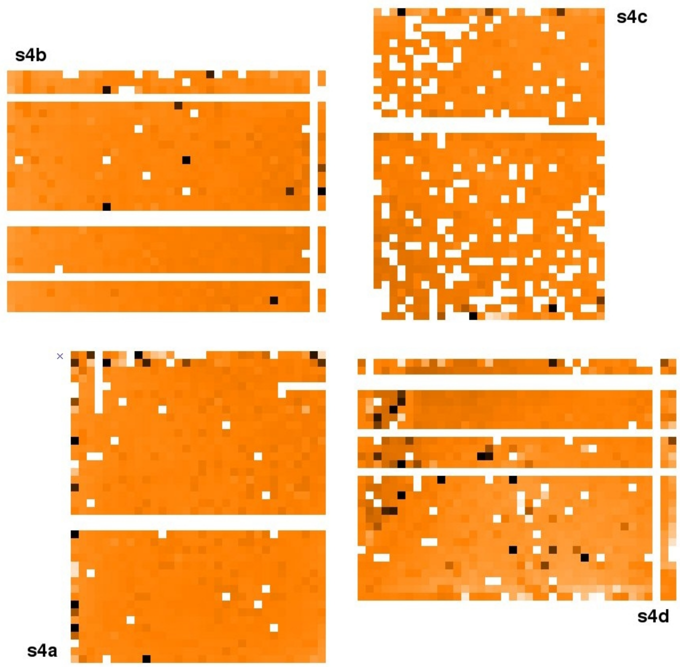

Figure 1.13: image of the SCUBA-2 footprint with the four sub-arrays of the 450 µm band labelled, where the dead bolometers are shown in white. FTS-2 only uses the two sub-arrays s4a and s4b (from the Joint Astronomy Centre JAC).

in each band not all four, a and b for the 450 µm band, and c and d for the 850 µm band, Figure 1.15 shows the relations between the output ports. In the ideal case the interferogram obtained in C will be identical to that in D but inverted, Table 1.2 shows the orientation of the spectrum for the 850 µm band.

Since it was the first time a TES array had been used inconjuction with Fourier transform spectrometer, it did not come as a surprise that several issues emerged during the commissioning of FTS-2. This thesis is concerned with early commissioning results obtained using FTS-2 at the JCMT. Therefore, we had to understand the new issues that have risen from

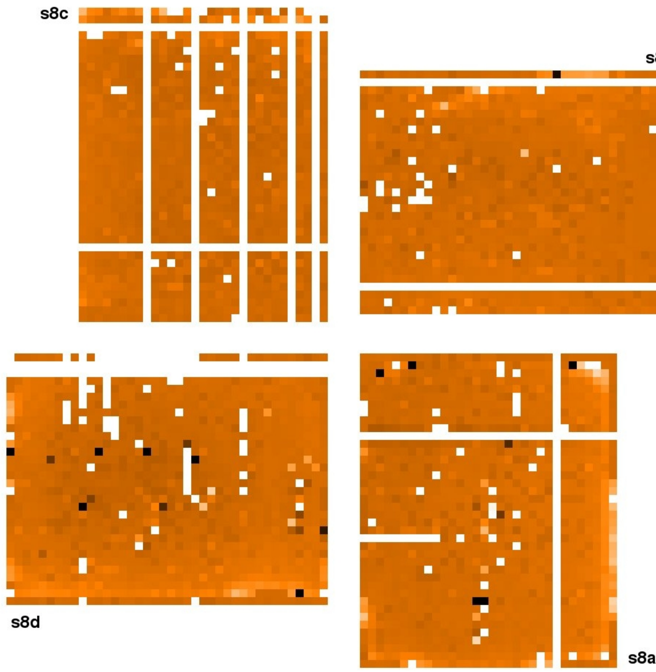

Figure 1.14: image of the SCUBA-2 footprint with the four sub-arrays of the 850 µm band labelled, where the dead bolometers are shown in white. FTS-2 only uses the two sub-arrays s8c and s8d (from the Joint Astronomy Centre JAC).

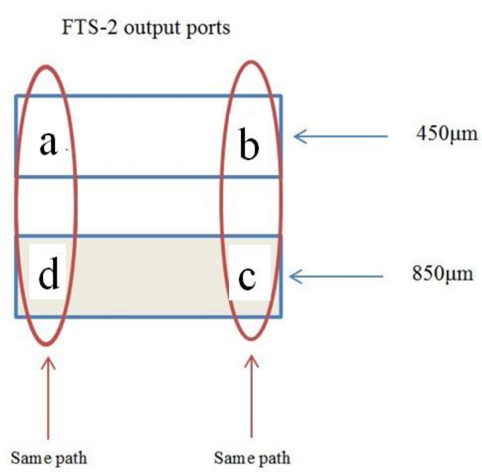

Figure 1.15: A diagram showing the relations between the output ports of FTS-2, where ports A and B share the 450 µm band, ports C and D share the 850 µm band.

using the first superconducting detector array with a Fourier transform spectrometer. Chapter 2 discusses the challenges of the correct interpretation of the data received, Chapter 3 discusses the integrated spectral response function of the whole system, and finally Chapter 4 discusses early astronomical observation using FTS-2, and demonstrated the sensitivity that is achieved by observation of Venus. The Venusian spectra has been used to determine the ozone column abundance in the Earth's atmosphere, and for the first time, determined the CO absorption line in Venus with a Fourier transform spectrometer.

Chapter 2

Data Processing Challenges

2.1 Overview

As noted previously, this was the first time that a superconductor detector array has been used in conjunction with a Fourier transform spectrometer. The preliminary study showed that while some bolometers behave as expected, others had artefacts that were latter shown to be associated with flux jumps and cosmic rays. Finally dead bolometers usually entire rows or columns, due to the multiplex schema for the detector readout were present. The most important of these artefacts identified in the data is the presence of flux jumps.

A triage approach was used to identify three classes: those in which the bolometers were well behaved, those that were beyond repair, and those that exhibited several artefacts, which impacted the scientific use, but ones that could be corrected. The triage was based on, first identifying the bolometers with recoverable artefacts, and second to mitigate them, so that they are adequate for the scientific use.

Since even the signal from individual bolometers vary from one scan to another, algorithms were developed to eliminate certain bolometer scans having peculiar features such as low signal-to-noise ratio, non-linearity and instability from further processing. This chapter discusses how to overcome the most important issues, which are the identification and correction of flux jumps discussed in Section 2.4, and the correction of cosmic rays discussed in Section 2.3. But before discussing the correction algorithms Section 2.2 introduces a test, which has been developed in order to investigate the relation between the input signal and the readout of the detectors, in particular to determine whether the relation is linear, a necessary step in Fourier analysis .

2.2 Data calibration

2.2.1 Non-linearity

A non-linear relation between the input signal and the bolometer readout can significantly impact the retrieval of accurate spectral fluxes, the effect is manifested as a series of non-physical harmonic features in the spectrum. As discussed in the first chapter, SCUBA-2 contains TES bolometers, which are linear devices when operated at the centre of their transition, but become non-linear when driven to the edges of the transition by large modulations in the measured signal, such that the negative electro-thermal feedback can not catch up with the input signal, see Figure 1.8. This is particularly problematic when using FTS-2, where its large modulation can drive the TES to the edges of the transition. Therefore this section investigates whether the bolometers are driven non-linear using FTS-2. The spectrum can be obtained from the interferogram, which is the measured signal produced using FTS-2, as

$$B(\sigma) = \int_{-L_{max}}^{L_{max}} I(x) \mathrm{e}^{-2\pi i \sigma x} \mathrm{d}x, \qquad (\mathrm{W}(\mathrm{cm}^{-1})^{-1}) \quad (2.1)$$

where I is the power on the detector as a function of the optical path difference, x, L_{max} is the maximum of the optical path difference (OPD), and B is the spectral power as a function of wavenumber, σ. Since the Fourier transform is a linear operator, it is essential for the detector readout signal to be linearly related to the input signal. If this is not the case, the effect is manifested as a series of non-physical spectral features that effectively steal power from the fundamental band. Thus when the detector response is non-linear, the spectrum can be expressed as

$$S(\sigma) = \alpha' + \beta' B(\sigma) + \gamma' [B(\sigma) * B(\sigma)] + \delta' [B(\sigma) * B(\sigma) * B(\sigma)] \quad (2.2)$$

The third and fourth terms on the right hand side of Equation (2.2) are responsible for the non-physical spectral features in the harmonic bands, which effectively decreases the intensity in the fundamental band and introduce the harmonic bands, however the energy lost to the harmonics is not conserved. It is important to know that in this transform the energy is not conserved. That is to say the energy in the harmonic bands is much less than would be present in the fundamental, see Figures 2.1 and 2.2.

Table 2.1: Properties of the non-physical spectral features

Coefficient	**Width**	**Location**
β' (fundamental band)	σ_w	σ_o
γ'	$2\sigma_w$	0 and $2\sigma_o$
δ'	$3\sigma_w$	σ_o and $3\sigma_o$

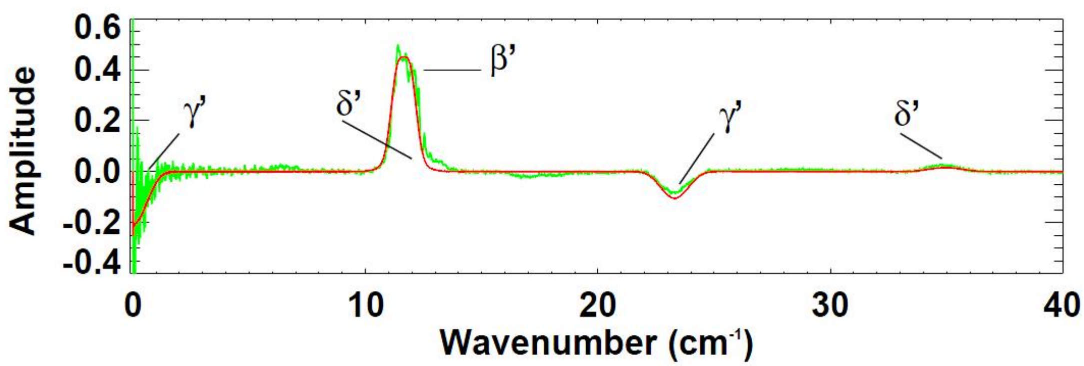

Figure 2.1: The locations of the coefficients of the non-linear response described in Equation 2.2 (Jones, 2010).

In order to calibrate the SCUBA-2 bolometers, the temperature of a heater internal to the SCUBA-2 cryostat is increased and the output signal is recorded to provide a calibration, this allows one to obtain the responsivity Volts per Watt. Thus before every observation a calibration scan is taken, where a known signal from an internal heater is generated, and an output signal is obtained from each detector, such that a relation can be established between the input signal and the readout, see Figure 2.3. The relation between the input power (pW) and the detector signal (V) can be investigated by fitting different degrees of polynomials to

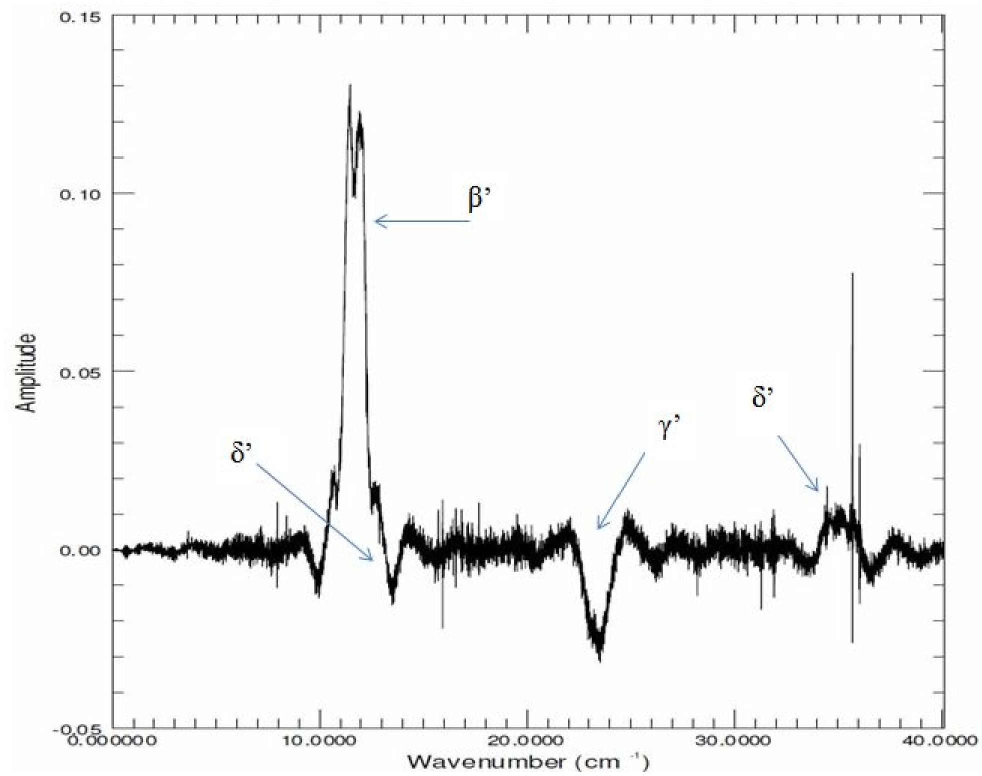

Figure 2.2: A spectrum obtained with FTS-2 showing non linearity features, observation s8c20130813_00080 bolometer (25,29).

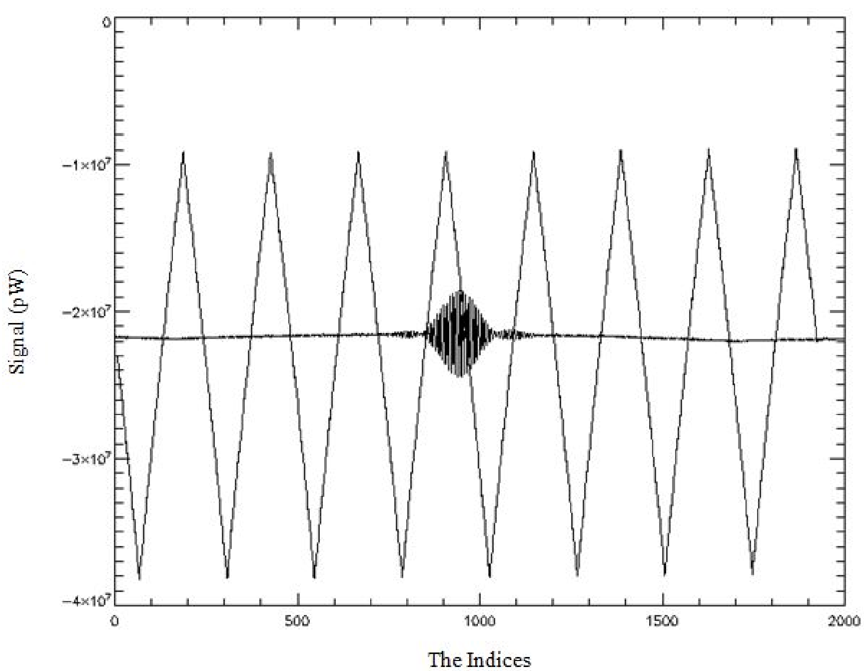

Figure 2.3: The calibration ramps of observation 20130907_007 bolomter (20, 20), superimposed with an interferogram.

each ramp, as shown in Figure 2.4. The amount of non-linearity can be determined to study the goodness of fit as a function of increasing order of polynomial, and by a comparing the values of reduced Chi-squared of each fit; the fit that gives reduced Chi-squared with the lowest order can be chosen.

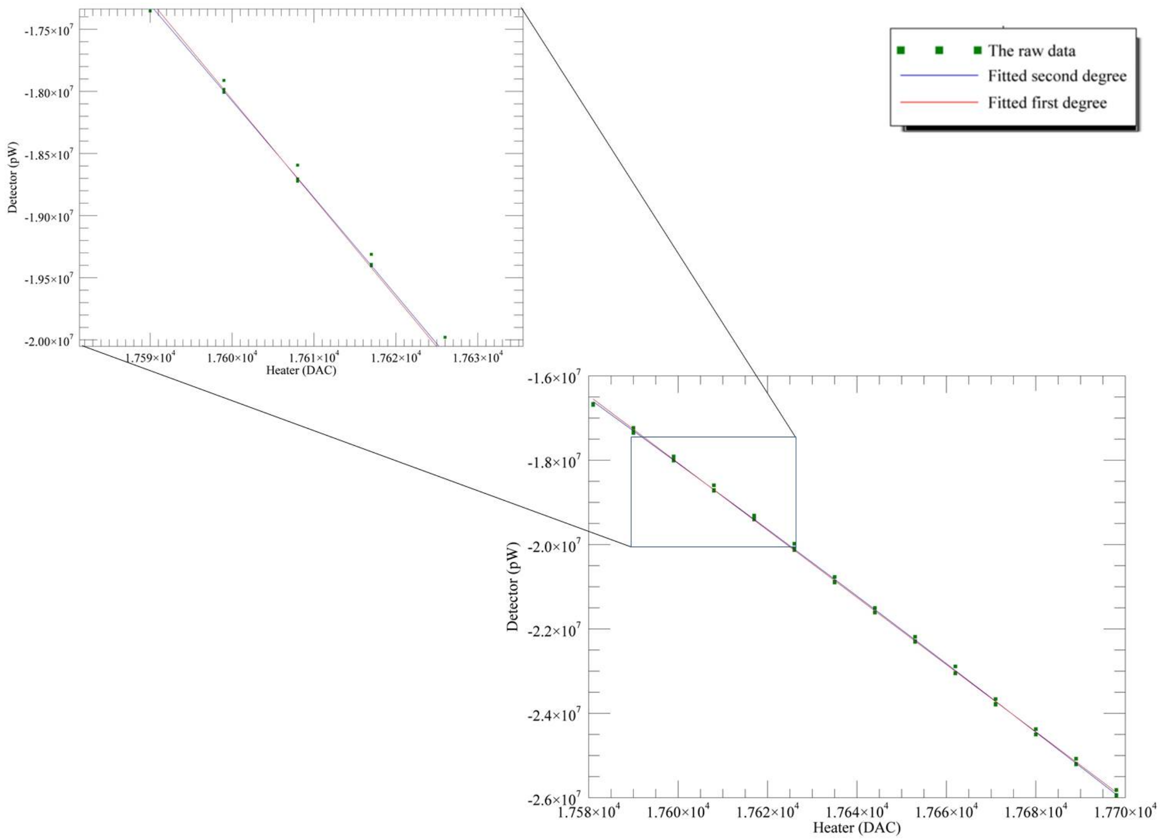

Figure 2.4: Shows the first and second degree polynomial fit to the first calibration ramp of observation (s8c20130907_0007) bolometer (20, 20); the insert shows a magnified region. It is clear that there is no significant difference and the bolometer exhibited a linear response

This calibration step is necessary to convert measured voltage units to detected power. When facing with spectra like the one showed in Figure 2.2, it was speculated that non-linearity can be of an important effect. Thus it was decided to study which degree of polynomial gave the lower reduced Chi-squared.

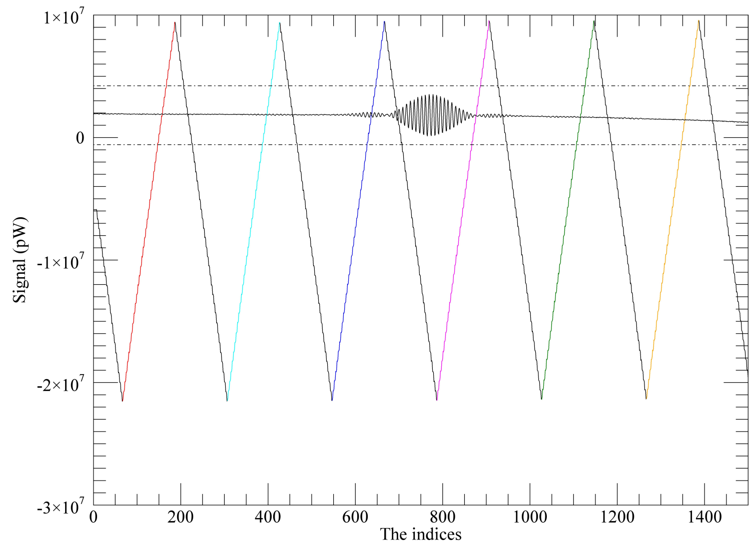

Figure 2.5: The calibration ramps of observation (s8c20130907_0007) bolometer (18, 23), where each ramp is identified from one another, taking a different colour, so a polynomial can be fitted to each one later on. The interferogram of the same bolometer is superimposed, with two horizontal dotted lines specifying the power range of analysis.

2.2.2 Calibration procedure

A typical calibration sequence is shown in Figure 2.5, where the heater temperature was increased and decreased through several cycles. The first step was to chop the ramps of each of the cycles, and then to fit polynomials with different degrees to each ramp. In order to get the best fidelity, fitting different degrees of polynomial was restricted to a range around the interferogram, as shown in Figure 2.5. Since in most cases the flux jumps are outside the interferogram power range, the fitting of the ramps was restricted to the power range of the interferogram. Figure 2.4 shows the first and second degrees of polynomials fitted to the first calibration ramp within the interferogram power range. Finally a statistical assessment is established as shown in Table 2.2, in which by comparing the values of Chi-squared, it shows which fit is better.

Table 2.2: A comparison of the first and second degree fits of the calibration ramps, observation (s8c20130907_002) bolometer (10, 27). The low values of reduced Chi-squared show that they were good fits.

	First degree	**Second degree**
The equation	$ax+b$	ax^2+bx+c
Mean (a)	-8.569×10^4	-23.763
Mean (b)	1.486×10^9	7.528×10^5
Mean (c)	N/A	-5.912×10^9
Mean (Chi-squared)	4.43×10^{-2}	4.445×10^{-2}
Standard deviation (a)	371.913	16.455
Standard deviation (b)	6.571×10^6	5.807×10^5
Standard deviation (c)	N/A	5.124×10^9
Standard deviation (Chi-squared)	8.714×10^{-3}	8.707×10^{-3}

2.2.3 Results

Using the the procedure described above, and from the comparison of fitting different degrees of polynomials to the ramps of bolometer (10, 27) observation (s8c20130907_002), shown Figures 2.3 and 2.4, it was found that the difference between the fits is small, as shown in Table 2.2.

The analysis showed that including higher order terms in the non-linear fit did not lead to a significant improvement, as seen in Table 2.2 and Figure 2.4, and the relation between the input signal and the readout of the detector was found to be linear in the majority of cases. It is clear that, what is sometimes regarded as non-linearity features (Figure 2.4) in the spectrum, or as non-linearity relation in the interferogram shown in Figure 2.6, is not just a simple non-linear relation between the input power and the measured signal, but rather a flux jump (which will be discussed in more details in Section 2.4) near the ZPD region with an accompanying non-linearity region, which is extending into the ZPD region. This explains why it masquerades as an apparent non-linearity in the spectral domain, as the interferogram shown in Figure 2.6 gave the spectrum shown in Figure 2.2.

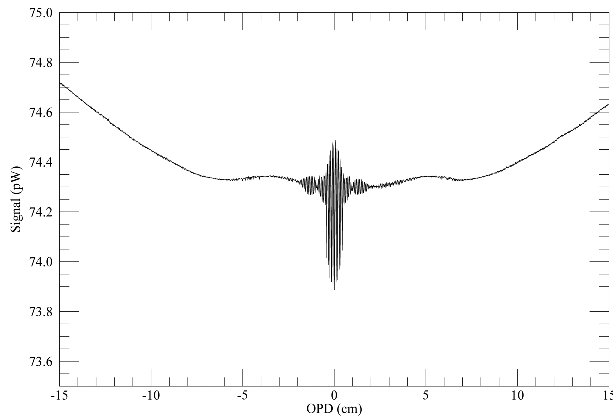

Figure 2.6: A raw interferogram with a flux jump in the ZPD region exhibiting as non-linearity, Observation (s8c20130813_00080) bolomter (25, 29).

2.2.4 Data calibration challenges

Fitting polynomials to essentially linear ramps (after identifying each one) is straightforward. However, it is sometimes complicated by the presence of flux jumps in the calibration ramps themselves that cannot be corrected, because the number of data points available in the ramps is not sufficient to correct for flux jumps. Nonetheless, since those flux jumps are not always in the interferogram range. Thus the ramps can be trimmed to a range around the interfergram values, this range is determined as $\pm 20\%$ beyond the range of the normalized ZPD signal. Figures 2.7 and 2.8 show examples of flux jumps occurring outside and inside the interferogram signal range, respectively. The analysis for Figure 2.7 is limited to the signal range of interferogram, on the other hand for bolometers like that showed in Figure 2.8, where a flux jump occurs within the interferogram range, further analysis is precluded.

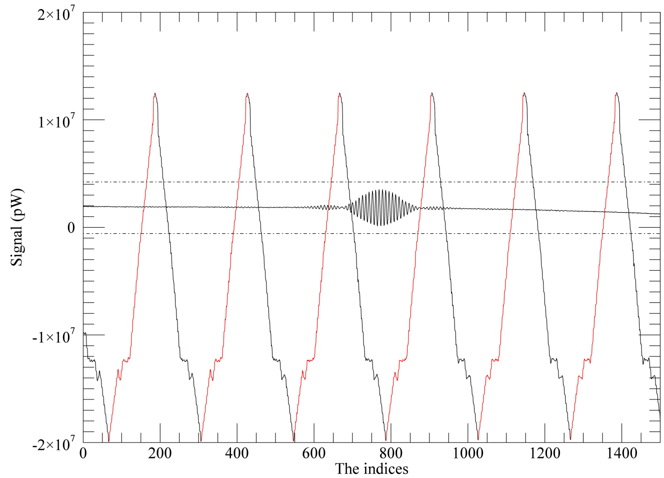

Figure 2.7: The calibration ramps with a flux jump outside the range of interferogram signal, where the analysis is limited to the interferogram range. Observation s8c20130907_0007 bolometer (26, 22).

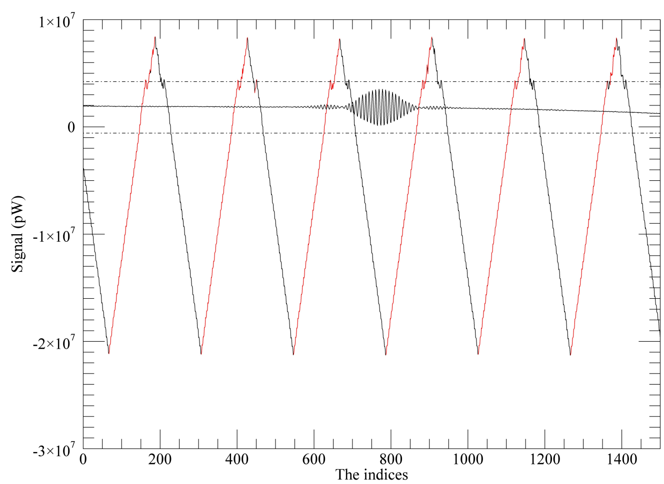

Figure 2.8: The calibration ramps with a flux jump inside the range of the interferogram signal precluding further analysis. Observation s8c20130907_0007 bolometer (20, 27).

2.3 Cosmic rays

2.3.1 Introduction

Cosmic rays are ionized nuclei (about 90% protons, 9% alpha particles and 1% heavier nuclei) with high energies (Gaisser, 1990). They are believed to emanate from outside our solar system, from sources such as supernovae and active galactic nuclei. The counting rate of cosmic rays is proportional to the altitude, Figure 2.9 shows the relation between the counting rate of cosmic rays and the altitude (Nave, 2012). They are also capable of producing showers of secondary particles, upon entering the Earth atmosphere causing what is called secondary cosmic ray shower. Since the James Clerk Maxwell Telescope is at an altitude of 4092 m (Johnstone, 2013), correction for cosmic rays is an important step to be taken into consideration for the correct interpretation of data.

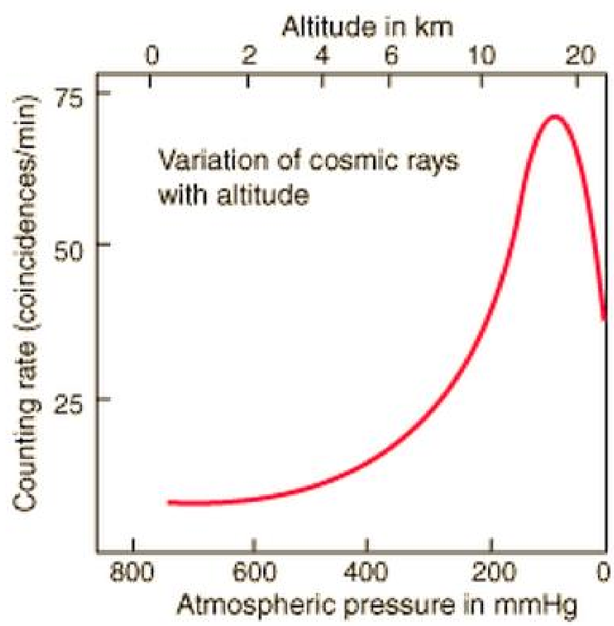

Figure 2.9: The relation between the counting rate of cosmic rays and the altitude (Nave, 2012).

Since cosmic rays can only deposit energy, they can only increase the temperature of the bolometer, artefacts caused by cosmic rays appear as spikes that are sudden increase in the signal, which then gradually fade away to the normal values. The gradual fading (the decay time) depends on the time constant of the detector, as it needs some time to recover from the sudden signal increase.

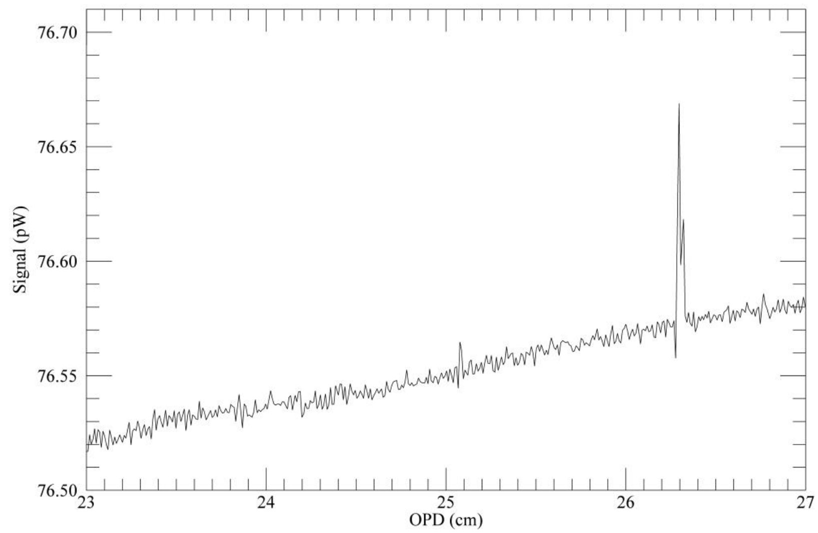

Figure 2.10: An interferogram with a cosmic ray at about 26.2 cm, observation (s8c20131119_00081) bolometer (10, 27).

2.3.2 Procedure

The purpose of this IDL procedure is to correct the interferogram by removing artefacts caused by cosmic rays, and recovering the normal values of the interferogram for these points. Like the flux jump correction procedure, the goal of this correction procedure is to identify and remove the noise component introduced by the cosmic ray. The IDL procedure can be introduced in steps as follows:

1. Obtain the derivative of the interferogram, as shown in Figure 2.11.

2. Identifying the spikes in the derivative, whose values are ten times the mean of the derivative. The threshold was chosen to be ten, so that any outlier point is not mistakenly regarded as a cosmic ray. Also after studying many bolometers it was found

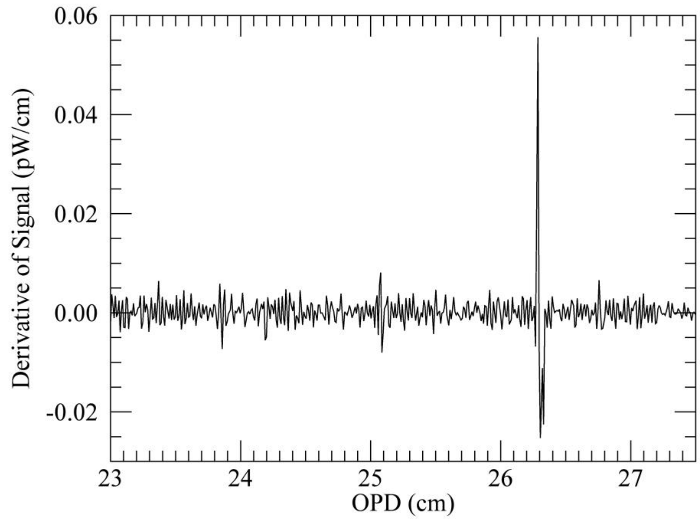

Figure 2.11: The derivative of the cosmic ray region in the interferogram. The sudden change in the interferogram caused by a cosmic ray is clearly shown at about 26 cm.

that the spike in the derivative, which is caused by a cosmic ray (as shown in Figure 2.11) is always larger than this threshold.

3. Regenerate the indices within each spike.

4. Replace the values at the indices (identified in step 3) by the mean value of small number of points around each cosmic ray point. The number of points is set to be 15, because the signal decays to the normal values after three points. Hence by setting the number of points to 15, we are certain to take points from both sides before and after the cosmic ray into the mean.

2.3.3 Results

Although this procedure was written to correct the cosmic rays, it also corrects the instabilities in the readout of the detector in the interferogram, which sometimes accompany the flux jumps. Figure 2.12 (top) shows an interferogram before the correction (where at about -35 cm there is an instability region in a flux jump and at about 26 cm there is a cosmic ray) overplotted by the interferogram after correction. Figure 2.12 (bottom left) is a magnified region showing the instability in the neighbourhood of a flux jump, while the figure at bottom right is a magnification of the cosmic ray region.

2.3.4 The challenges of cosmic rays correction

There are no significant issues with cosmic rays correction procedure. However, its ability to detect cosmic rays is limited to the regions outside the ZPD region, because of large dynamic range and modulated signal in the ZPD region. Also it might unintentionally correct some points around the cosmic rays which do not need to be corrected. This is insignificant because these points are too few in number, compared to those in the high resolution interferograms

2.4 Flux jumps

2.4.1 Introduction

The theory that underlies flux jumps has been presented in Section 1.6, here we discuss the impact of flux jumps on the data and how they can be identified and mitigated. The flux jumps are the most important challenge, because they lead to spectral artefacts in the Fourier transformed spectrum, as shown in Figure 2.13, which limit the information that can be extracted from the spectrum obtained with FTS-2. A statistical analysis (introduced in more detail in Chapter 3) of the first commission data indicated that, about 32 % of the bolometers exhibit flux jumps, with the majority of them located toward the centre of the field of view. A typical flux jump, as shown in Figure 2.13 (left), appears as a discontinuity in the interferogram accompanied with what seems to be a non-linearity region, this comes from the fact that the detectors consist of superconducting quantum interface devices (SQUIDs), as discussed in Chapter 1, where the SQUID is functioning in a FLL. The flux jump appears when the FLL loses its lock, due to high rate of change in the magnetic field from the TES, and relocks in a different quantize step, so the readout switch from one quantum state to another, shown as a discontinuity in the interferogram.Figure 2.13 (left)

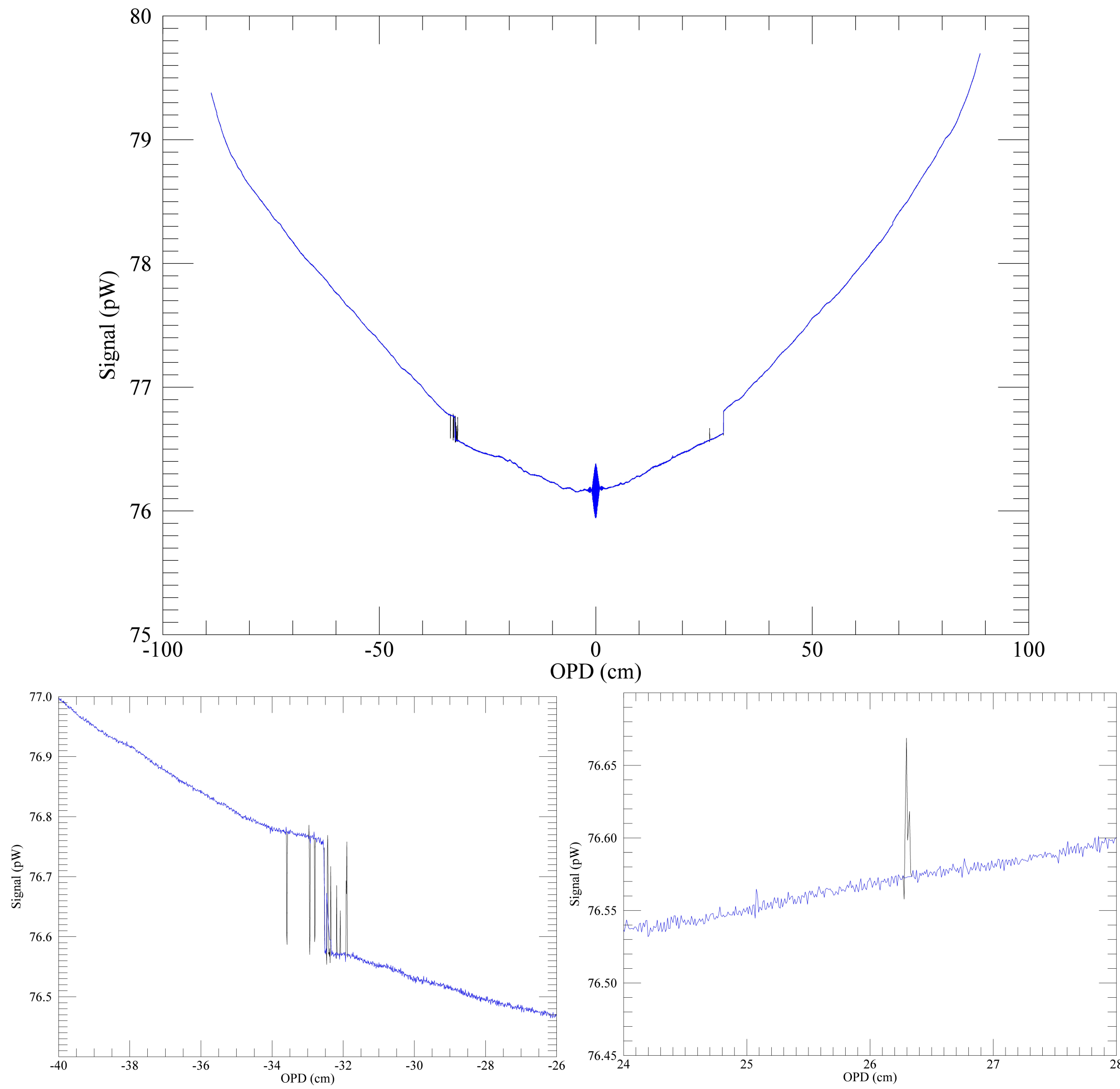

Figure 2.12: The figure in the top shows the interferogram before (black) and after cosmic rays correction (blue), where at about -35 cm there is an instability region in a flux jump, and at about 26 cm there is a cosmic ray. The figure in the bottom left is a zoom in on the flux jump instability region, and the figure in the bottom right is a magnified region showing the instability in the neighbourhood of a flux jump, while the figure at bottom right is a magnification of the cosmic ray region. Observation (s8c20131119_00081) bolometer (10, 27)

shows an interferogram with a flux jump.

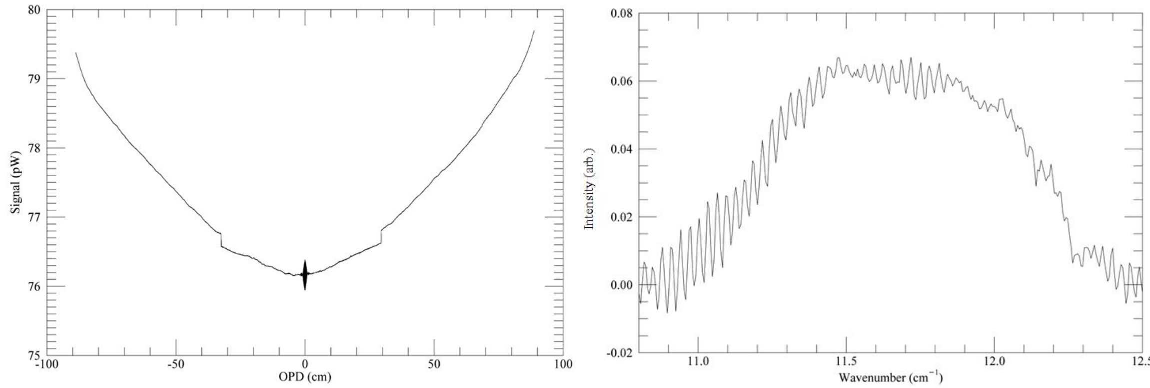

Figure 2.13: The interferogram with flux jumps at about -35 cm and 30 cm on the left. The obtained spectrum before correcting the flux jumps in the interferogram on the right. Observation (s8c20131119_00081) bolometer (10,27).

An IDL code was written to first identify the presence of flux jumps and then pick the interferograms with flux jumps, then mitigate the flux jumps and the accompanying non-linearity regions, using the information immediately before and after the flux jump.

2.4.2 Procedure

The procedure of flux jumps correction consist basically of two operations. First the detection of flux jumps, and second mitigating flux jumps.

Identification of flux jumps

Given their frequency, a robust and automatic flux jump detecting algorithm was required, where it is capable of interrogating every interferogram, and look in every bolometer for the presence of flux jumps. This algorithm is required to work in a way that it neither misses a flux jump, nor takes too long to process the 1280 bolometer interferograms for every sub-array and for every scan obtained with FTS-2. Since the identification of flux jumps was based on a differential method, it cannot be used in the ZPD region. In fact it is very difficult to identify a flux jump within the ZPD region, because of the high modulation that occurs in this region. Thus, we obtain the derivative of the interferogram outside the

ZPD region (from -5 cm to 5 cm), as shown in Figure 2.14, in which any spike (greater than ten times the mean of the derivative) is obtained as flux jumps in this region of the interferogram.

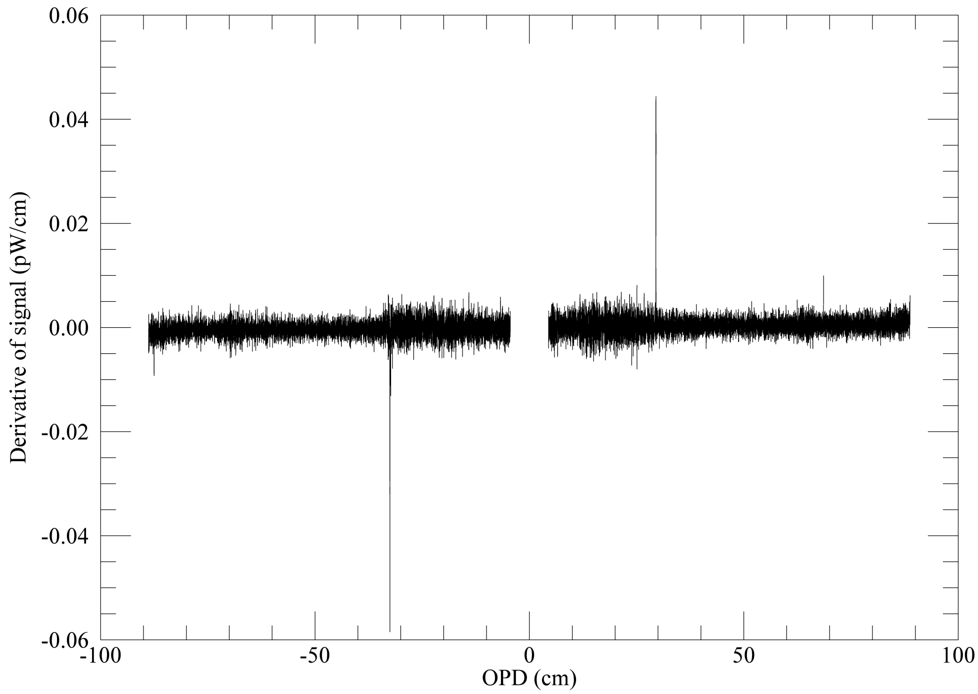

Figure 2.14: The derivative of the interferogram obtained from the first step, where the flux jumps appear as spikes.

Mitigating flux jumps

The second half of the procedure of flux jumps correction is to be able to fix as many flux jumps as possible, such that the interferogram after the correction process is of sufficient quality to allow scientific analysis. Flux jumps themselves are easy to identify, however, near the flux jump the response becomes non-linear, so not only the flux jump needs to be corrected but also the non-linearity region accompanying it. This part can be summarized in the following steps;

1. Identifying the regions (before flux jump, the non-linearity, and after the non-linearity region), where the length of every one of them is 6% of the total number of points

of the interferogram. The 6% was chosen for three reasons; First, in case of the high resolution interferograms each region will be about 1200 points, which from a study of many bolometers; it was shown that in most cases the non-linearity region is about 1200 points. Second, since the flux jumps occur at different OPD values, it was a reasonable trade off to be able to correct as many flux jumps as possible.

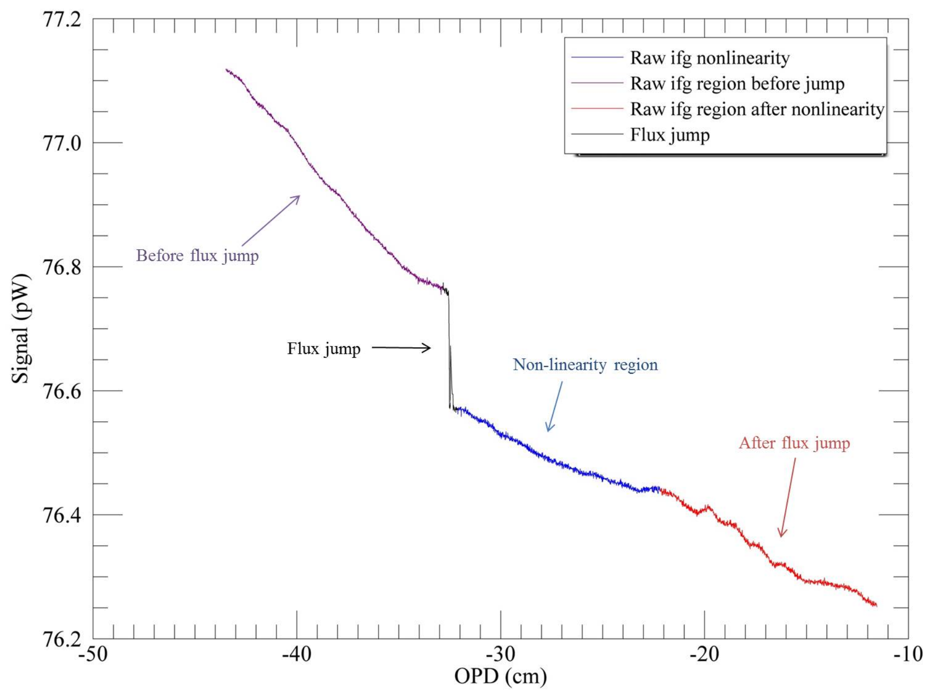

Figure 2.15: The different identified regions (before flux jump, the non-linearity, and after the non-linearity region) of the interferogram, observation (s8c20131119_00081) bolometer (10, 27). The regions that need to be corrected are the non-linearity region in blue, and the flux jump in black.

2. Fit a second degree polynomial to each region, as follows:

$$\begin{aligned} b(x) &= b_3 x^2 + b_2 x + b_1 \\ nf(x) &= n_3 x^2 + n_2 x + n_1 \\ a(x) &= a_3 x^2 + a_2 x + a_1, \end{aligned} \tag{2.3}$$

where a, nf and b are the second degree fits (as functions of, x, the OPD) for the regions (Figure 2.15) before non-linearity (purple), non-linearity (blue), and after non-linearity region (red), respectively. Figure 2.16 shows the different identified regions, and their fitted polynomials.

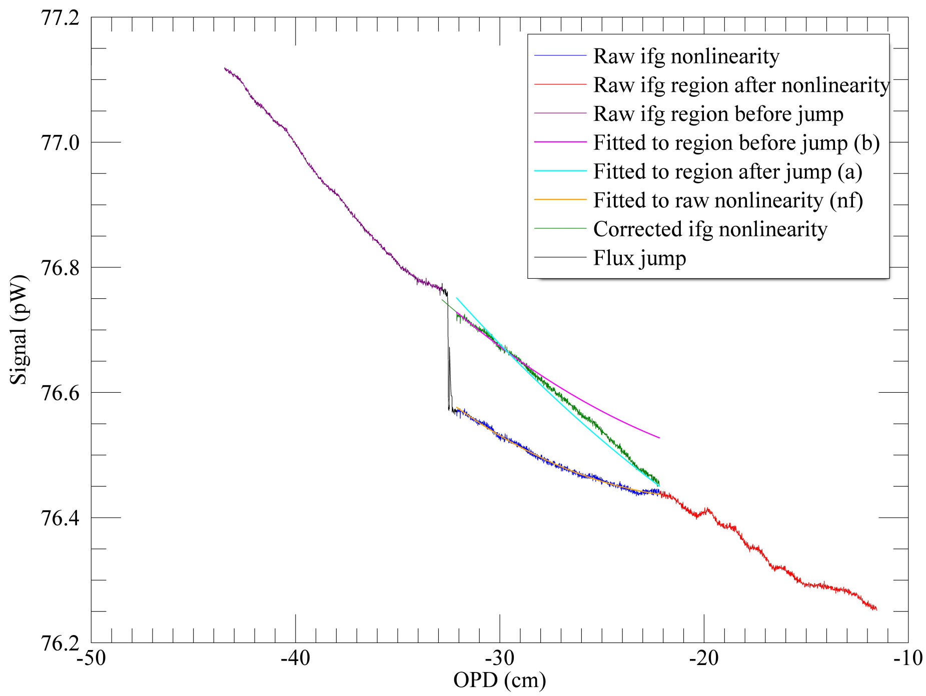

Figure 2.16: The different identified regions of the interferogram and the fits to each region, observation (s8c20131119_00081) bolometer (10, 27). The legend shows the region of the raw interferogram (*nonlinear* in blue) and the fitted polynomials (b, a and nf in magenta, cyan and orange, respectively), which will be used in Equation 2.4.

3. Generate weighting factors z and y for the points that are to be corrected. The values of the weighting factors are fractions from 0 to 1, depending on the proximity of the point to each of regions, where z and y correspond to the fitted curves before b and after a the flux jump, respectively. For example in Figure 2.16, at the closest point in the non-linearity region to the region after flux jump, the values of the weighting factors are $z = 0$ and $y = 1$, while at at the midpoint of the non-linearity region, the values of the weighting factors are $z = y = 0.5$.

4. Correct the flux jumps by using the equation,

$$Corrected = \frac{((z \times b) + (y \times a)) \times nonlinear}{nf}, \quad \text{(W)} \quad (2.4)$$

where b, a and nf are the second degree polynomial fits for the regions before flux jumps, after flux jumps and the non-linearity, respectively, z and y are the weighting factors, and $nonlinear$ is the raw non-linearity region.

5. Repeat the procedure for every flux jump in the interferogram, Figure shows the correction of the second flux jump in the same interferogram in Figure 2.16.

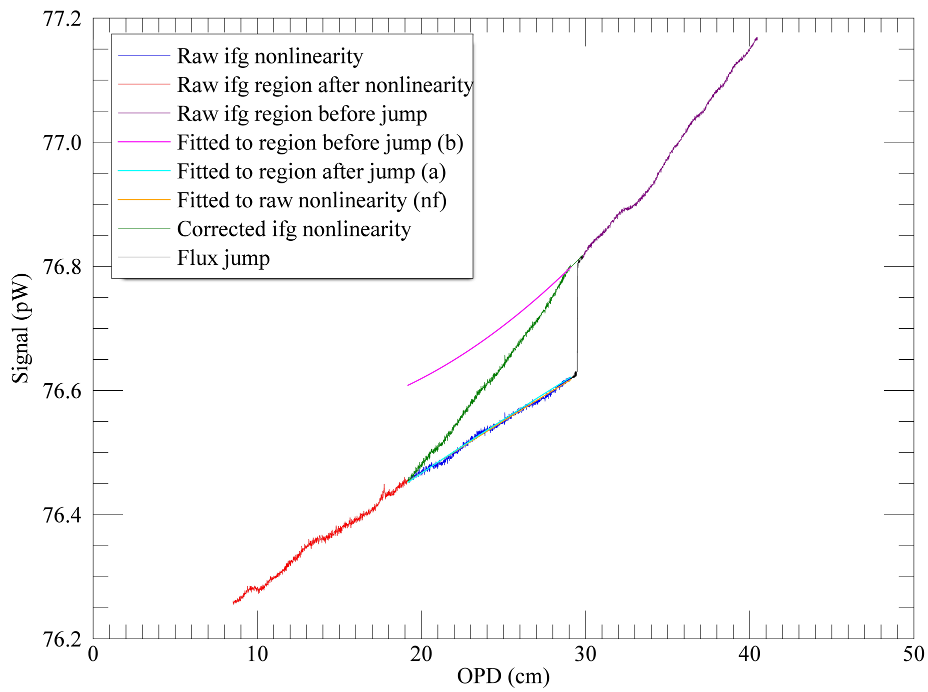

Figure 2.17: The different identified regions of the interferogram and the fits to each region around the second flux jump, observation (s8c20131119_00081) bolometer (10, 27). The legend shows the region of the raw interferogram (*nonlinear* in blue) and the fitted polynomials (b, a and nf in magenta, cyan and orange, respectively), which will be used in Equation 2.4.

6. Reconstruct the interferogram with the corrected flux jump regions.

2.4.3 Results

Figure 2.18 shows the interferogram before and after the corrections. Flux jumps correction algorithm made a significant improvement to the spectra, as shown in Figures 2.19 and 2.13. It is clear that the spectrum before the correction process cannot be used, while the spectrum after correction resembles a typical FTS-2 spectrum, as shown in Figure 2.19, and the presence of the line of molecular oxygen at 12.292 cm^{-1} can be seen.

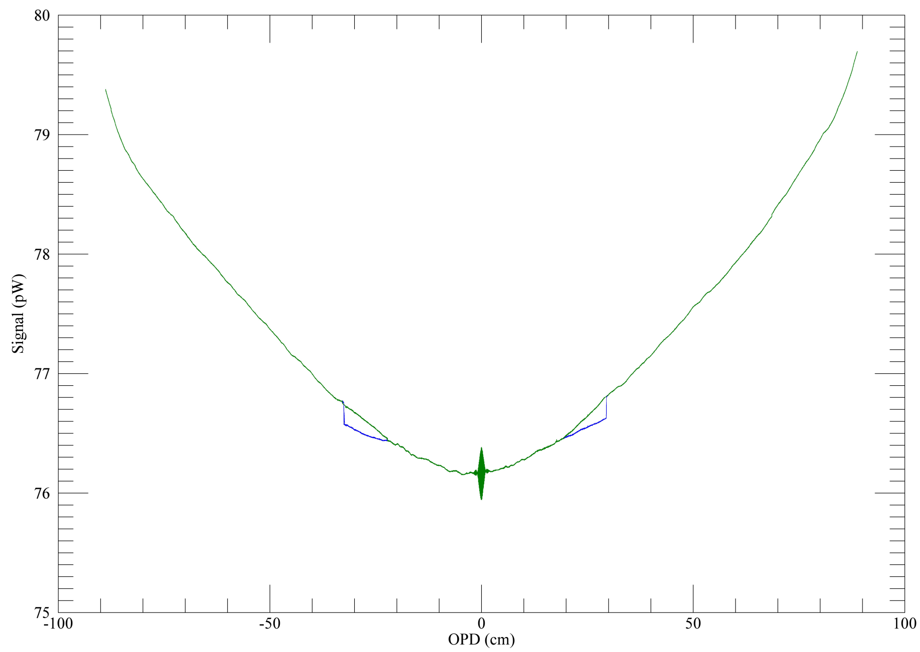

Figure 2.18: The raw interferogram in blue and the corrected one superimposed in green, and it is obvious that the correction procedure succeeded in retrieving the interferogram.

2.4.4 Challenges to the flux jump correction

Although the algorithm used to correct the flux jumps generally improved the data quality, and was written to be as flexible as possible, there were some challenges limiting its performance, putting constraints on its ability to succeed in all the cases. Figure 2.20 shows different cases of interferograms exhibiting flux jumps.

The challenges and constraints are mentioned as the following;

- The non-linearity region length is set to a number of points (six percent of the total number of points), which although it was found to give the optimum results for most cases, it might not be the best option for a given case.

- If the non-linearity region is too close to the ZPD region it cannot be corrected, because there are not enough points to be used for correction outside the ZPD region,

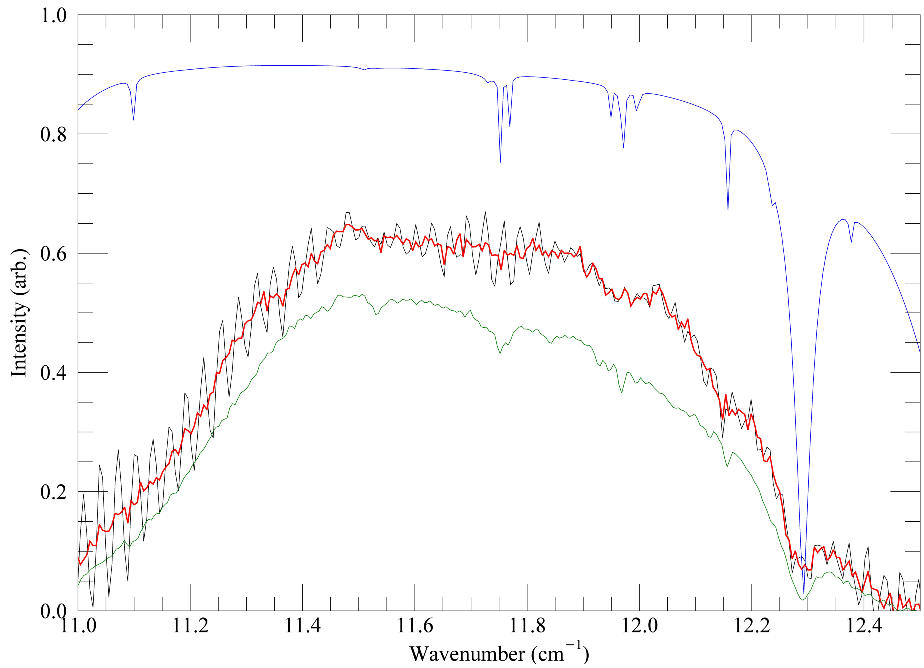

Figure 2.19: The spectrum after correcting the flux jumps in the interferogram (red), superimposed by the spectrum before the correction procedure (black), the atmosphric transmission obtained from BTRAM (blue), and a typical spectrum obtained with FTS-2 (green). The retrieved spectrum resembles the typical spectra obtained using FTS-2, and the presence of the line of molecular oxygen at 12.291 78 cm^{-1} can be seen.

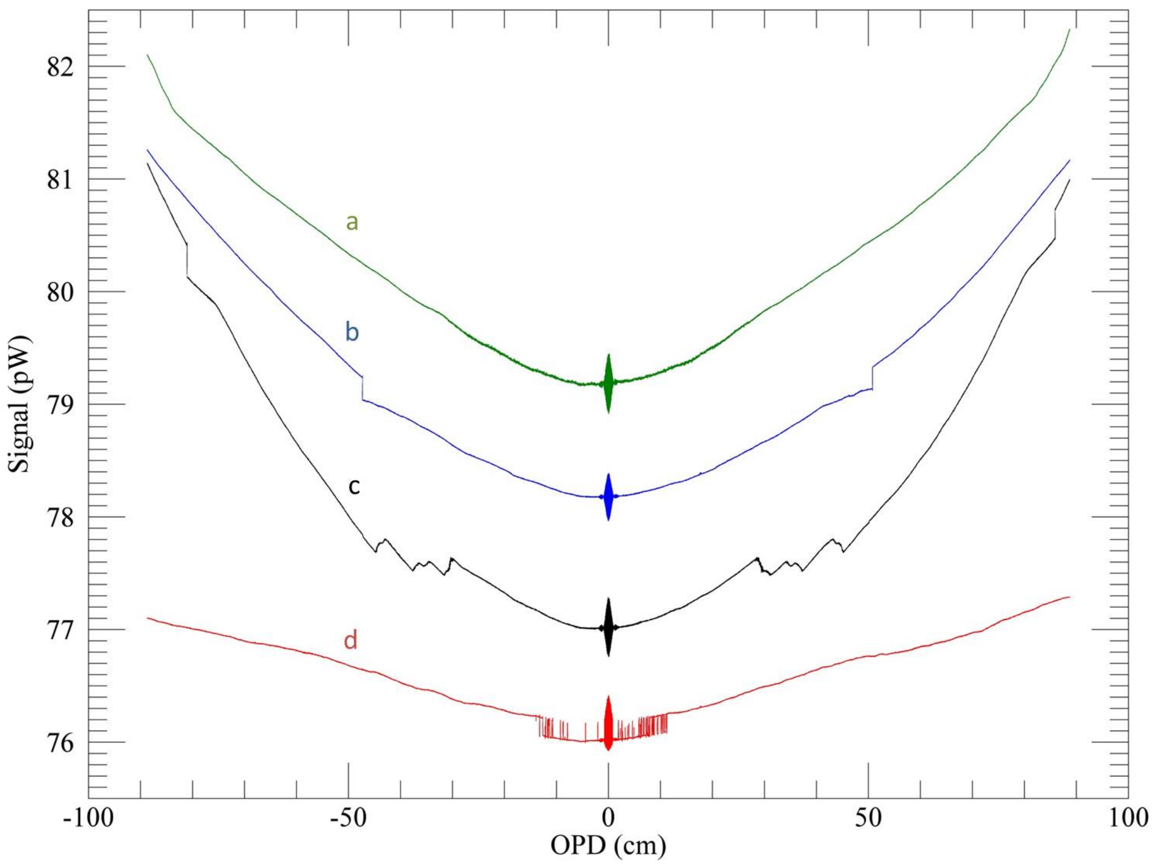

Figure 2.20: Different types of interferograms from observation (s8c20131119_00081), where (a) in green is a very good interferogram obtained from bolometer (11, 24), (b) is the interferogram from bolometer(24, 26) having flux jumps at about -50 cm and 50 cm that can be corrected. On the other hand (c) in black and (d) in red are examples of those interferograms that cannot be corrected because, in (c) there are more than two flux jumps in the interferogram bolometer (24, 32), while (d) is an interferogram with flux jumps and non-linearity in the ZPD region bolometer (17, 27).

as seen in the interferogram in red in Figure 2.20.

- If the non-linearity region is too close to the edge of the interferogram, the flux jump will be trimmed (not corrected), as shown in Figure 2.21.

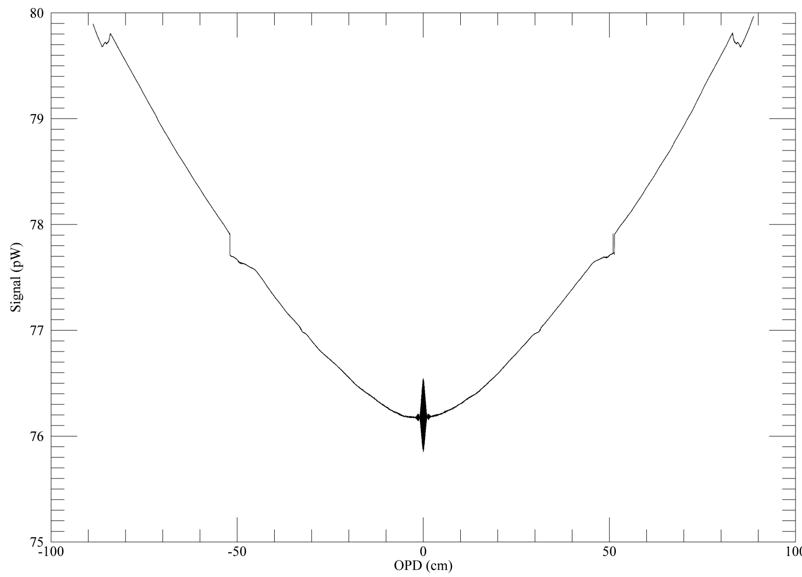

Figure 2.21: An interferogram with more than flux jump two flux jumps but the interferogram can be trimmed to certain range from -80 cm to 80 cm, then the flux jumps at -50 cm and 50 cm can be corrected, observation (s8c20131119_00081) bolometer (13, 19).

- If there is more than one jump in each half of the interferogram, the interferogram cannot be corrected, because the regions around each flux jump are not reliable as they also need correction, as seen in the interferogram in black in Figure 2.20.

2.5 Conclusions

A number of procedures were written to overcome the issues found in analysing the FTS-2 data from the commissioning runs. First we investigated how the input signal is related to readout and it was shown to be linear. Second the procedures for identification and where possible mitigation of flux jumps and cosmic rays were discussed. Table 2.3 summarizes the purposes and the challenges of each procedure. The cosmic rays correction procedure successfully identified and mitigated almost all the cosmic rays artefacts in the

Table 2.3: A summary of the procedures, which were made to invistigate the relation between the input signal and the detectors readout, and for flux jumps and cosmic rays corrections, showing the purposes and the challenges of each procedure.

The name	**The purpose**	**The challenges**
Calibration from heater ramps	Investigate the input-readout relation, important to retrieve the input stellar signal.	Some ramps endure flux jumps which makes it very hard correct and obtain a relation.
Flux jump correction	Correct for the flux jumps, extremely important as a flux jumps can make the spectrum unusable.	Many restrictions on the location of the flux jump, and no more than two can be corrected in one interferogram.
Cosmic ray correction	Correct for the cosmic rays, the counting rate increases with altitude.	Some points might get unnecessarily corrected.

interferograms. Although the flux jumps correction procedure managed to identify almost all flux jumps, it succeeded to mitigate roughly about 40% of the flux jumps. Thus we investigated whether there were implementation aspects that can minimize the frequency of flux jumps. After discussing the issue with Dr. Bentley, it was found possible to re-bias the detectors. In the new regime the flux jumps exist in about 18% percent of interferograms, and the correction procedure is able to correct a bigger fraction of those that still remain.

Chapter 3

The Spectral Response of SCUBA-2

3.1 Introduction

SCUBA-2 is a wide-field sub-millimetre bolometer camera operating at the James Clerk Maxwell Telescope, which provides simultaneous images in two filter bands at 450 µm and 850 µm matched to the high atmospheric transmission ”atmospheric windows”. Figure 3.1 shows the locations of 450 µm and 850 µm bands, which match the regions of high atmospheric transmission.

Several filters are used to define these two bands, the filters specifications are given in Tables 3.1 and 3.2. The filter profiles were measured before their installation in SCUBA-2 (Holland et al., 2013) Figure 3.2 shows the profile of each filter. It should be noted here that the measurements of these filter profiles were performed individually at room temperature. However when filters are combined in series, spectral artefacts are often introduced, due to optical resonant cavities between the filters themselves. Furthermore, it was not possible to measure these artefacts in the laboratory prior to full assembly and integration of the entire system.

The characterization of the SCUBA-2 spectral response is necessary, in order to interpret correctly the photometric measurements of astronomical sources observed with SCUBA-2. Figure 3.3 is an illustrative diagram of the locations of the filters upon installation with the filters colour coded according to their operating temperatures.

This chapter discusses number of issues, where the next section shows how the FTS-2 measurements were performed, Section 3.4 shows how the data were analysed and com-

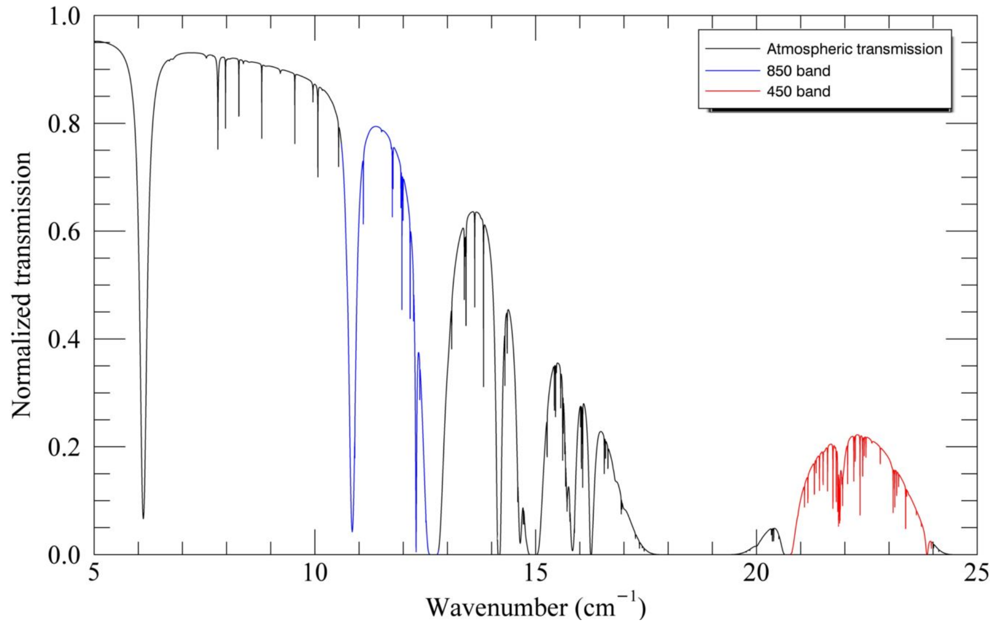

Figure 3.1: The theoretical atmospheric transmission above Mauna Kea for 0.5 mm PWV produced by BTRAM (Chapman, Naylor, Gom, Querel & Davis-Imhof, Chapman et al.). The blue and red regions represent the 450 µm and 850 µm bands of high atmospheric transmission.

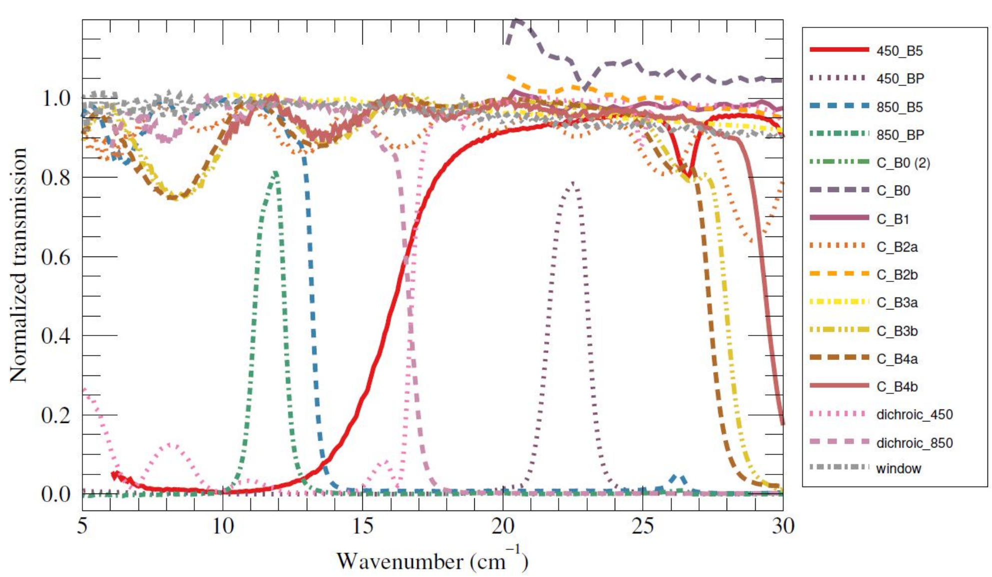

Figure 3.2: The individual spectral profiles of the optical components within SCUBA-2 (Holland et al., 2013).

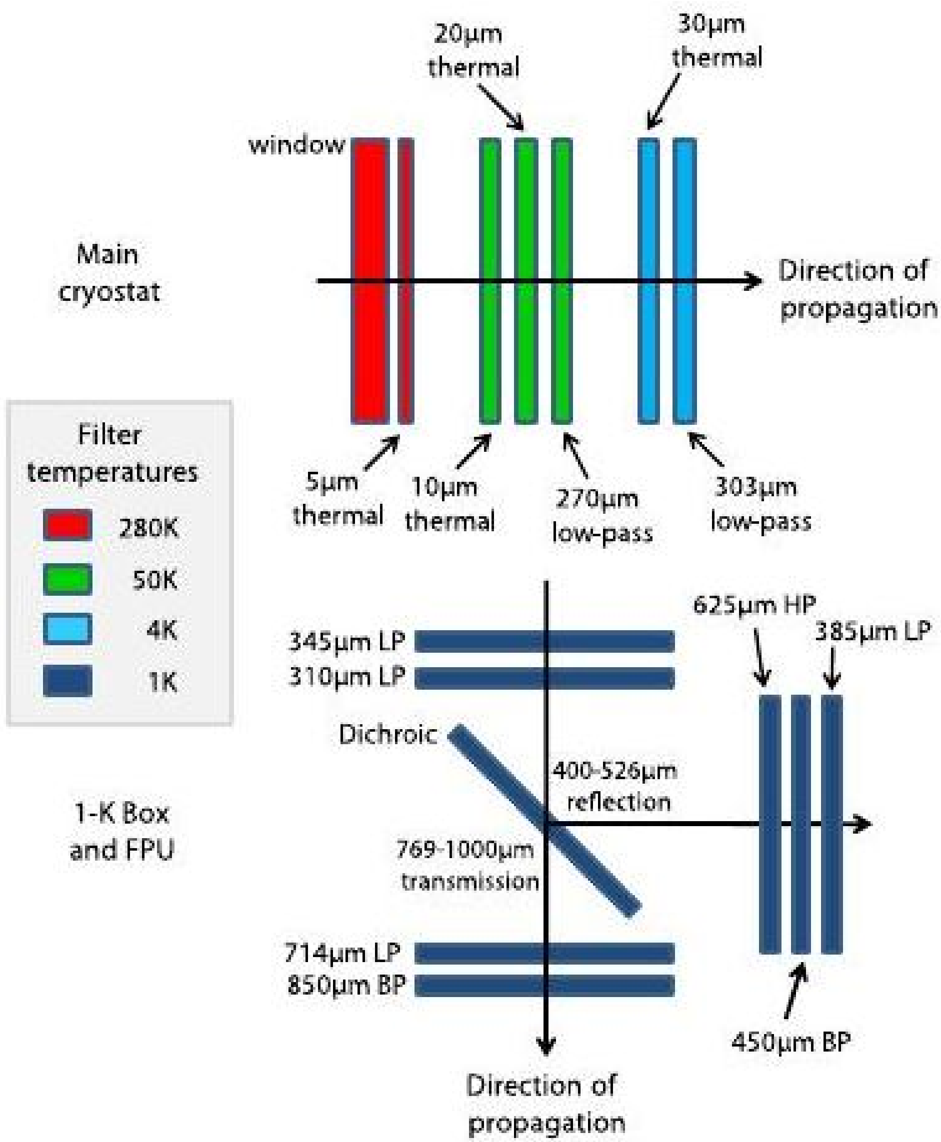

Figure 3.3: Schematic of the filters installed in SCUBA-2 and their operating temperatures; BP, LP and HP represent band-pass, low-pass and high-pass, respectively (Holland et al., 2013).

Table 3.1: Specifications of the SCUBA-2 filters (from the Joint Astronomy Centre JAC).

Filter location	Filter name	Temperature (K)	Pass band (cm^{-1})	Transmission (%)
Window	450	300	$21.1 - 23.5$	> 90
	850	300	$11 - 12.3$	> 90
Behind 300 K window	C_B0	300	$5 - 30$	> 95
Radiation shield outer	C_B1	60	$5 - 30$	> 95
Radiation shield middle	C_B2b	60	$5 - 30$	> 95
Radiation shield inner	C_B2a	60	$5 - 30$	> 95
Helium shield	C_B3a	4	$5 - 30$	> 95
Helium shield	C_B3b	4	$5 - 40$	> 90
Cold stop (outer)	C_B4a	1	$5 - 40$	> 90
Cold stop (inner)	C_B4b	1	$5 - 40$	> 90
Array edges	450_B5	0.1	$20-$ optical	> 90
	850_B5	0.1	$10 - 16$	> 90
Array bandpass	450_BP	0.1	$21.1 - 23.5$	> 70
	850_BP	0.1	$11 - 12.3$	> 70

Table 3.2: Specification of the SCUBA-2 diachronic filter (from the Joint Astronomy Centre JAC).

Filter name	**Temperature (K)**	**Reflection**		**Transmission**	
		Frequency (cm^{-1})	Transmission (%)	Frequency (cm^{-1})	Transmission (%)
Dichronic	1	19-25	> 90	10-13	> 90

pares the results obtained with the theoretical predictions. Section 3.5 shows how the spectral response is used for correct interpretation of observations performed with SCUBA-2 and FTS-2.

3.2 Determining the Spectral Response of SCUBA-2

FTS-2 was designed in a Mach-Zehnder configuration with full access to its four ports (two input ports and two output ports) (Naylor et al., 2006). As mentioned in the first chapter, each output port measures the difference between radiation entering the two input ports of the interferometer. By placing a black body in each input port, where one black body has a heating pad attached to it, while the other is left at ambient temperature, the resulting spectrum at each output port can be combined with the Planck radiation law, to provide the spectral response of SCUBA-2. The spectrum measured can be expressed as:

$$O(\sigma) = F(\sigma)\eta[\varepsilon_A B(\sigma, T_A) - \varepsilon_B B(\sigma, T_B)]A\Omega \qquad (\text{W (cm}^{-1})^{-1}) \quad (3.1)$$

where $F(\sigma)$ denotes the spectral response of SCUBA-2 as a function of wavenumber, η is the system efficiency, ε_A and ε_B are the emissivity of the two black bodies, $B(\sigma,T)$ is the spectral radiance for each black body, one at temperature T_A, the other is at T_B, and $A\Omega$ is the illuminated area solid angle product. The spectral radiance $B(\sigma,T)$ is expressed by the Planck function as:

$$B(\sigma,T) = 2hc^2\sigma^3 \frac{1}{\exp[hc\sigma/kT]-1} \qquad (\mathrm{W\ sr^{-1}m^{-2}(cm^{-1})^{-1}}) \tag{3.2}$$

where, σ is the wavenumber, T is the temperature, h is the Planck constant, c is the speed of light and k is the Boltzmann constant. In the case of an ideal interferometer one observation is required to identify the spectral response of SCUBA-2. However, because of a lack of symmetry between the optical paths from the two ports in the interferometer, two observations are required. In this case, since the interferometer observation provides a differential measurement between the two ports, thus by taking the difference between two observations, the input port with a constant temperature black body is cancelled out, removing the systematic errors within the interferometer. Using Equation 3.1, the two observations can be expressed by:

$$O_1(\sigma) = F(\sigma)\eta[\varepsilon_A B(\sigma,T_{A_1}) - \varepsilon_B B(\sigma,T_B)]A\Omega \qquad (\mathrm{W\ (cm^{-1})^{-1}}) \tag{3.3}$$

$$O_2(\sigma) = F(\sigma)\eta[\varepsilon_A B(\sigma,T_{A_2}) - \varepsilon_B B(\sigma,T_B)]A\Omega \qquad (\mathrm{W\ (cm^{-1})^{-1}}) \tag{3.4}$$

T_{A_1} and T_{A_2} are the two temperatures of the heated black body in the two observations. Taking the difference between both observations gives:

$$O_2(\sigma) - O_1(\sigma) = F(\sigma)\eta\varepsilon_A[B(\sigma,T_{A_2}) - B(\sigma,T_{A_1})]A\Omega \qquad (\mathrm{W\ (cm^{-1})^{-1}}) \tag{3.5}$$

As the resulting spectrum is the multiplication between the source spectral index and the spectral response of SCUBA-2, the spectral response can be obtained by dividing the two measurements by the difference between the Planck functions with corresponding temperatures, as follows:

$$SRF(\sigma) = \frac{O_2(\sigma) - O_1(\sigma)}{B(\sigma, T_{A_2}) - B(\sigma, T_{A_1})} \tag{3.6}$$

It should be noted here that, for simplicity the right hand side in Equation 3.6 is normalized for efficiency, emissivity and the product of the illuminated solid angle (both assumed to be constant).

3.3 SCUBA-2 bias settings

3.3.1 The first set of observation

Several observations of black body sources were taken, each consisting of three high resolution ($0.0056\,\mathrm{cm}^{-1}$) scans with Nyquist frequency of $50\,\mathrm{cm}^{-1}$ and acquisition time of 34.6 s. In order to simulate black body radiation sheets of Eccosorb were used because of its high emissivity at these wavelengths (Laird-Technologies). One of the sources was held at ambient temperature while the temperature of the second was changed, as shown in Table 3.3.

Table 3.3: Observing parameters for the first set of observations, where the black body in port s8d was held at constant temperature, while the second in port s8c was operated at different temperatures with an uncertainty of $\pm 0.5\,^{\circ}$C.

Port 2 (s8c)	**Port 1 (s8d)**	**No. of scans**
Load 26 °C	Ambient 11 °C	3
Load 15.5 °C		
Load 15 °C		
Load 35.7 °C		
Load 35.7 °C	Ambient 11 °C	3
Load 36.6 °C		
Load 48.8 °C		
Load 49.4 °C		

In these initial observations the presence of a low frequency oscillation in the interfer-

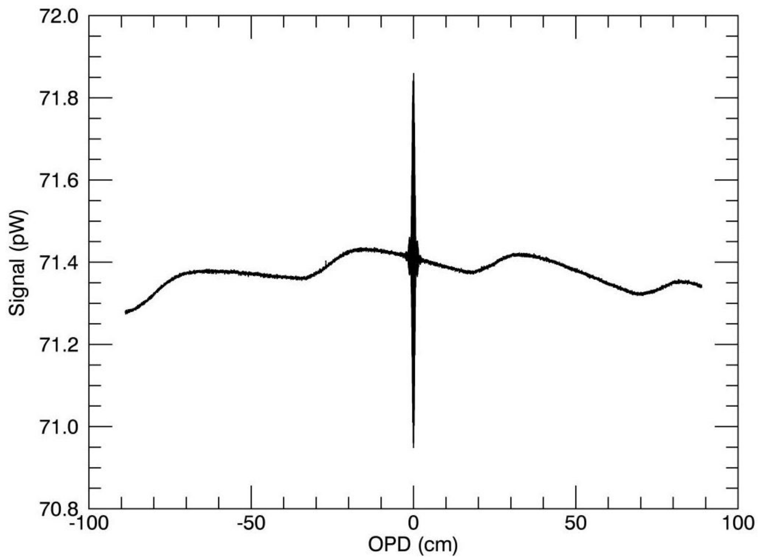

Figure 3.4: The raw interferogram of the 850 µm band port (C) bolometer (19, 20) showing the baseline drift/low frequency oscillation, observation s8c20131203 – 00011 – 0301.

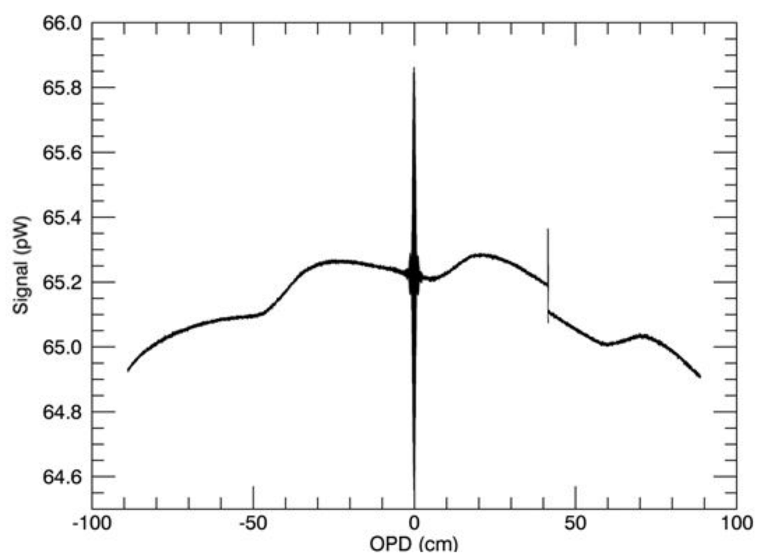

Figure 3.5: The raw interferogram of the 850 µm band port (C) pixel (25, 22) showing the presence of a flux jump.

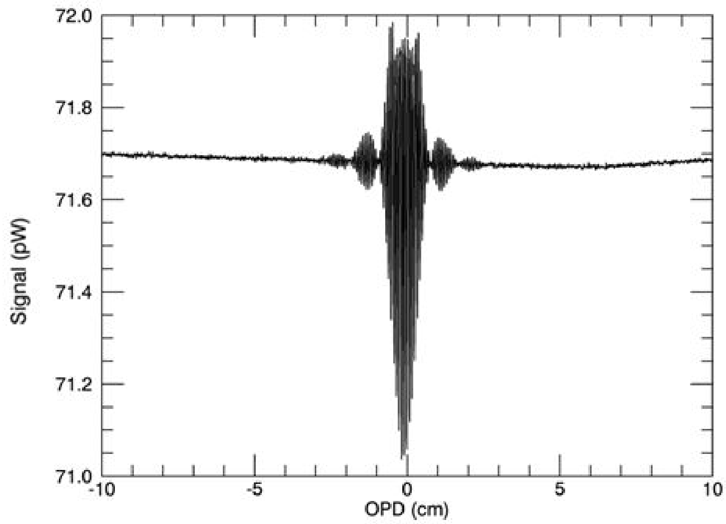

Figure 3.6: The interferogram of the 850 µm band port (C) bolometer (20, 20), having a flux jump in the zero path difference region.

ogram is clearly seen (see Figure 3.4). Also in some cases the presence of flux jumps is observed, as shown in Figure 3.5. In this case, the low frequency oscillation could be miss interpreted as flux jumps, so the algorithm failed. Hence, in order to overcome this challenge the interferogram was trimmed to a small range around the ZPD point ($-10\,\mathrm{cm}^{-1}$ to $10\,\mathrm{cm}^{-1}$). However, even with this trimming, it cannot eliminate the flux jumps that occur in the ZPD region, see Figure 3.6.

3.3.2 The second set of observation

Following the analysis of flux jumps discussed above, we had a discussion with Dr. Dan Bentley in the Joint Astronomy Centre (JAC), an expert in the TES detectors, about the best way to avoid flux jumps. He suggested that it would be possible to re-bias the detectors, so that the bolometers do not exhibit as many flux jumps. A second set of observations (shown in Table 3.4) was taken with the bias setting changed.

It was immediately evident that with re-biasing the settings, most bolometers did not exhibit flux jumps. However, to asses the improvement in a statistical manner, a comparison was made between the power in the fundamental band and the power in the harmonics. Since flux jumps when they do exist in the ZPD region, give rise to non-linearity fea-

Table 3.4: Observing parameters for the second set of observations, where the black body in port s8d was held at constant temperature, while the second in port s8c was operated at three temperatures with an uncertainty of $\pm 0.5\,°C$

Port 2 (s8c)	Port 1 (s8d)	No. of scans
Load 16.8 °C	Ambient 7.7 °C	10
Load 25.3 °C	Ambient 8.1 °C	10
Load 34 °C	Ambient 8.4 °C	10

Table 3.5: A statistical comparison between the first and second sets, where scans with no data are those filled with (NaN; not a number), the bad scans are those with signal-to-noise ratio less than the threshold (30).

	First set	Second set
Total number of scans	19200	23040
Scans with no data	7932 (41 %)	8109 (35.2 %)
Bad scans	6191 (32.2 %)	4242 (18.4 %)
Good scans	5077 (26.4 %)	10689 (46.4 %)

tures, which appear as power leakage from the fundamental band to the harmonic bands, as shown in Chapter 2. Thus the assessment of whether the bolometers in the second set of observations had non-linearity features, enables one to quantify the amount of bolometers exhibiting flux jumps. Also a more detailed comparison between both sets of observations was necessary, in order to probe the effect of re-biasing on the signal-to-noise ratio.

3.3.3 Non-linearity

Non-linearity, as discussed in the previous chapter, occurs when there is a non-linear relation between the input signal and the detector signal. It appears as power in the harmonic bands (see Figure 2.2) which decreases the signal within the band in favour of the harmonic band power. Thus, to investigate the presence of non-linearity, we integrated the area over one of the harmonic bands ($22\,\mathrm{cm}^{-1}$ to $25\,\mathrm{cm}^{-1}$ for the $850\,\mu\mathrm{m}$) and divide this by the power within the signal band ($11\,\mathrm{cm}^{-1}$ to $25\,\mathrm{cm}^{-1}$). The acceptable range for this ratio was set to be less than 0.1, based on previous analysis (Jones, 2010). We applied this algorithm on the bolometers and the statistical results are shown in histograms, Figures 3.7, 3.8 and 3.9, one for each temperature of the three (16.8 °C, 25.3 °C and 34 °C), showing the number of bolometers versus the percentage of signal in the harmonic to that of the band.

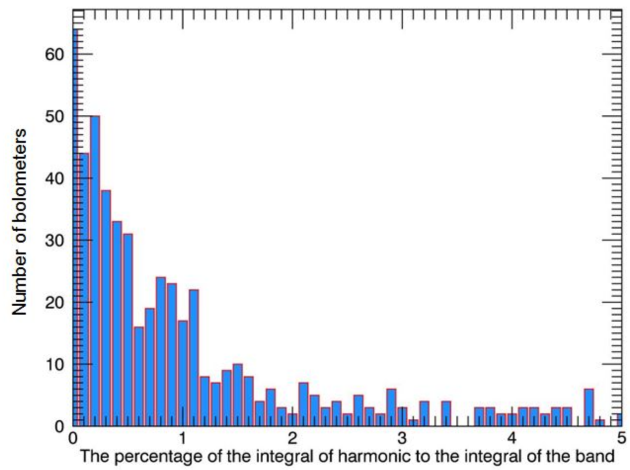

Figure 3.7: The number of bolometers versus the percentage of the integrals of the area of the harmonic to that of the band, for temperature 16.8 °C.

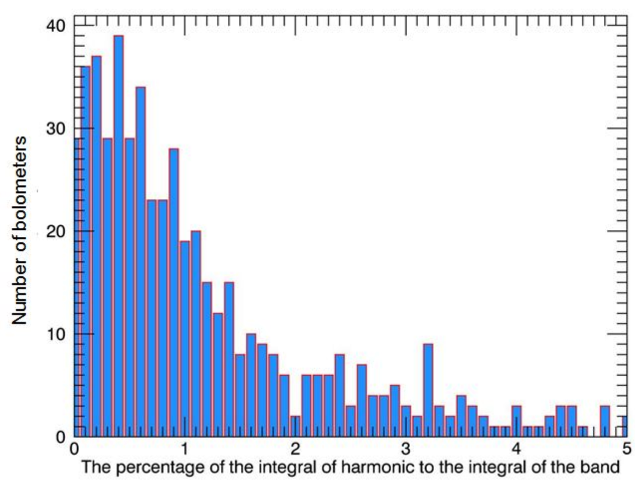

Figure 3.8: The number of bolometers versus the percentage of the integrals of the area of the harmonic to that of the band, for temperature 25.3 °C.

In this analysis a noisy bolometer will also fail this test and can be mistakenly regarded as a non-linear bolometer. Another method to specify how many bolometers exhibited non-

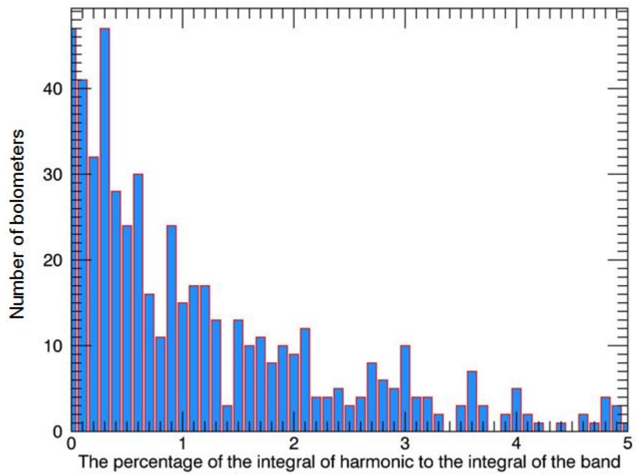

Figure 3.9: The number of bolometers versus the percentage of the integrals of the area of the harmonic to that of the band, for temperature 34 °C.

linearity features was introduced, where the power in the harmonic is compared with that of a nearby region that is representative of the noise, such that a non-linear bolometer would have more power in the harmonic band, while for a linear bolometer both regions would be roughly the same.

Implementing this method, the root mean square of the harmonic was compared to that of the region from 16 cm^{-1} to 19 cm^{-1}. Figures 3.10, 3.11 and 3.12 are histograms, one for each temperature of the three (16.8 °C, 25.3 °C and 34 °C), showing the number of bolometers versus the ratio between the root mean square of each band. For a bolometer operating in the linear regime, the ratio should be close to unity.

From Figures 3.10, 3.11 and 3.12, it can be seen that the majority of bolometers do not exhibit non-linearity features especially in the observations of the black bodies with the two lowest temperatures. Nonetheless, for the observation where the black body had the highest temperature (Figure 3.12), it can be seen that the black body is starting to drive more bolometers non-linear, which is to be expected due to the higher incident power. An unexpected outcome of these measurements, was that the observations of the lowest temperature black body were slightly worse than the second observation having the mid-

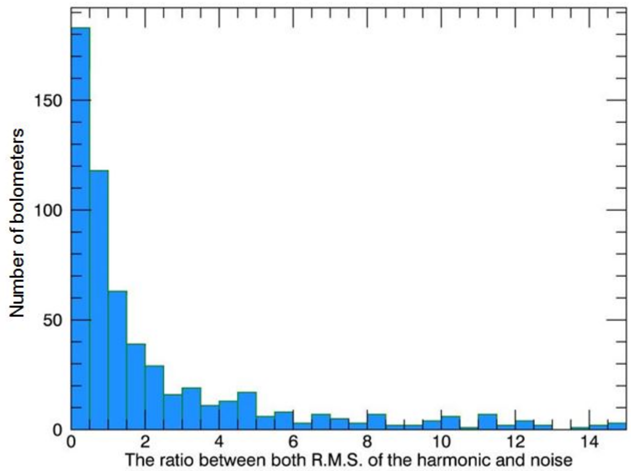

Figure 3.10: A histogram showing the ratio between the root mean square of the harmonic to that of the noise versus the frequency of bolometers for port (C) in the 850 µm band for temperature 16.8 °C.

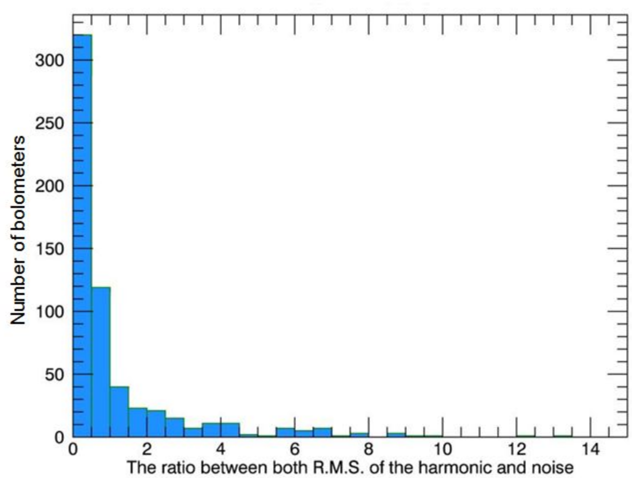

Figure 3.11: A histogram showing the ratio between the root mean square of the harmonic to that of the noise versus the frequency of bolometers for port (C) in the 850 µm band for temperature 25.3 °C.

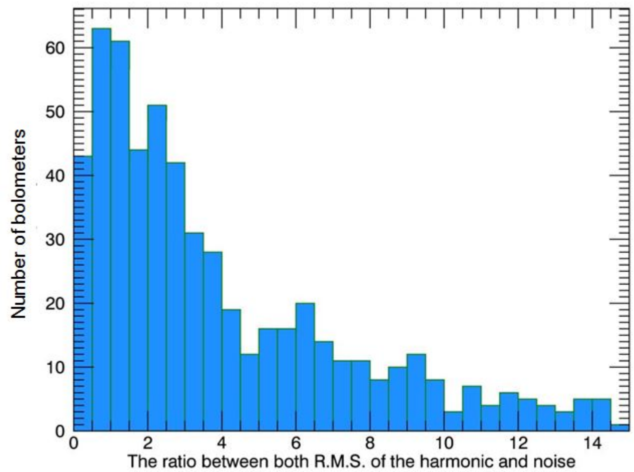

Figure 3.12: A histogram showing the ratio between the root mean square of the harmonic to that of the noise versus the frequency of bolometers for port (C) in the 850 µm band for temperature 34 °C.

range temperature.

3.3.4 The signal-to-noise ratio

Although the change in the bias settings of the bolometers eliminated most of the flux jumps, it was important to compare the signal-to-noise ratio in both cases, because we wanted to know whether by re-biasing and thus changing the responsivity, the signal-to-noise ratio would decrease significantly, in other words to quantify the sensitivity loss occurred. The signal was defined to be the maximum within the band, and the noise to be the root mean square outside the band, in order to enable for the comparison of the signal-to-noise ratios of the bolometers in both cases of bias settings. Figures 3.13 and 3.14, show histograms of the signal-to-noise ratio for the old and the new bias settings respectively, for the 850 µm band port C.

It can be seen in Figure 3.13 and 3.14, in which although the bolometers in the new bias setting have slightly less responsivity, the signal-to-noise ratio is higher when using the new bias. This is because with the old settings more bolometers were experiencing flux jumps in the ZPD region that could not be corrected, thus exhibiting non-linearity characteristics,

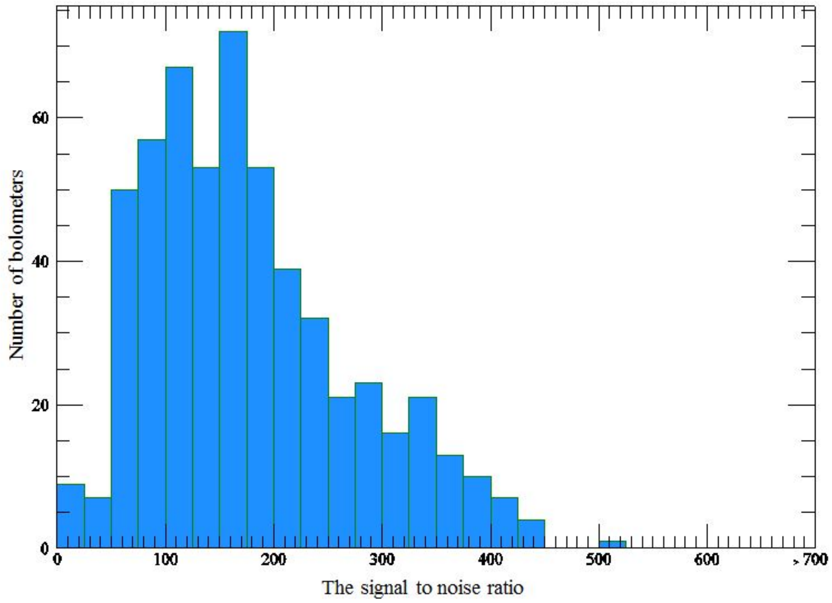

Figure 3.13: A histogram showing the frequency of pixels versus the signal-to-noise ratio, for the data with the old settings, port (C) the 850 μm band.

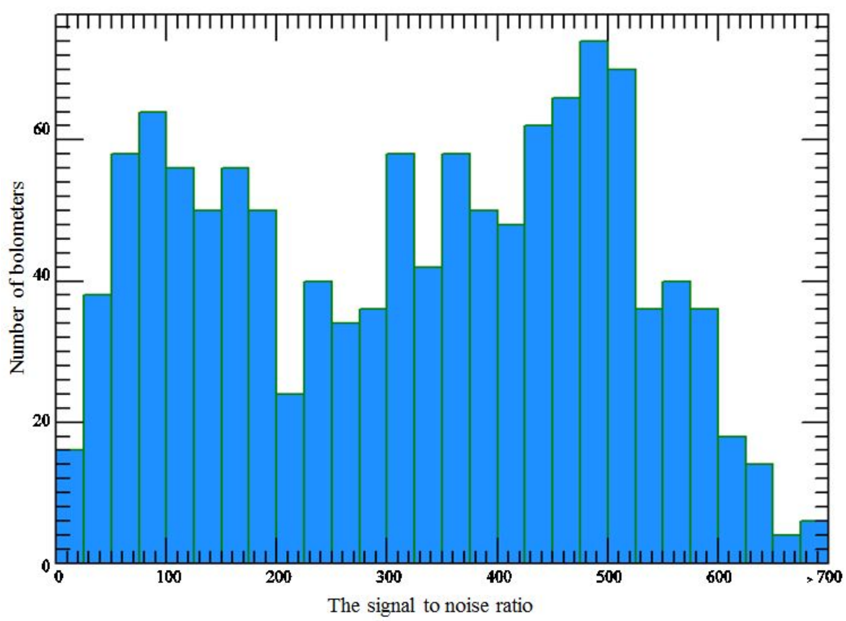

Figure 3.14: A histogram showing the frequency of pixels versus the signal-to-noise ratio, for the data with the new settings, port (C) the 850 μm band.

decreasing the energy within the band in favour of the harmonic bands making the signal average across scans lower, which in turn leads to lower signal-to-noise ratio.

3.4 Determining the spectral response function

3.4.1 Procedure

For the reasons described above, a procedure was developed to obtain the spectral response function using the second set of observations, which consisted of ten interferograms recorded for each of the three temperatures, as shown in Table 3.4. this procedure is as follows:

- Obtain the phase corrected interferogram of each scan. Figure 3.15 shows the signal near the zero path difference region for a well behaved bolometer (19,17) where the signal-to-noise ratio is high.

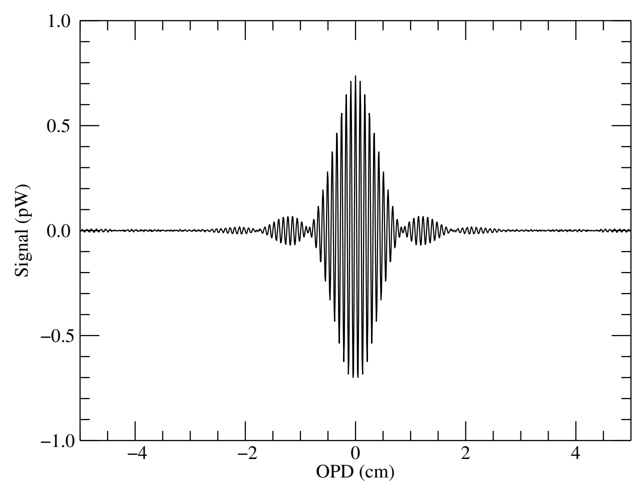

Figure 3.15: A phase corrected interferogram of the 850 μm band port (C) bolometer (19, 17) near the ZPD region.

- Filter the bad interferograms by applying a filter that excludes the bolometers with a signal (maximum of the interferogram) to noise (standard deviation between 9 cm and 10 cm on each side) ratio less than the threshold, which is 30. Figure 3.16 shows an example of a bad interferogram in terms of signal-to-noise ratio.

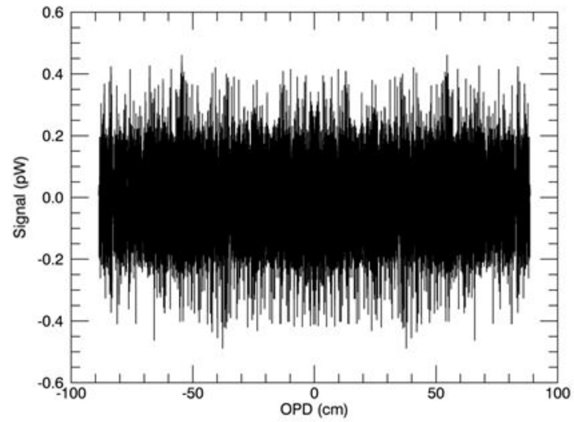

Figure 3.16: An example of a bad interferogram that did not pass the signal-to-noise condition, 850 μm band port (C) bolometer (18, 18).

- Fourier transform each interferogram to obtain the spectrum of each scan, and then average the spectra for each observation across the scans for each bolometer.
- Calculate the Planck functions for the corresponding temperatures.
- The spectral response function is determined by dividing the differences between the spectra (shown in Figure 3.17) over that of the corresponding Planck functions (shown in Figure 3.18), as explained in Equation 3.6. Figure 3.19 shows the spectral response function for bolometer (19, 22).

In the case where there have been several scans of each black body, it is possible to perform the procedure described above, and then filter the spectral response function according to the signal-to-noise ratio (mean of the spectral filter profile within the band divided by the standard deviation within the band). Finally, normalize the mean spectral response function of each bolometer, by dividing the mean over the maximum.

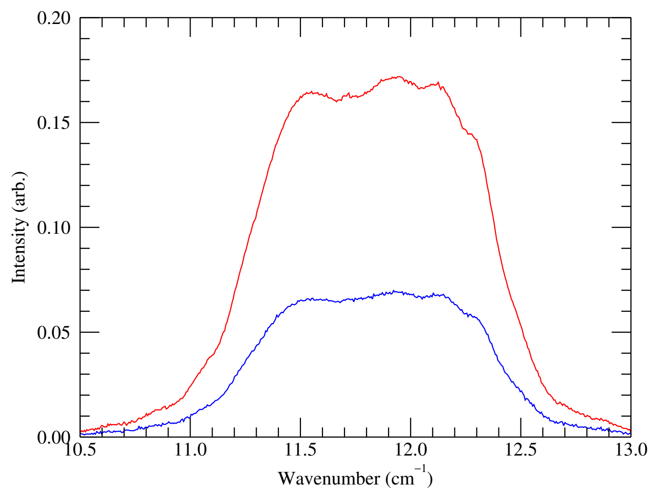

Figure 3.17: The mean spectrum across different scans for bolometer (19, 22) in the 850 μm band port (C) for temperature 34 °C (red), and the mean spectrum across scans for the same bolometer for temperature 16.8 °C (blue).

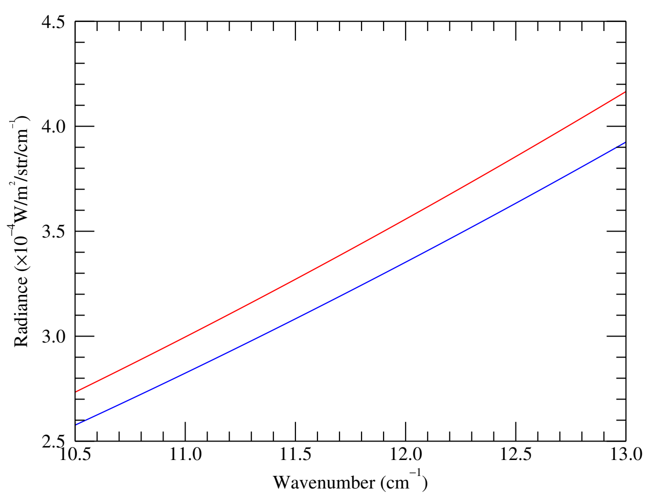

Figure 3.18: The Planck functions for the corresponding temperatures, 34 °C (red) and 16.8 °C (blue).

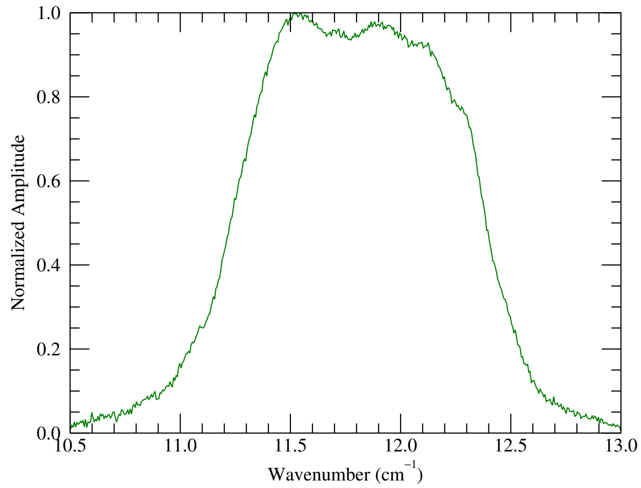

Figure 3.19: The spectral response function of bolometer (19, 22) in the 850 µm band port (C).

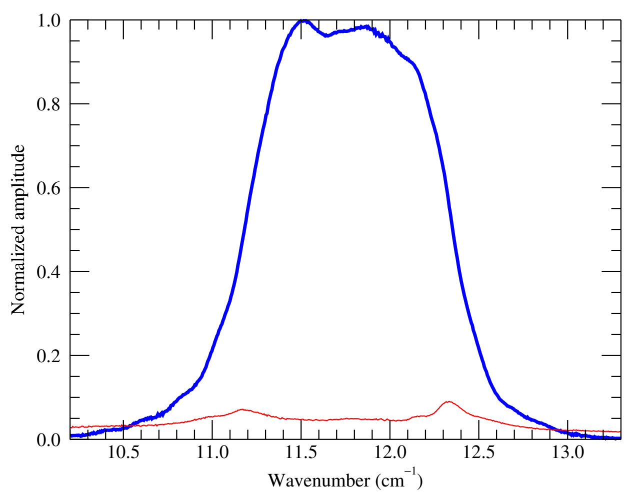

Figure 3.20: The normalized average spectral response function across the sub array (C) in the 850 µm band (blue), and the standard deviation (red).

The average of spectral response function across the sub-array, for all bolometers that passed the test is shown in Figure 3.20.

3.4.2 Spectral Response Stability

Having developed an algorithm to determine the spectral response function, the next step was to see whether it varies across the sub-array in any of the four sub-arrays. Unlike the spectral intensity, which is stronger at the center of the field of view and falls off to the edges of the sub-array, the spectral response function is expected to be smooth and gradual across the sub-array. In order to investigate whether a gradient was present across the sub-array, five regions were defined in each sub-array, one at the centre and one at each corner. The spectral response function for each bolometer was obtained using the same procedure for the other three sub-arrays in both bands (s4a, s4b and s8c). After rejecting the bolometer exhibiting no-linearity, flux jumps or high noise, the total number of bolometers included in the average for each region in each sub-array, is given in Table 3.6.

Table 3.6: A statistical comparison between the first and second sets, where scans with no data are those filled with (NaN; not a number), the bad scans are those with signal-to-noise ratio less than the threshold (30).

Region	**4A**	**4B**	**8C**	**8D**
Total bolometers	589	477	570	503
North-east	19	2	20	8
South-east	20	22	22	15
Northwest	11	22	29	0
South-west	26	27	30	38
Centre	39	21	38	24

Figure 3.21 shows the averages of each region in each sub-array, in which some residual fringing can be seen. This is not regarded to be a significant concern for the photometric observations made by SCUBA-2 (Holland et al., 2006).

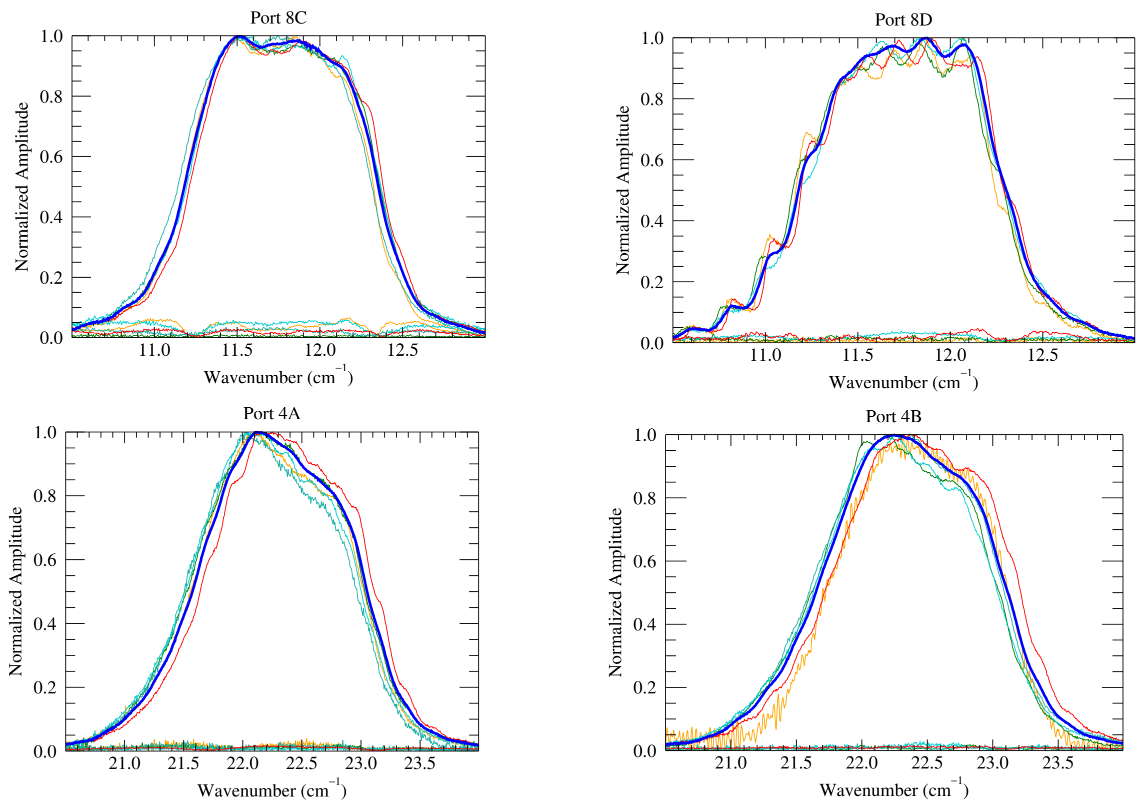

Figure 3.21: The average spectral response function for the four SCUBA-2 sub-arrays used by FTS-2 (thick blue line). Also shown are the SRF as determined from averages of the sub-regions of each sub-array (thin lines).

3.4.3 Comparison of the measured SRF with the theoretical predictions

After obtaining the spectral response function, it was important to compare the measured values with the spectral response function predicted by the linear product of the spectral transmission of each filter shown in Figure 3.2. Figures 3.22 and 3.23 show the comparisons between the predicted and the averaged measured spectral response functions, for each of the two bands 450 µm and 850 µm, respectively.

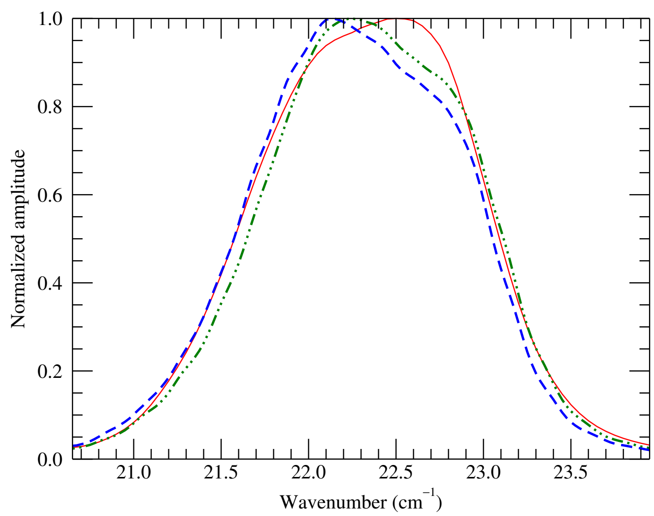

Figure 3.22: Comparison between the predicted (solid red) and the measured (dash-dot green: *s*4*b*, dashed blue: *s*4*a*) 450 µm spectral response functions.

It can be seen in Figure 3.23, that there is a small shift between the predicted and the measured spectral response function. It was speculated that the shift might be explained by the fact the predicted spectral response function is calculated by a linear product of the transmission measurements of each filter, which were performed at room temperature, not at cryogenic temperatures. An optimization function was used to find the factor, which when multiplied by the wavenumber grid, gives the minimum difference between the predicted and the measured and spectral response functions. It was found that the factor for the 450 µm is 1.001, while for the 850 µm it is 1.01. Considering that SCUBA-2 has several filters, which have been measured individually at room temperature, while the mea-

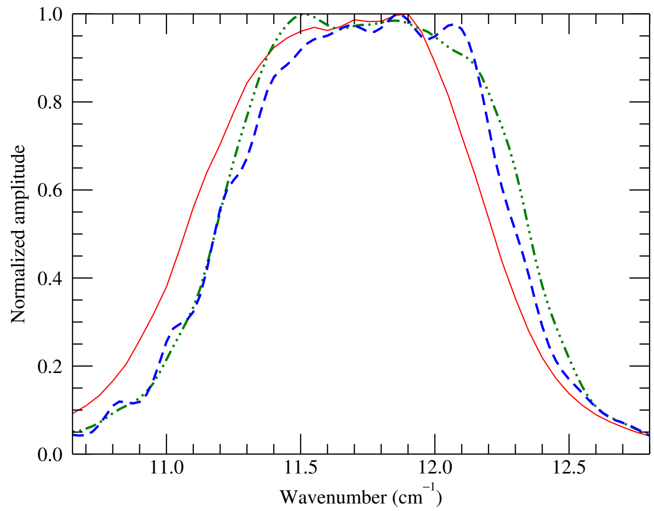

Figure 3.23: Comparison between the predicted (solid red) and the measured (dash-dot green: *s*8*c*, dashed blue: *s*8*d*) 850 µm spectral response functions.

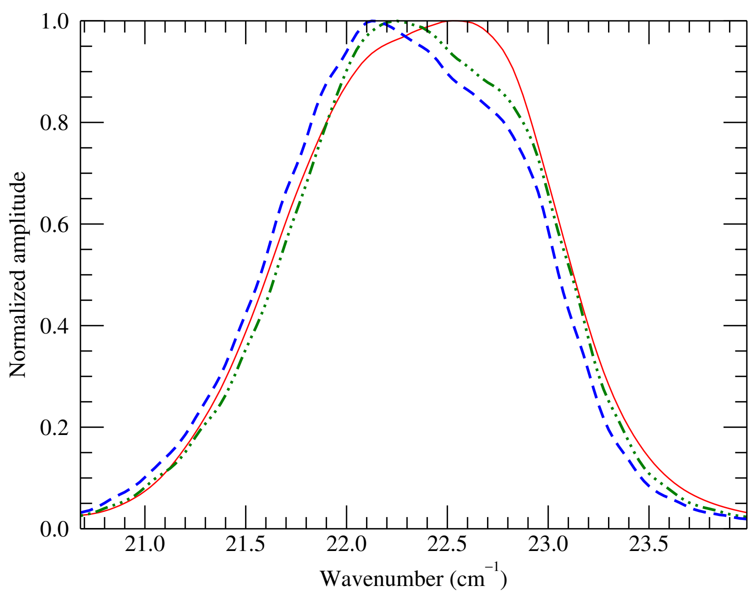

Figure 3.24: Comparison between the predicted (solid red) with a shift factor of (1.00147), and the measured (dash-dot green: *s*4*b*, dashed blue: *s*4*a*) 450 µm spectral response functions.

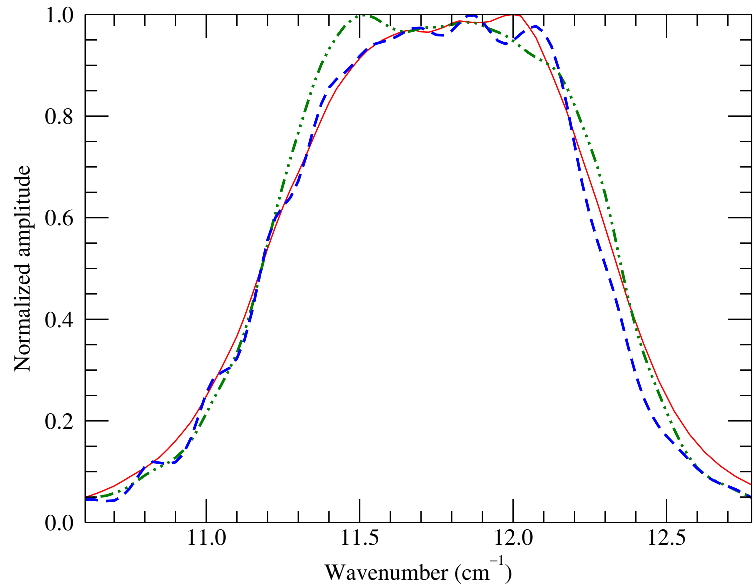

Figure 3.25: Comparison between the predicted (solid red) with a shift factor of (1.01006), and the measured (dash-dot green: $s8c$, dashed blue: $s8d$) 850 μm spectral response functions.

sured combined cryogenic performance is within 0.1 % and 1 % for the 450 μm and 850 μm bands, respectively, showing an excellent agreement between the expected and the measured. Figures 3.24 and 3.25 show the comparison between the expected and the measured spectral response functions with the expected one shifted for the 450 μm and 850 μm bands, respectively.

3.5 Application of the spectral response function

To illustrate how the measured spectral response function can be used, it was applied to the third temperature measurement, considered as an unknown. Since the 450 μm and 850 μm bands are in the Rayleigh-Jeans regime for the temperatures that we have been studying, and as long as the responsivity of bolometers is linear. The unknown black body temperature can be retrieved by using SRF obtained as

$$SRF'(\sigma) = \frac{O_2(\sigma) - O_1(\sigma)}{\sigma^2 (T_2 - T_1)}, \tag{3.7}$$

where SRF'(σ) is the spectral response function of wavenumber and contains the efficiency and the product of the illuminated solid angle (all assumed to be constant because of dealing with the same port, and independent of wavenumber), $O_2(\sigma)$ and $O_1(\sigma)$ are the observations of the two blackbodies with temperatures T_2 and T_1 respectively. Assuming the second input port is at the same temperature in both observations, the temperature of the black body temperature, considered an unknown, can be determined by;

$$T_3 = \frac{O_3(\sigma) - O_1(\sigma)}{\sigma^2 \times SRF'(\sigma)} + T_1 \qquad \text{(K)} \tag{3.8}$$

Figure 3.26 shows the retrieval of the third temperature after applying Equations 3.7 and 3.8. It is again clear that, using the spectral response function derived from the same bolometer produces the temperature with lowest difference between the measured and expected, as compared with using the averaged spectral response functions over a number of bolometers. It also indicates that the responsivity of the bolometer is linear and the retrieved temperature is very close (within ± 0.08 K) to the expected temperature, especially taking into account, the uncertainty of the thermometry and the fact that the ambient temperature of the second input port varied during the observations (as shown Table 3.4).

Also to find how close the result would be to the Planck function. Figure 3.27 shows that using the spectral response function derived from the same bolometer gives the best agreement with the Planck function of the black body, as is to be expected.

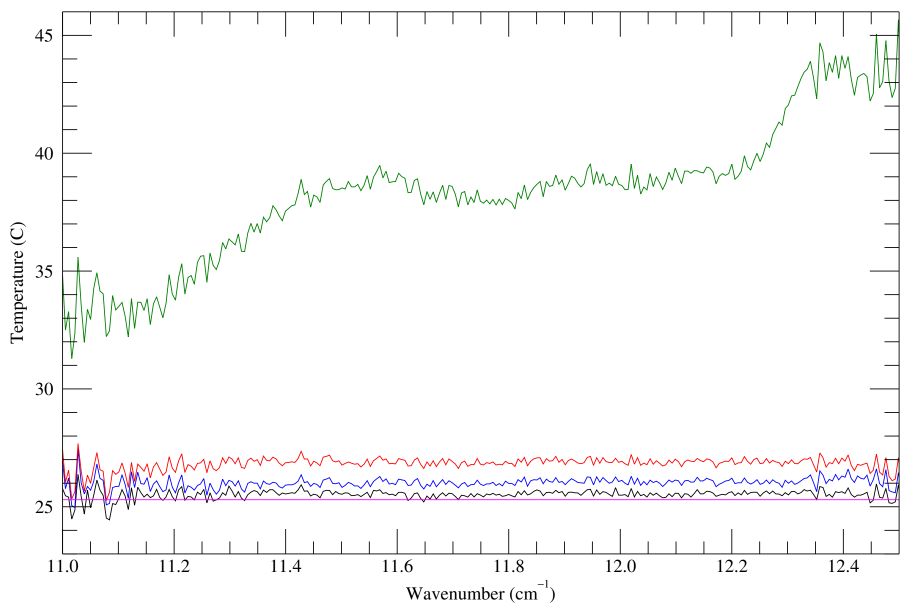

Figure 3.26: Retrieval of the black-body temperature for bolometer (19,22) when using the SRF derived from the same bolometer (lower spectrum), the average of 2×2 neighbouring bolometers (second lowest spectrum), the average of 3×3 neighbouring bolometers (third lowest spectrum) and the average of all the active bolometers (top spectrum). The flat line shows the actual temperature measured on the black-body heater (25.3 °C). Curvature in the retrieved temperature indicates poor characterization of the SRF. It can be clearly seen that the more bolometers included in determining SRF, the increasingly further the retrieved temperature is from the actual one.

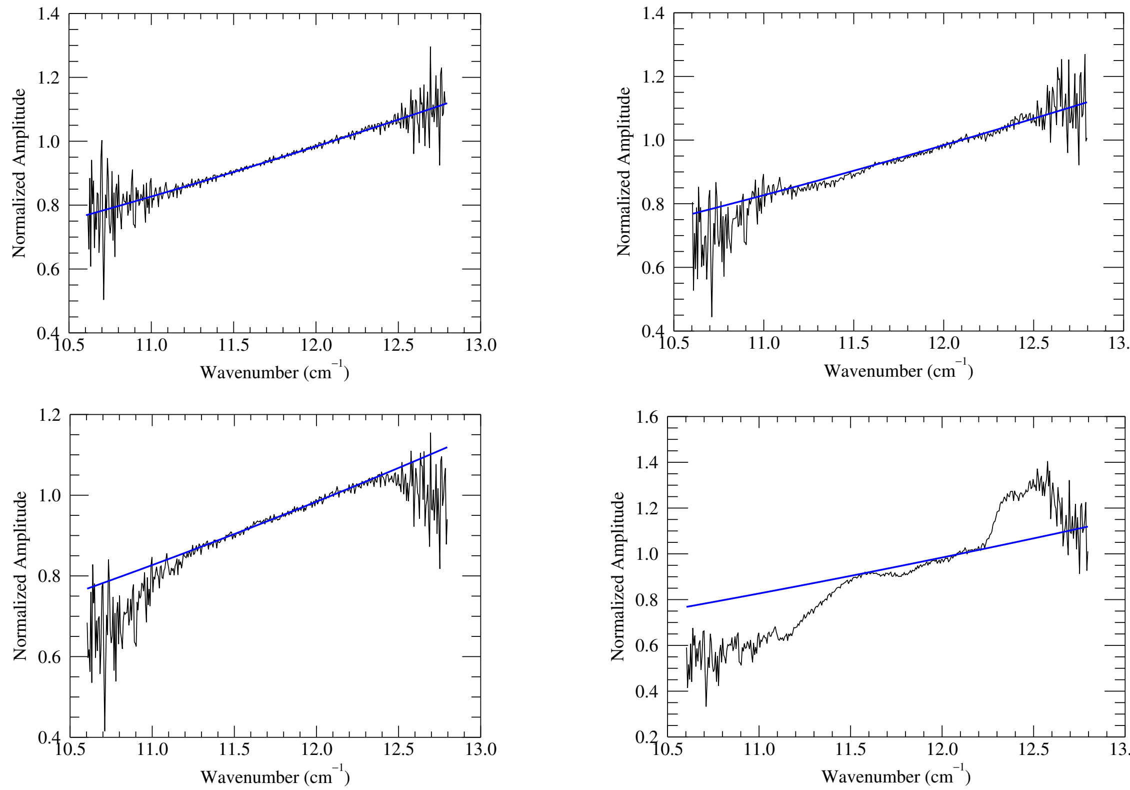

Figure 3.27: A comparison between the application of various spectral response functions on the observations of bolometer (19,22), where the Planck function is shown in blue, and the retrieved is in black, which is the division of the observation spectrum by the SRF. Applying the SRF derived from the same bolometer (top left), the average of 2×2 neighbouring bolometers (top right), the average of 3×3 neighbouring bolometers (bottom left) and the average of all the active bolometers (bottom right). Superimposed is the Planck function of the third temperature (T_{A_3}). It can be clearly seen that, the more bolometers are included in determining SRF, the increasingly poorer the fits are to the Planck function.

3.6 Conclusion

Although the initial bias settings of SCUBA-2 led to a greater number of bolometers experiencing flux jumps, nevertheless it was still possible to deduce the spectral filter profile using a limited subset of the data. Tests were then made to decide which settings were better to be used, according to:

- A statistical comparison of the results.
- The non-linearity characteristics.
- The signal-to-noise ratio.

Based upon the statistical analysis, it was shown that the re-biasing exercise is very beneficial, in terms of the number of bolometers experiencing flux jumps and the signal-to-noise ratio. For this reason the observations, where SCUBA-2 detectors were biased, were used to identify the spectral response profile for each sub array with greater accuracy, and in all subsequent observations with FTS-2 the bolometers were operating in a re-biased mode.

A comparison was made between the calculated spectral response profiles and the room temperature measurements of the individual filters. A small shift was found between the spectral response profiles of the 850 µm band and the prior installation measurements, which might be due to the change in temperature. However taking into account that several filters were combined, there is an excellent agreement between the predicted values and the results. Based upon the fact that the spectral response changes across the array, it preferable to use the spectral response of few bolometers rather than the mean across across the sub-array.

Chapter 4

FTS-2 Observation of Venus

4.1 Introduction

In order to investigate the on sky performance, during the commissioning of FTS-2, several astronomical targets or planetary objects were observed including Venus, Mars, Jupiter and Uranus. After overcoming the data processing challenges as discussed in Chapter 2, and obtaining the integrated spectral response function as presented in Chapter 3, we investigated the spectral information content from Venus. Unfortunately the JCMT was going through a transition phase to a new ownership, thus data access was limited as the observing time was at a premium, and the observation of Venus was performed in poor atmospheric transmission conditions, see Figure 1.3 (C).

As mentioned earlier, SCUBA-2 has 1280 bolometers in each sub-array (see Figures 1.13 and 1.14). However, the diffraction limit of JCMT is about 14$''$ for the 850 µm band, and each bolometer covers around 7$''$, to satisfy the Nyquist sampling criterion. On the day of observation (2013/08/14)(JPL) Venus had an angular diameter of 13.4$''$, making Venus an unresolved object illuminating 2×2 bolometers, as shown in Figure 4.1. This chapter discusses the results of the analysis of the best bolometer and the best scan of Venus.

Table 4.1: The geocentric positions of the Sun and Venus at 2013/08/14, (Ephemeris).

Object	**Right Ascension**	**Declination**
Sun	$9^h\ 35^m\ 03^s$	$14^\circ\ 22'\ 19''$
Venus	$11^h\ 49^m\ 49^s$	$2^\circ\ 01'\ 58''$

Figure 4.2 shows the locations of the inner planets and Earth at 2013/08/14, and Table

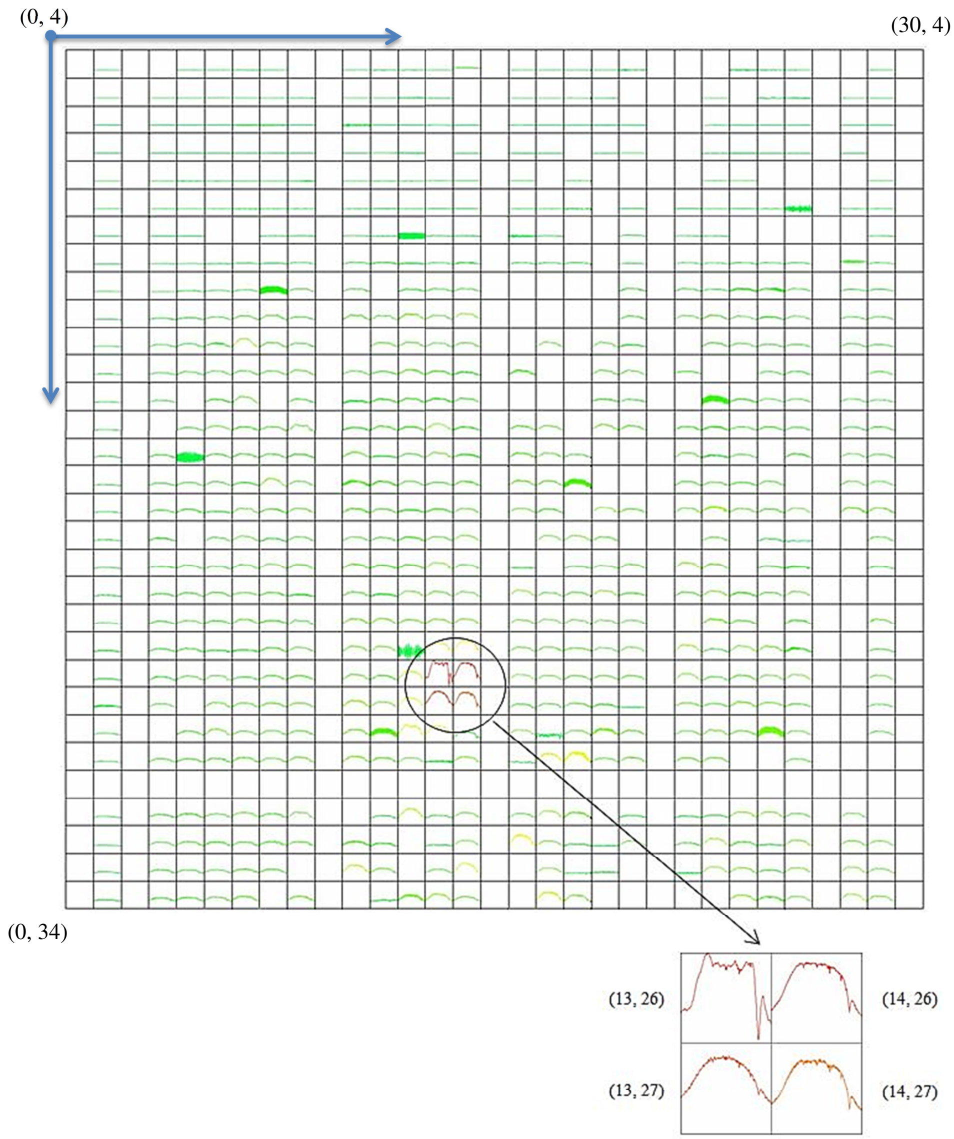

Figure 4.1: A portion of the sub-array of port C in the 850 µm band in observation 20130814 scan 001, in which Venus is illuminating four bolometers. The insert shows a zoom of the four bolometers on Venus, and bolometer (14,26) was chosen because it has high signal.

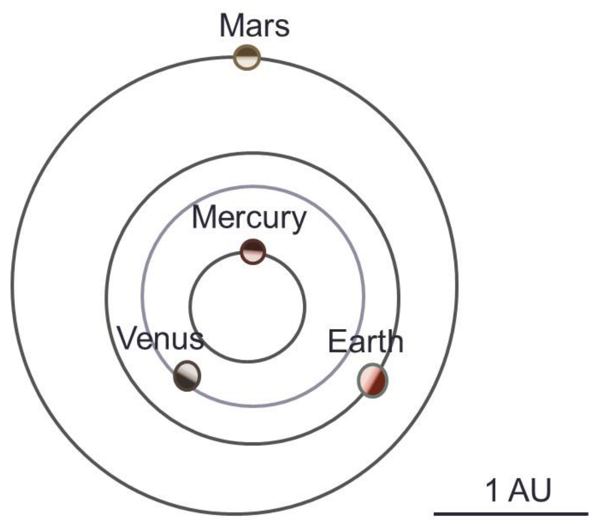

Figure 4.2: A diagram of the positions of the inner planets at the day of observation 2013-08-14, with the sun at the centre (Wolfram—Alpha, 2014).

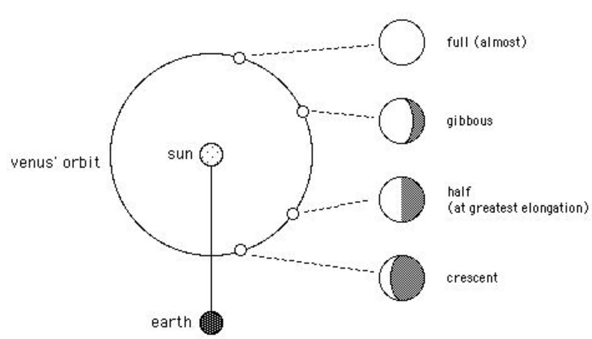

Figure 4.3: A diagram of the phases of Venus in the heliocentric system (Mcclung, 2003).

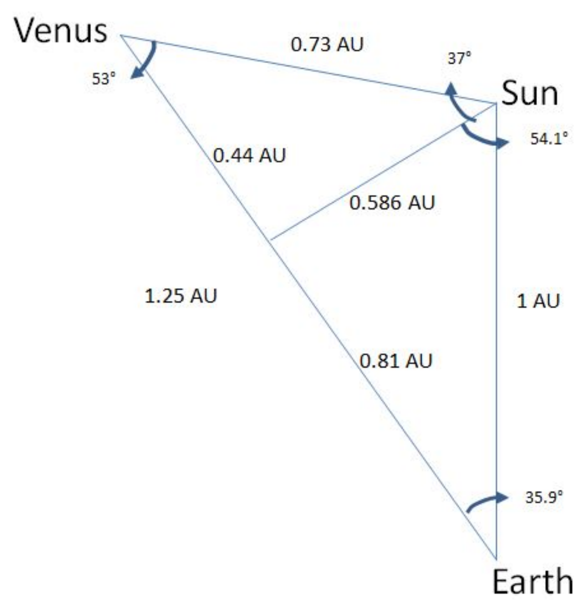

Figure 4.4: The distances and angles between the Sun, Venus and Earth at the time of observation.

4.1 shows the details of the Sun and Venus positions relative to the Earth at the observation date, Figure 4.3 shows the phases of Venus along its orbit. By using the geocentric angles presented in Table 4.1, and assuming that the distance between the Earth and the Sun was 1 AU, it can be calculated that at the time of observation Venus was in the gibbous phase, with about 70 % of its face illuminated by the sun. The atmospheric PWV at the time of observation was 1.82 mm (obtained from the WVM), which makes the atmospheric transmission poor as shown in Figure 4.5.

Nonetheless, the spectral information obtained from this observation can be used to retrieve the temperature of Venus as will be discussed in Section 4.2. It can also be used to identify telluric species (through identifying the absorption lines in the spectrum Section 4.3). Having identified the species of the Earth atmosphere, the spectrum can be then further studied to identify features that are present in the Venusian atmosphere Section 4.4.

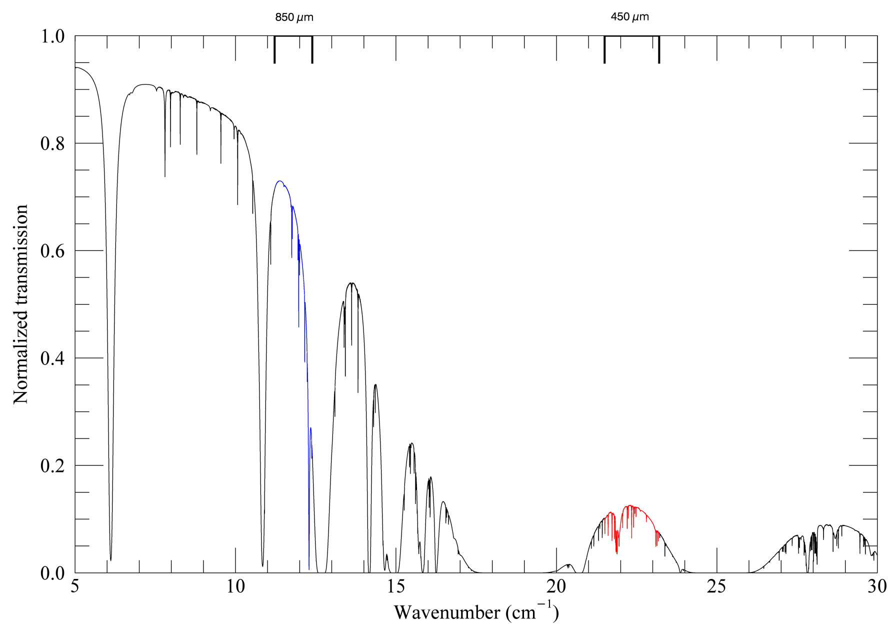

Figure 4.5: The atmospheric transmission at the observation date obtained by BTRAM using the PWV given by the WVM, where the PWV was 1.82 mm. The 850 µm band in blue and the 450 µm band in red

4.2 Venus temperature

Venus is the second planet from the sun with similarities to Earth in size and mass. However, Venus is covered by an optically thick atmosphere such that its surface cannot be seen by observations in the visible band. The thick atmosphere of Venus works like a greenhouse increasing the temperature of Venus surface to about 735 K, while the pressure is 93 bar (Basilevsky & Head, 2003).

This section will present how the temperature can be retrieved. From this information, it is possible to know how deep FTS-2 is observing in the atmosphere, using the relation between the temperature and the altitude in the Venusian atmosphere, Figure 4.6 shows how the temperature pressure profiles change with the altitude. The procedure used in the

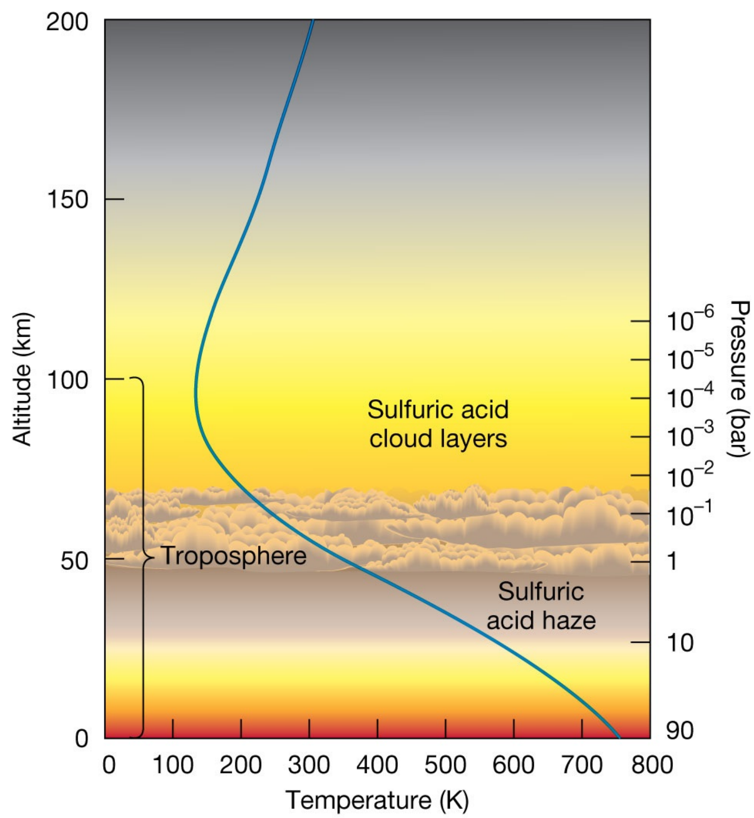

Figure 4.6: The change in temperature and pressure at different altitudes in the atmosphere of Venus (Noel, 2012)

previous chapter to retrieve the temperature of a black body, with a temperature considered to be unknown, will be used here to retrieve the temperature of the observed portion of the Venusian atmosphere at these wavelengths.

The flux density of the astronomical source is attenuated, as some of the light is removed from the beam by scattering or absorption during its path through the Earth's atmosphere. The magnitude of attenuation is related to the opacity of the atmosphere, τ, along the line of sight. The spectral power originally coming from the source, $O_v(\sigma)$, can be related to that observed, $O_{obs}(\sigma)$, by the equation;

$$O_v(\sigma) = \frac{O_{obs}(\sigma)}{\exp[-\tau]} \qquad (\mathrm{W}\ (\mathrm{cm}^{-1})^{-1}) \qquad (4.1)$$

The transmission in the 850 µm band through the Earth atmosphere is dominated by the atmospheric water vapour, as mentioned in Section 1.1. The value of tau is determined through three ways for the JCMT data; First the JCMT-Skydips, which are available as JCMT data files. Second there is the JCMT WVM, which measures Tau every 6 s and is pointed along the main beam. Third there is the calculating sky opacities Tau monitor, which measures the 225 GHz opacity every 10 min. Because the WVM is pointed along the line of sight, it the one that will be used.

Using the spectral response function obtained by Equation (3.8), which is shown in Figure 4.7, the temperature of Venus can be calculated using

$$T_V = \frac{O_V(\sigma)}{\sigma^2 \times SRF'(\sigma)} \qquad (\mathrm{K}) \qquad (4.2)$$

where $O_V(\sigma)$ is the observation of Venus, which is shown in Figure 4.8.

Figure 4.9 shows the retrieved temperature to be 275.3 K with an uncertainty of ±0.5K, which is the mean temperature within the band. From Figure 4.6, it can be predicted that FTS-2 is observing to a depth of around 65 km altitude. It should be noted here that the observation of Venus used was taken with the old bias settings of bolometers (discussed in the previous chapter), so we had constraints on the number of scans that can be used, and

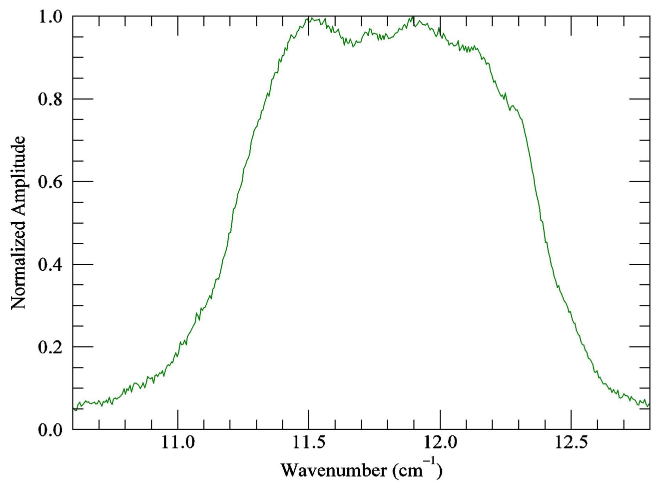

Figure 4.7: The normalized spectral response function of bolometer (14, 26) port C in the 850 μm band.

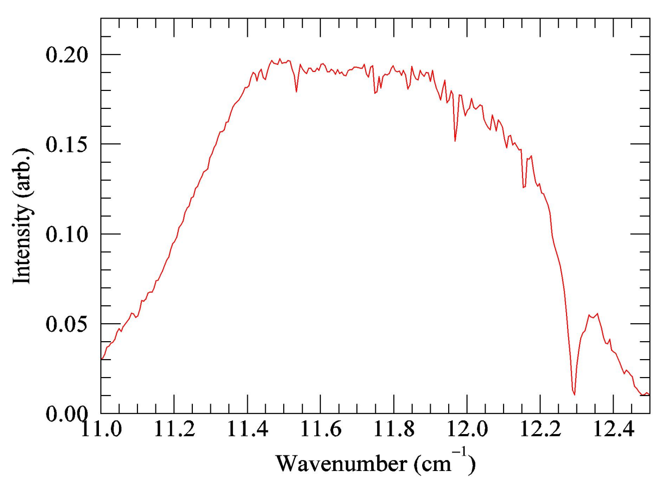

Figure 4.8: The spectrum of Venus obtained from bolometer (14, 26) port C in the 850 μm band, where the slight imbalance between the ports is the reason that the molecular oxygen absorption line (at 12.29 cm^{-1}), which is known to be a saturated line, does not reach zero.

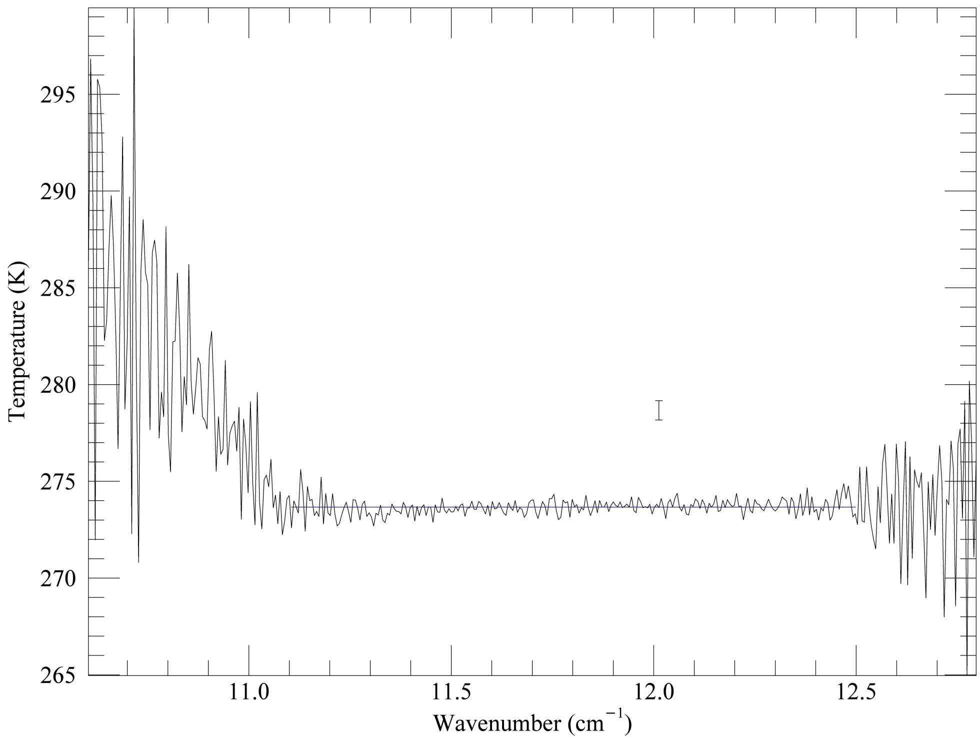

Figure 4.9: Retrieval of Venus temperature for bolometer (14, 26), when using atmospheric transmission and the SRF derived from the same bolometer, as showed in Equations 4.1 and 4.2 yielding a value of mean temperature (blue) 275.26 K with an uncertainty of ±0.5K, which by looking at Figure 4.6 this indicates that FTS-2 probes a height in the Venusian atmosphere of about 65 km. Since the layers above this height are colder, so the species in higher altitudes will be seen through their absorption lines.

only one bolometer could be used. For that reason we chose the best bolometer and the best scan we could find. In order to validate this result, we contacted Dr. Mark Gurwell in the Harvard-Smithsonian Center for Astrophysics, who has an entire model of the temperature profile in Venus, which is used in the Common Astronomy Software Applications (CASA), the value of temperature of Venus at the 850 μm band is 276.7 ± 0.75 K, which is in a very good agreement with our result.

4.3 Using Venus to probe the atmosphere of Earth

The last section showed how the spectrum of Venus was obtained using FTS-2, and how it can be used to retrieve the temperature of Venus, by using the continuum of the spectrum after dividing it by the spectral instrument response. This section will discuss how a spectrum of Venus obtained from the interferogram of one bolometer in one scan can be used to calculate the column abundance of the ozone and the molecular oxygen in the atmosphere of Earth above Mauna Kea. Having identified species known to exist in the atmosphere of Earth, attention can focus on what is left and the possibility can also be used to determine the column abundance of some species in planetary atmosphere, as the determining of column abundance of CO in the Venusian atmosphere, as shown later on.

4.3.1 Absorption Lines

The Venusian spectrum has been analysed to determine what features arise from Venus, and what are due to the Earth. The electromagnetic radiation eminent from Venus is composed of a continuum and of a few spectral lines. The continuum is produced from the optically thick layers in the atmosphere of Venus, from which the temperature of these layers was retrieved as shown in Section 4.2. On the other hand the spectral lines are absorption lines, produced by gas at the higher altitude layers in the Venusian atmosphere, which are optically thin and colder.

When electromagnetic radiation propagates through a medium, the molecules in the medium scatter, absorb, and emit electromagnetic radiation. Scattering strongly depends on radiation wavelength, such that it decreases with increasing wavelength, and since this thesis is concerned with 450 µm and 850 µm bands, at these wavelengths scattering is not important and will not be discussed any further. A spectral line is an electromagnetic radiation with a definite frequency. It can be a bright line which is called an emission line, or it can be a dark line on the continuous spectrum that is called an absorption line. Emission lines appear when the configuration energy of a molecule changes from an energy state to a lower one, this difference of energy is radiated away giving an electromagnetic radiation with a definite frequency. Absorption lines appear when an absorbing material is placed between the source and the observer, Figure 4.10.

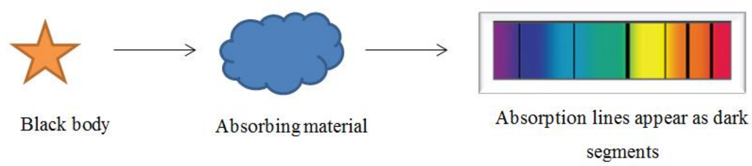

Figure 4.10: An illustration of the process leading to the presence of absorption lines

A molecule, in the absorbing material, absorbs a photon from electromagnetic radiation coming from the source. After absorbing the photon, the molecule is excited from one energy level to a higher one, where the transition energy is equal to that of the photon, see Figure 4.11 for an illustration of the process of molecular excitation. In our case the absorbing material lies in the atmospheres of the Earth and Venus.

Since the excitation energy between the energy levels is different for each molecule, each one has unique photon energies (thus frequencies) that it can absorb, thus the absorption lines of a molecule are unique and can be used to identify the molecule. That is why studying the absorption lines is important as it enables us to determine the molecules that exist in the absorbing material, in this case the atmospheres of the Earth and Venus.

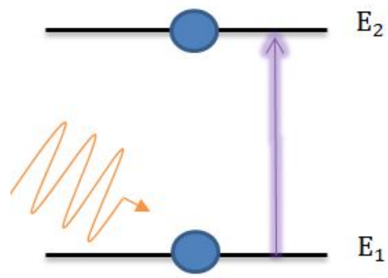

Figure 4.11: A diagram of a photon absorbed by a molecule, the molecule gets excited from energy level E_1 to E_2.

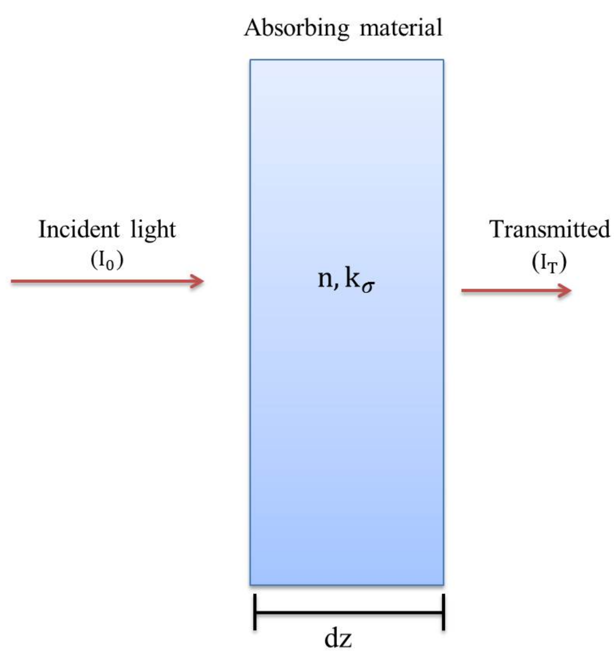

Figure 4.12: A diagram of the absorption of light, when passing through an absorbing material, where, n, is the number density of the absorbing molecule (in molecules cm^{-3}), dz is the thickness of the layer (in cm), both can be related to the column density, u, as $u = ndz$, and k_σ is the absorption coefficient (in cm^2 molecules^{-1})

The absorbed spectral power of the electromagnetic radiation can be calculated as

$$dI = -I_0 k_\sigma u, \qquad (\mathrm{W}\ (\mathrm{cm}^{-1})^{-1}) \quad (4.3)$$

where k_σ is the absorption coefficient, at wavenumber σ, in $\mathrm{cm}^2\mathrm{molecule}^{-1}$, u is the absorber column density in molecules cm^{-2} (Houghton, 2002). In Equation 4.3 the transmission of spectral power depends on k_σ, which is related to the spectral line strength by

$$k_\sigma = S_{T_0,P_0} f(\sigma - \sigma_0), \qquad (\mathrm{cm}^2/\mathrm{molecules}) \quad (4.4)$$

where S is the spectral line strength in $\mathrm{cm}^{-1}\mathrm{molecules}^{-1}$ $(\mathrm{cm}^{-2})^{-1}$ (at temperature $T_0 =$ 296 K and pressure $P_0 = 1013$ mbar) (Houghton, 1986). The spectral line strength is a fundamental property of the absorbing material, and is tabulated in HITRAN (Rothman et al., 2013), Jet Propulsion Laboratory (JPL) (Pickett et al., 1998) and Gestion et Etude des Informations Spectroscopiques Atmosphriques (GEISA) (Jacquinet-Husson et al., 1998) data bases, but it has to be corrected for the temperature of the absorbing material, as will be seen in the next section, $f(\sigma - \sigma_0)$ is the normalized line shape and it is associated with the half width at half maximum, which depends on the temperature and pressure of the material, as the spectral line strength, the HWHM is tabulated in HITRAN and JPL for T_0 and P_0.

From Equations 4.3 and 4.4, the absorption of radiation depends on the spectral line strength, the HWHM, the temperature and pressure of the absorbing material, and the absorber column density. Thus by calculating the absorbed spectral power and the other conditions, we can obtain the column density of the different molecules in the material, as we will discuss in the next section the calculation of the column abundances of ozone and molecular oxygen in the atmosphere of Earth.

4.3.2 Ozone and molecular oxygen column abundance in the atmosphere

In order to measure the column abundance, first we need to calculate the absorbed spectral power in the absorption line, which is obtained by the equivalent width.

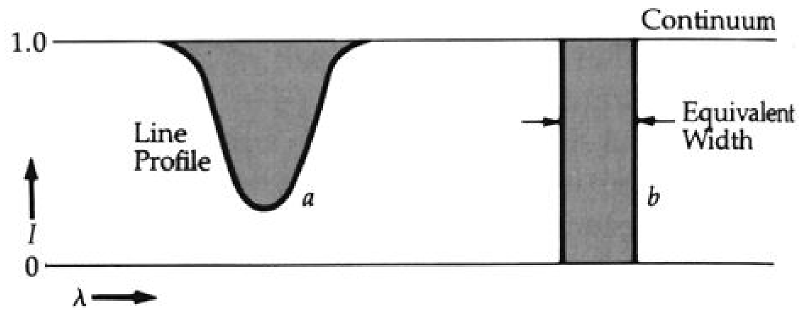

Figure 4.13: A diagram show how the equivalent width is found, where the area of the rectangle is equal to that of the line profile (Rieke, 2002)

The equivalent width of a spectral line is a measure of the strength of a spectral line in the spectrum, found by forming a rectangle with a height equal to the continuum, as shown in Figure 4.13. The equivalent width is the width of the rectangle that gives the area of the rectangle to be equal to that of the spectral line.

Ozone has several absorption lines within the range of the spectrum 11.22 cm^{-1} to 12.395 cm^{-1}. The equivalent width along with the spectral strength and the half width at half maximum of each line, can be used to determine the column abundance of ozone. The ozone absorption lines were chosen for analysis according to their strength. Eleven lines were chosen, whose spectral lines, S_0 (at T_0 and P_0 see Table 4.3) are higher than 3.2×10^{-23} cm molecules^{-1}, because of the low quality of the spectrum, as it is from one bolometer in one scan with a poor atmosphere transmission conditions, as shown in Figure 4.5.

After obtaining the Venus spectrum shown in Figure 4.14, the baseline of the spectrum was brought to zero by subtracting the minimum value of the molecular oxygen absorption line, as it is supposed to be a saturated line.

The equivalent width was calculated using an IDL code written by Brad Gom, and here we will show how to calculate one of the ozone absorption lines (at 12.157 cm^{-1}), as Figure

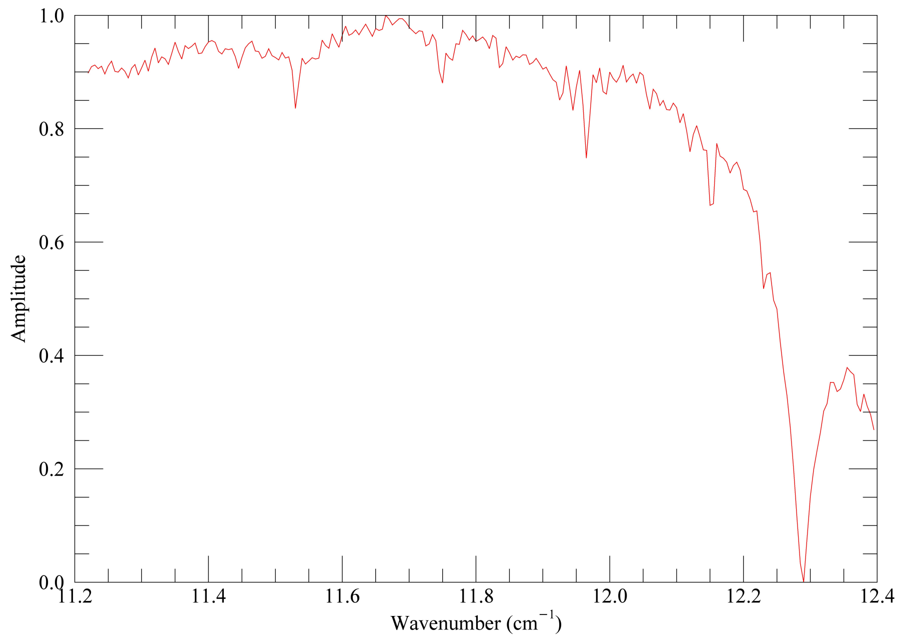

Figure 4.14: The spectrum of Venus obtained from bolometer (14,26) port C in the 850 µm band, the baseline was brought to zero and then the spectrum was normalized.

4.15 shows, the code introduces a fitted polynomial to be regarded as the continuum of the

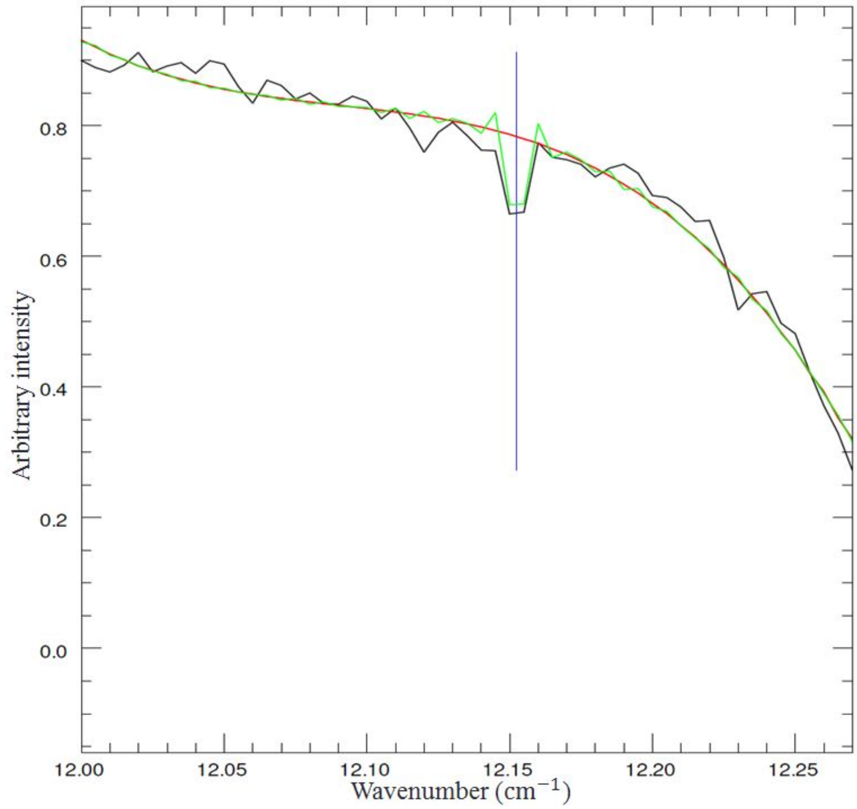

Figure 4.15: Using FTfitter gui, an IDL program written by Brad Gom, to measure the equivalent width of spectral lines, and here we show how it works on the ozone line at 12.157 cm^{-1}, where the blue line denotes the centre of the line, the red line is the continuum, the black is the spectrum, and the green is fitted to the absorption line.

spectrum, then by choosing an absorption line, it calculates the area of the absorption line with respect to the continuum (which is given here as 1.3×10^{-3}), thus the equivalent width is the result of dividing the area by the height of the continuum at the absorption line giving an equivalent width of ($1.6 \pm 0.1 \times 10^{-3}$ cm^{-1}).

The column abundance of ozone (with the assumption it is a weak line) can be calculated as;

$$u = \frac{A_{eq}}{S_{T,P} M_a} \qquad \text{(molecules cm}^{-2}\text{)} \tag{4.5}$$

where u denotes the vertical column abundance, A_{eq} denotes the equivalent width, $S_{T,P}$ denotes the spectral line strength corrected, for the temperature and stimulated emission,

Table 4.2: The m values for some molecular species (Chapman, 2003)

Molecular species	m values
O_3	1.5
O_2	1
CO	1
CO_2	1
H_2O	1.5
N_2O	1
CH_4	1.5

of ozone and M_a denotes the air mass, which is known for the observation. Equation 4.5 shows how the corrected spectral line strength can be calculated (Rothman et al., 2013),

$$S_{T,P} = S_0 \left(\frac{T_0}{T}\right)^m \left(\frac{\sigma}{\sigma_0}\right) \left(\frac{1 - exp[\frac{-hc\sigma}{k_B T}]}{1 - exp[\frac{-hc\sigma_0}{k_B T_0}]}\right) \left(\frac{1 + exp[\frac{-hc\sigma_0}{k_B T_0}]}{1 + exp[\frac{-hc\sigma}{k_B T}]}\right) \left(\frac{exp[\frac{-E}{k_{B1} T}]}{exp[\frac{-E}{k_{B1} T_0}]}\right) \quad \text{(cm/molecules)} \qquad (4.6)$$

where S_0 is the spectral line strength at $T_0 = 296$K and 1013 mbar pressure, T is the assumed temperature, σ and σ_0 are the line wavenumber as observed and the original line wavenumber respectively, h is the Planck constant in $\mathrm{J \cdot s}$, c is the speed of light in $\mathrm{cm \cdot s^{-1}}$, k_B is Boltzmann constant in $\mathrm{J \cdot K^{-1}}$, E is the energy in $\mathrm{cm^{-1}}$ of the lower level of the transition and k_{B1} is Boltzmann constant in $\mathrm{cm^{-1} \cdot K^{-1}}$. The value of m depends on the molecular species, the m values for some molecular species are given in Table 4.2.

The BTRAM, which gave the relation between altitude, pressure and temperature above Mauna Kea, was used to generate a tropical atmospheric transmission model. In this model the ozone temperature was assumed to be $T = 236$ K, according to the temperature of the layer with the highest ozone column abundance (at 30 km altitude). The spectral line strength of the ozone line at 12.157 $\mathrm{cm^{-1}}$ was found to be $S_0 = 1.45 \times 10^{-22}$ cm molecules^{-1} using HITRAN database. Thus using Equation 4.6 the corrected spectral line strength for the (12.157 $\mathrm{cm^{-1}}$) is $S_{T,P} = 2.21 \times 10^{-22}$ cm molecules^{-1}. By working through the above steps for all the eleven chosen ozone lines, it is possible to establish a relation between the equivalent width and the corrected spectral line strength. Table 4.3 shows the

Table 4.3: The values of the properties of the ozone lines, where the spectral line strength, energy of the lower level of transition and HWHM obtained from HITRAN, the equivalent width is calculated using FTfitter, and the spectral line strength corrected for the temperature and pressure of ozone using Equation 4.6 (Rothman et al., 2013).

Wavenumber (cm^{-1})	**Spectral line strength** ($\times 10^{-23}$ cm molecule^{-1})	**Spectral line strength corrected** ($\times 10^{-23}$ cm molecule^{-1})	**Energy of the lower level of transition** (cm^{-1})	**HWHM** ($cm^{-1}atm^{-1}$)	**Equivalent width** ($\times 10^{-4} cm^{-1}$)
11.752	8.3	12.5	77.082	0.076	10.5 ± 0.8
11.769	7.1	8.0	348.645	0.074	2.4 ± 0.8
11.842	3.5	5.7	5.729	0.079	2 ± 0.8
11.929	6.8	9.3	171.502	0.075	3.9 ± 0.8
11.948	7.1	7.5	411.055	0.075	4.2 ± 0.8
11.970	15	22.1	100.572	0.076	15.6 ± 0.8
11.997	8.2	7.8	510.203	0.074	2.2 ± 0.8
12.124	6.0	5.9	464.999	0.074	4.5 ± 1
12.157	14.5	22	64.926	0.078	16.3 ± 1
12.234	9.7	11.4	313.120	0.075	6.17 ± 1
12.376	7.1	9.3	207.562	0.073	9.14 ± 0.8

details of every one of the eleven absorption lines of ozone, and in Figure 4.16 shows the positions of the ozone lines on the spectrum of Venus.

The relation between the equivalent width and the corrected spectral line strength can be established, see Figure 4.17. By dividing the slope over the air mass, which is 1.06, the vertical column abundance of ozone can be given as $u = l/M_a = 7.9\ \pm 0.5\ \times 10^{18}$ cm^{-2}.

In an attempt to validate the result, we contacted Dr. Richard Querel in University of New Zeeland, who has access to the data sets of the OMPS satellite (Flynn et al., 2004), which is the daily ozone column estimate for a 1×1 degree area at latitude 19.5°, longitude $-155.5°$, the value of the ozone column abundance at 2013/08/14 was 7.67×10^{18} cm^{-2}.The determined value using FTS-2 with one bolometer shows excellent agreement

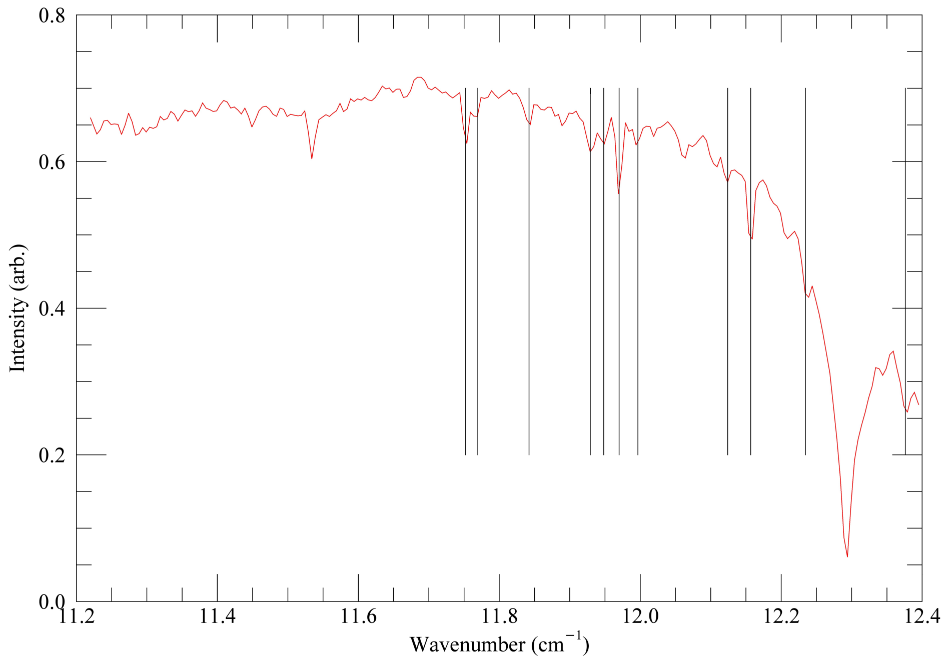

Figure 4.16: The spectrum of Venus from bolometer (14,26). The vertical lines show absorption lines of ozone included in this analysis

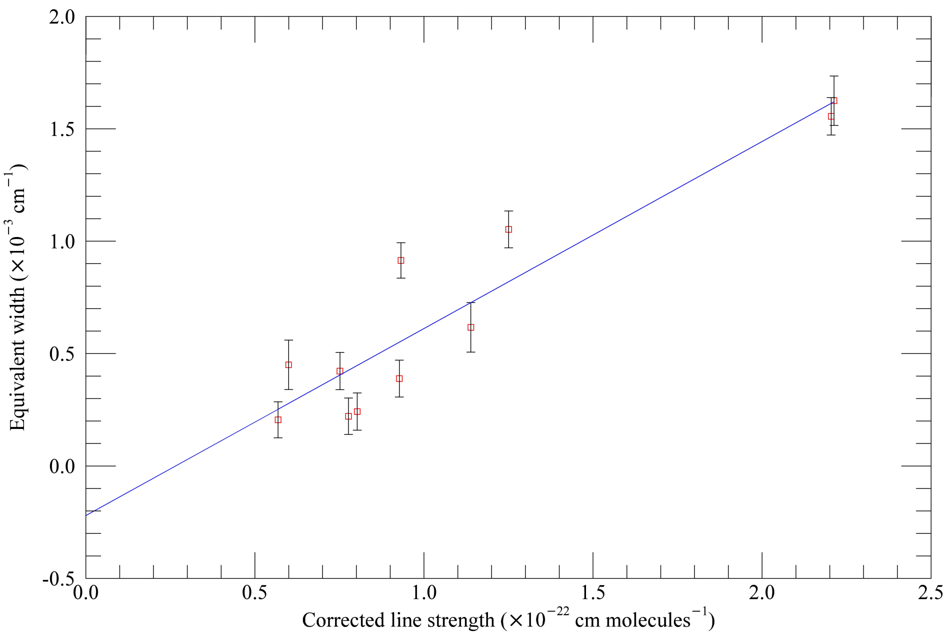

Figure 4.17: The relation between the equivalent width of each of the absorption lines of ozone as calculated using FTfitter gui and the corrected spectral line strength calculated by Equation 4.2 using HITRAN database and BTRAM. A line is fitted to the data points with a slope of $l = 8.3\ \pm 0.5\ \times 10^{18}$ cm^{-2} molecules, and intersects the y axis at $-2.2\ \pm 0.6\ \times 10^{-4}$ cm^{-1}.

with that obtained from OMPS, and this shows the vast improvement in sensitivity of SCUBA-2, since the determination of the column abundance of ozone was previously performed using the observations of the sun.

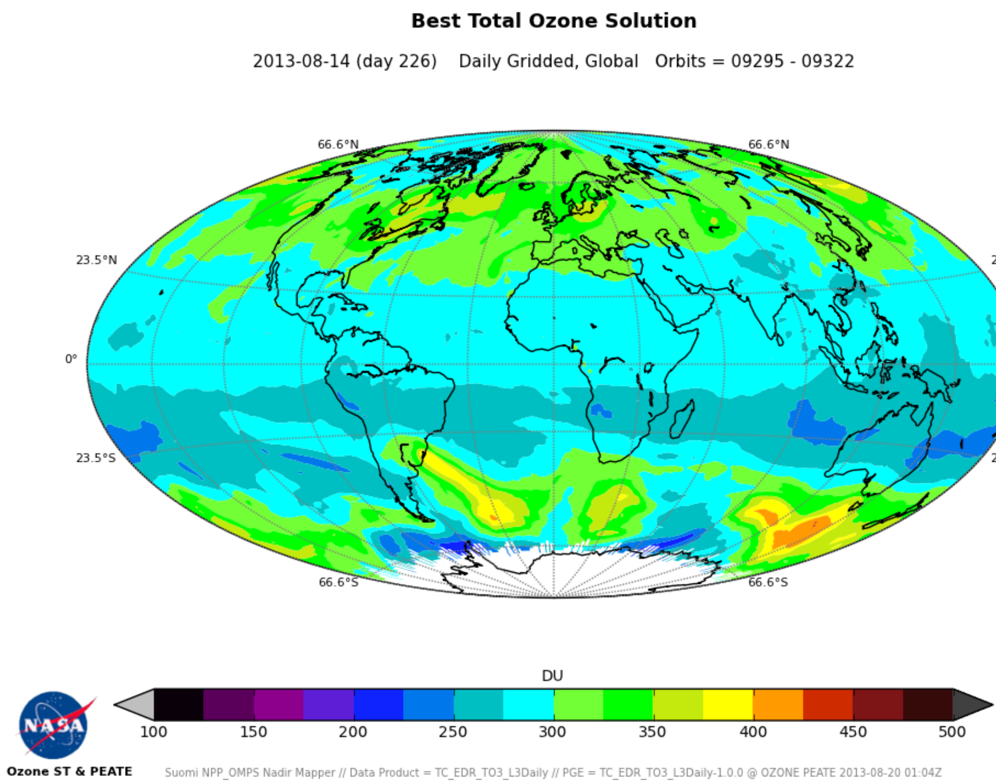

Figure 4.18: The daily ozone column estimate for a 1 x 1 degree area (at Latitude 19.5°, Longitude $-155.5°$. Taken from the OMPS data set.

The same method was used to obtain the vertical column abundance of molecular oxygen in the Earth's atmosphere. Thus using the FTfitter code to obtain the equivalent width of the molecular oxygen absorption line at $12.29\,\mathrm{cm}^{-1}$, the equivalent width was found to be $0.07\,\mathrm{cm}^{-1} \pm 5 \times 10^{-3}\ \mathrm{cm}^{-1}$. From HITRAN database spectral line strength is 2.3×10^{-26} cm molecules^{-1} and the half width at half maximum is 0.047 cm^{-1} atm^{-1} at 296 K and 1 atm pressure, while the energy of lower level of transition is $3.96\,\mathrm{cm}^{-1}$. Using Curtis Godson approximation, in which we take the mean of the pressure of the lower bound and the higher bound to be the assumed pressure, where we assume that molecular oxygen is in a hydrostatic equilibrium (Houghton, 2002). Since the lower pressure bound is zero and the higher bound is (at the telescope, and obtained from the header of the observation) 625 mbar, the pressure is assumed to be 312.5 mbar and using BTRAM, see Figure 4.19, it was found that for tropical regions the temperature is 241 K at pressure 312.5 mbar. Us-

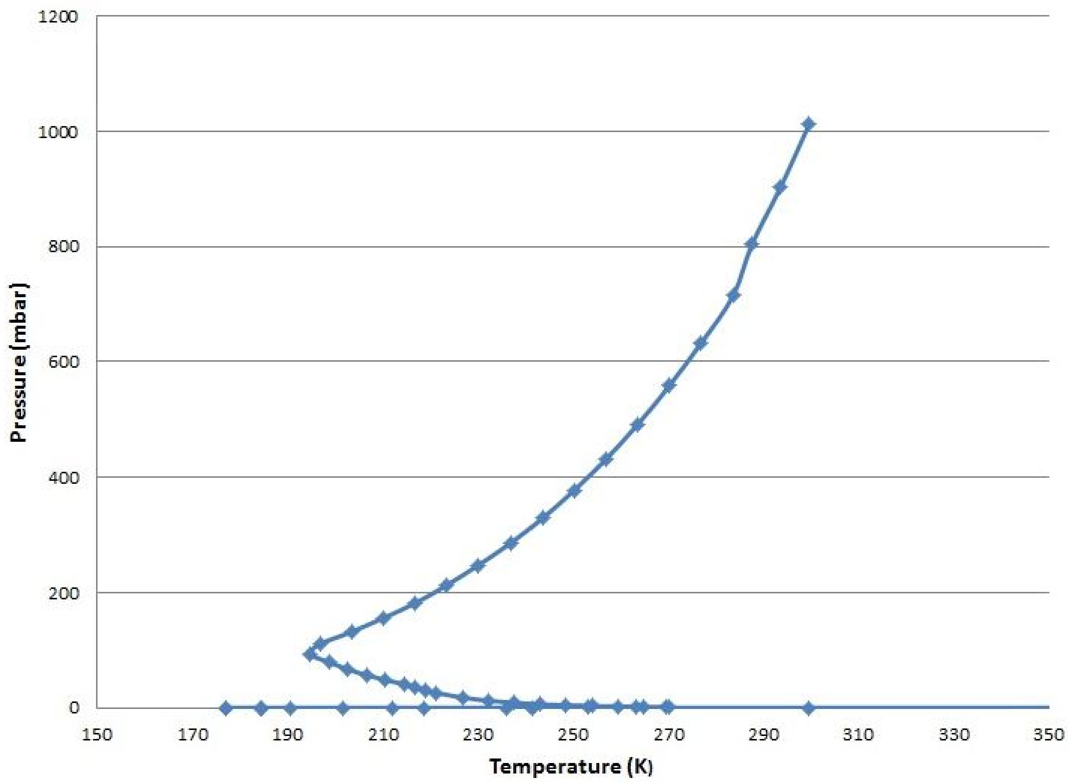

Figure 4.19: The relation between temperature and pressure of the Earth atmosphere in the tropical regions, the data were obtained using BTRAM.

ing Equation 4.6, the corrected spectral line strength is 3.48×10^{-26} cm/molecules. The half width at half maximum can be corrected for the temperature and pressure of molecular oxygen as (Rothman et al., 1998)

$$\alpha = \alpha_{ref} \left(\frac{P}{P_0}\right) \left(\frac{T_0}{T}\right)^m \qquad (\mathrm{cm}^{-1}\ \mathrm{atm}) \qquad (4.7)$$

where α and α_0 are the corrected and the reference half width at half maximum respectively, P and P_0 are the assumed pressure and the reference pressure respectively, while T and T_0 are the assumed temperature and the reference temperature respectively. From Equation 4.7, α, is calculated to be 0.018 cm^{-1} atm. Assuming the molecular oxygen absorption line is a strong line, the column abundance of molecular oxygen along the line of sight can be calculated as:

$$u = \frac{A_{eq}^2}{4S_{T,P}\alpha} \qquad \text{(molecules cm}^{-2}\text{)} \tag{4.8}$$

dividing u by the air mass to determine the vertical column abundance of molecular oxygen, which gives $1.9 \pm 0.2 \times 10^{24}$ molecules cm^{-2}. While the order of magnitude in our result agree with the theoretical column abundance of molecular oxygen, which is 4×10^{24} molecules cm^{-2} (Seinfeld & Pandis, 2012), we believe the discrepancy is due to the fact that the line at 12.29 cm^{-1} is close to the edge of the band, where the transmission of the filter is rapidly dropping (Figure 4.7). Thus the equivalent width calculated for the line should have been larger, which in turn will increase the column abundance by the Equation 4.8.

4.4 Venus absorption lines

4.4.1 Introduction

The atmosphere of Venus is optically thick acting as a greenhouse, there is also a high speed circulation up to about 100 m/s, such that the atmosphere circles the planet in just four Earth days, however, the wind speed decreases in lower altitudes. The atmosphere of Venus can be divided into three sections: lower atmosphere (troposphere), middle atmosphere, upper atmosphere and ionosphere, see Figure 4.20. The atmosphere of Venus is composed mainly of carbon dioxide (96%) and nitrogen (3.5%) (Svedhem et al., 2007). As shown in Section 4.2 the altitude that FTS-2 is predicted to be observing is around 65 km, which is the altitude of the middle and lower atmospheres, so the main cloud layers and the middle atmosphere will be discussed in more details. The main cloud layers extend from altitude slightly less than 50 km to about 70 km, the middle atmosphere is a thin haze extending to about 90 km altitude and it is thicker near the poles. As shown in Figure 4.20, the main cloud region is formed of three layers, where the clouds are composed mainly of sulfuric species (Esposito et al., 1983). Figure 4.21 shows the composition of the principle sulphur-

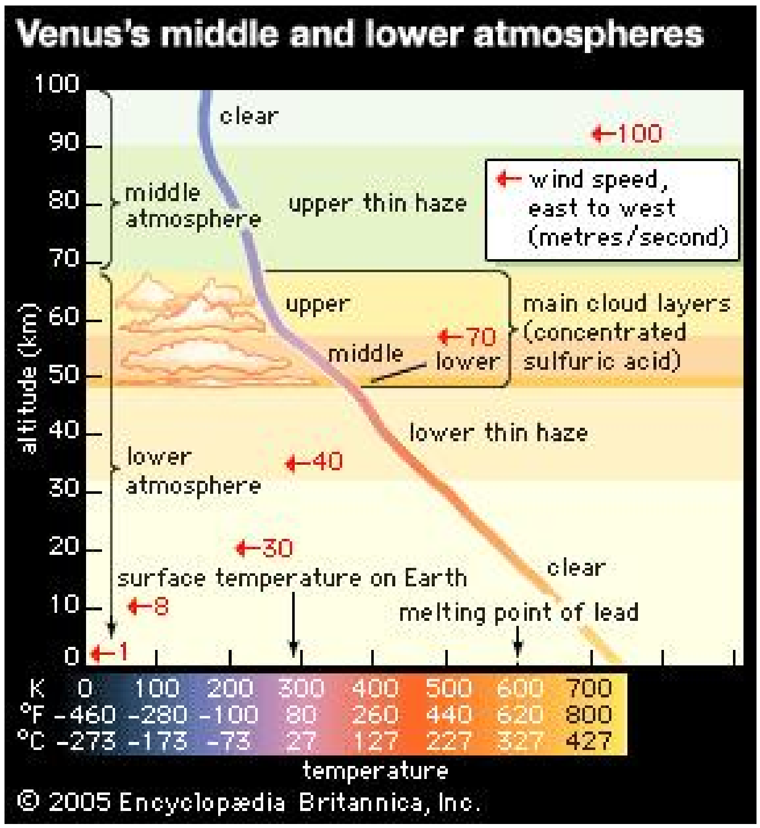

Figure 4.20: The middle and lower atmospheres of Venus.

bearing species.

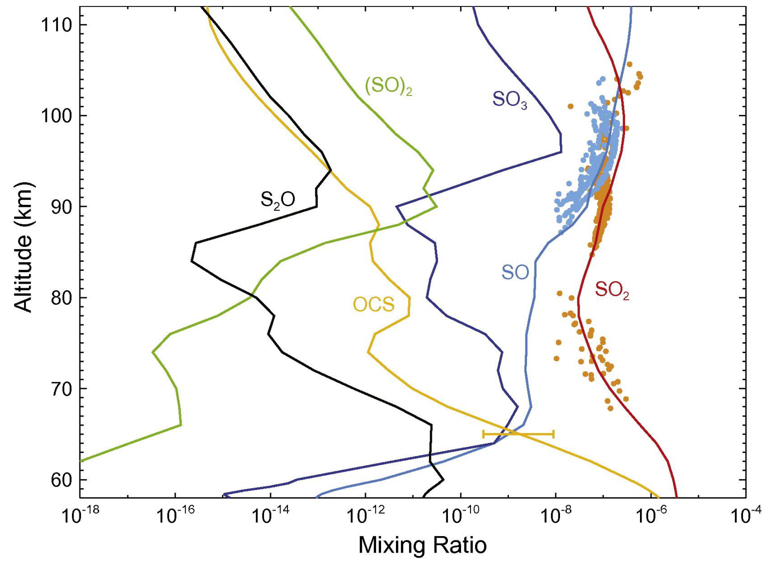

Figure 4.21: The composition of sulfuric species in the atmosphere of Venus (Zhang et al., 2012)

After having identified the species of the Earth atmosphere, the spectrum can be further studied to identify features that must arise in the atmosphere of Venus. In order to identify the molecules in the atmosphere of Venus, the frequencies of the absorption lines should be determined, so any Doppler effects that exist due to the relative motion between Venus and Earth should be addressed. Thus, to examine whether the Doppler shift of Venus is large enough to have to be accounted for, the relative velocity between the Earth and Venus on the time of observation should be calculated, because it is responsible for the Doppler shift. When the bodies are approaching, the Doppler effect shifts the spectral information towards blue (higher frequencies), while if the bodies are moving apart from each other the spectral information is shifted towards red (lower frequencies), the change in the frequency between the observed and the original frequency is given by (Kutner, 2003).

$$\Delta f = \frac{v}{c} f_0 \qquad \text{(Hz)} \qquad (4.9)$$

where Δf is the change in frequency, v denotes the relative velocity, c is the speed of light in the vacuum and f_0 is the original frequency. By using the geocentric positions of the Sun and Venus at the time of observation shown in Table 4.1, and assume the distance between the Earth and Sun is 1 AU. It is possible to calculate the relative velocity of Venus with reference to Earth at the time of observations, see Figure 4.4.

The relative velocity of Venus with reference to Earth is $v = 10.4$ km/s, using Equation 4.9 this relative velocity gives, Δf of 0.012 GHz, that is smaller than the resolution of FTS-2, thus the effect of the Doppler shift can be disregarded.

4.4.2 Absorption features of Venus

Using Venus spectrum, some absorption features were identified other than the telluric absorption lines and then were compared to the molecules shown in Figure 4.21, in order to search for a match. Figure 4.22 shows the details of the identified absorption lines from the spectrum, and the absorption lines of five molecules; HDO, SO_2, CO, SO and S_2O, which are the molecules that are expected to show in the spectrum.

Figure 4.23 shows the ozone and the theoretical locations of the absorption lines of molecules, SO_2, CO, SO, and S_2O, whose lines were found to fall on what are thought to be absorption lines in the spectrum. Although, as seen in Figure 4.23, absorption lines of S_2O match absorption features in the retrieved spectrum of Venus, it is still an open discussion whether these are coming from S_2O existing in the Venusian atmosphere, as the column density of S_2O in Venus is 2×10^{15} cm^{-2} (Mills et al., 2007), or it is coming from the Earth's atmosphere as there is a volcano near Mauna Kea, which might be responsible for the presence of S_2O absorption lines.

After identifying the features from the Earth's atmosphere, attempts were made to identify species that might present in Venus. The next section follows the same methodology to calculate the column abundance of CO from its absorption line at 11.53 cm^{-1}.

Observed			Theoretical	
Line #	Observ. Prop.		Elements	Position (GHz)
Line 1	Center	343.20582	HDO	N/A
	Center Err.	0.03389	SO2	N/A
			CO	N/A
			SO	N/A
			S2O	343.2457
Line 2	Center	345.79822	HDO	N/A
	Center Err.	0.0117	SO2	N/A
			CO	345.79599
			SO	345.70456
			S2O	345.79868
Line 3	Center	356.0993	HDO	N/A
	Center Err.	0.1146	SO2	356.09938
			CO	N/A
			SO	N/A
			S2O	356.0867
Line 4	Center	356.36697	HDO	N/A
	Center Err.	0.24429	SO2	N/A
			CO	N/A
			SO	N/A
			S2O	356.35095
Line 5	Center	360.30593	HDO	N/A
	Center Err.	0.06485048	SO2	360.2904
			CO	N/A
			SO	N/A
			S2O	360.29583
Line 6	Center	361.41899	HDO	N/A
	Center Err.	0.0228645	SO2	N/A
			CO	N/A
			SO	361.35111
			S2O	361.67044
Line 7	Center	362.95363	HDO	N/A
	Center Err.	0.0419	SO2	362.96542
			CO	N/A
			SO	N/A
			S2O	362.86675
Line 8	Center	365.7722	HDO	N/A
	Center Err.	0.04519344	SO2	365.7487
			CO	N/A
			SO	N/A
			S2O	365.8681

resolution = 0.168831 GHz

Likely Candidate

Figure 4.22: The details of the observed absorption lines and the theoretical absorption lines of five molecules (Rothman et al., 2013).

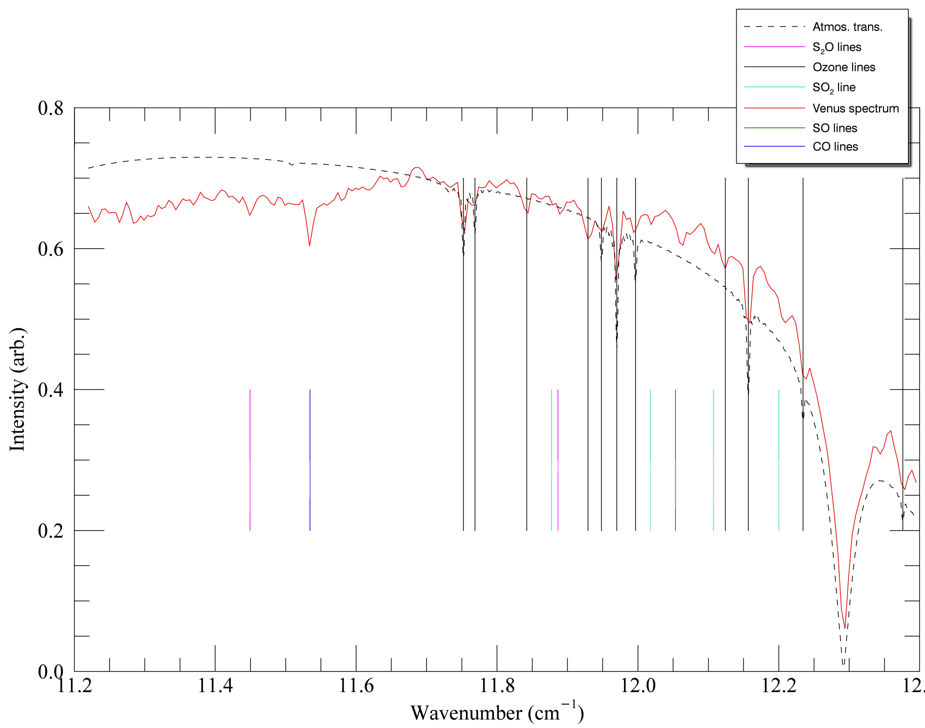

Figure 4.23: The retrieved Venus spectrum (red) normalized to the Earth atmospheric transmission profile (black). The vertical lines are the absorption lines of S_2O, ozone, SO_2, SO and CO, which are thought to match what is seen as absorption lines in the retrieved Venus spectrum of bolometer (14, 26).

Table 4.4: The values of the properties of CO line at 11.53 cm^{-1} at T_0 and P_0

The property	**The value**
Spectral line strength (S_0)	8.28×10^{-23} cm molecules^{-1}
HWHM (α_0)	0.071 cm^{-1} atm^{-1}
Energy of lower level E	11.535 cm^{-1}

4.4.3 Carbon monoxide in the Venusian atmosphere

The carbon monoxide column abundance in the atmosphere of Venus can be calculated using the method shown earlier in determining the ozone and molecular oxygen column abundances in the atmosphere. First, the properties of the absorption line of CO must be obtained from HITRAN, see Table 4.4. Assuming the temperature of CO in the atmosphere of Venus is 160 K (at am altitude of 100 km at solar zenith angle of 60 degrees (Bougher et al., 1986), and the pressure is assumed to be 0.05 mbar (Clancy et al., 2003). Using Equations (4.6 and 4.7), to correct the spectral line strength and the half width at half maximum for temperature and pressure of CO in Venus gives, 2.7×10^{-22} cm molecules^{-1} for spectral line strength and 1.3×10^{-6} cm^{-1} atm^{-1} for the half width at half maximum. Then it was required in order to know whether the strong line or the weak line assumption should be used, the value, where if it is greater than the column abundance, then it is a weak line regime, and if the column abundance is greater it is a strong line regime. In the weak line regime the relation between equivalent width and the column abundance is given by Equation 4.5 while in the strong line regime the relation is given by Equation 4.8, so there is a critical point where

$$\frac{4\alpha}{S_{T,P}} = 9.6 \times 10^{16} \qquad \text{(molecules cm}^{-2}\text{)} \tag{4.10}$$

The column abundance of carbon monoxide is 2.8×10^{20} cm^{-2} (Yung & DeMore, 1982), thus the CO line at 11.53 cm^{-1} is in the strong line regime and the strong line assumption can be applied. Using FTfitter to obtain the equivalent width, see Figure 4.24,

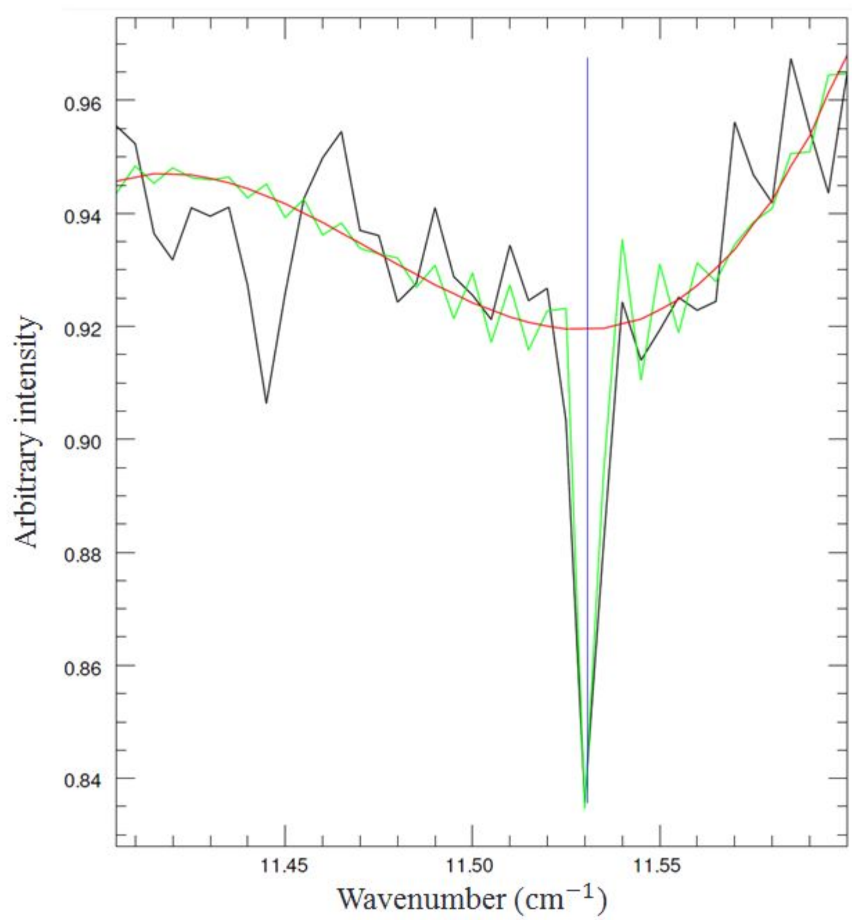

Figure 4.24: Using FTfitter gui, an IDL program written by Brad Gom, to measure the equivalent width of spectral lines, and here we show how it is used on the carbon monoxide line, where the blue line denotes the centre of the absorption line, the red line is the continuum, the black is the spectrum, and the green is fitted to the absorption line

the equivalent width is $1.2 \pm 0.08 \times 10^{-3}$ cm^{-1}, using Equation 4.8, the column abundance of CO was found to be $1.9 \pm 0.3 \times 10^{20}$ molecules cm^{-2}, which agrees with values predicted by the model, taking into account that 30% of Venus facing the Earth was at night and the CO abundance varies by a factor of 2 to 4 (Clancy, 1983).

Although we had access to limited data from one bolometer, which only sampled a quarter of the energy coming from Venus, with a 30 s observation of Venus in a gibbous phase during poor atmospheric conditions, we were able to validate the amount of ozone in the Earth's atmosphere, which only previously has been obtained using an observation of the sun. In addition, we also obtained the column abundance of molecular oxygen with a reasonable agreement to the accepted column abundance. Furthermore, this section showed how to determine the CO column abundance in the Venusian atmosphere, with a promise of determining the abundance of other species in other planetary atmospheres, and constructing models of species abundances and mixing ratios.

Chapter 5

Conclusion and Future Work

Despite that over half the energy emitted by the universe falls in the far infra-red spectral range, and the fact that sub-millimetre astronomy provides a wealth of information about the process of star formation in the molecular clouds, sub-millimetre astronomy remains a relatively new field. Due to two principle challenges; first, the generally low transmittance of the atmosphere of Earth, second, the complexity of instrumentation.

This thesis has presented preliminary results obtained from the commissioning of FTS-2, as a Fourier transform spectrometer designed to work in conjunction with the next generation bolometric camera of SCUBA-2. This represents the first time a Fourier transform spectrometer has been coupled with TES bolometers and, as often with applying new technology, a number of unforeseen challenges were encountered, which had to be accounted for.

Unfortunately the JCMT was going through a transition phase to a new ownership, thus data access was limited as the observing time was at a premium. Nonetheless, we were able to identify the key issues and propose potential solutions, and despite having limited data, we were able to obtain an observation of Venus under poor conditions with non-optimal settings. However, by studying one bolometer we have been able to identify the temperature of Venus from fitting to the continuum spectrum, and the abundance of the carbon monoxide in the Venusian atmosphere by its absorption line, for the first time using a ground-based Fourier transform spectrometer. We were also able to use the observation of one planet to validate the column abundance of ozone in the atmosphere of Earth. The quality of the data from a single bolometer, from the thousands that are available, exceeds that of previous measurements of the column abundance of ozone, using a single bolometer observing the sun (Naylor et al., 1981). This simple comparison shows the potential of imaging spectroscopic measurements using FTS-2 and SCUBA-2.

5.1 Future work

This thesis will act as a reference framework for the next steps of the commissioning of FTS-2. In this thesis, we have shown that the flux jumps are the most significant challenge. While it has been shown their occurrence has been reduced through biasing the settings of SCUBA-2 bolometers, the situation can be further improved by optimizing the bias settings. Furthermore, second area that will be addressed, in the coming months, is the slight imbalance between the input ports of FTS-2. Recently, a process is in place for transferring the JCMT to the University of Hawaii ownership on 31st January 2015, at which point it will be operated by a new entity called the East Asian Observatory, who have expressed an interest in completing the commissioning of FTS-2. The work presented in this thesis will provide the baseline for the continued commissioning of the spectrometer.

Appendix A

Physical constants

Some physical constant	The value	The units
Planck constant (h)	6.626×10^{-34}	$\mathrm{J \cdot s}$
Speed of light (c)	2.998×10^{10}	$\mathrm{cm \cdot s^{-1}}$
Dirac constant ($\hbar$)	1.055×10^{-34}	$\mathrm{J \cdot s}$
Boltzmann constant (k)	1.381×10^{-23}	$\mathrm{J \cdot K^{-1}}$
	0.695	$\mathrm{cm^{-1}K^{-1}}$

Bibliography

Abazajian K., Arnold K., Austermann J., Benson B., Bischoff C., Bock J., Bond J., Borrill J., Calabrese E., Carlstrom J., et al., 2013, arXiv preprint arXiv:1309.5383

Andrews D., Brucksch Jr W., Ziegler W., Blanchard E., 1942, Review of Scientific Instruments, 13, 281

Basilevsky A. T., Head J. W., 2003, Reports on Progress in Physics, 66, 1699

Bastien P., Bissonnette E., Simon A., Coudé S., Ade P., Savini G., Pisano G., Leclerc M., Bernier S., Landry J., et al., 2011, in Astronomical Society of the Pacific Conference Series Vol. 449, Pol-2: The scuba-2 polarimeter. p. 68

Bougher S., Dickinson R., Ridley E., Roble R. G., Nagy A. F., Cravens T. E., 1986, Icarus, 68, 284

Chapman I., Naylor D., Gom B., Querel R., Davis-Imhof P.,

Chapman I. M., 2003, Master's thesis, University of Lethbridge

Clancy R., Sandor B., Moriarty-Schieven G., 2003, Icarus, 161, 1

Clancy R. T., 1983, PhD thesis, California Institute of Technology

Clarke J., 1993, in , The new superconducting electronics. Springer, pp 123–180

Cooper L. N., 1956

Dempsey J. T., Holland W. S., Chrysostomou A., Berry D. S., Bintley D., Chapin E. L., Craig S. C., Coulson I. M., Davis G. R., Friberg P., et al., 2012, in SPIE Astronomical Telescopes+ Instrumentation A new era of wide-field submillimetre imaging: on-sky performance of scuba-2. pp 845202–845202

Economou F., Jenness T., Cavanagh B., Adamson A., Allan A., 2006, Astronomische Nachrichten, 327, 788

Engelberg S., 2006, Random signals and noise: a mathematical introduction. CRC Press

Ephemeris, An almanac of the daily motions of the planets and stars, 'http://www.ephemeris.com/ephemeris.php'

Esposito L., Knollenberg R., MAROV M., Toon O., TURCO R., 1983, Venus, 1, 484

Flynn L. E., Homstein J., Hilsenrath E., 2004, in Geoscience and Remote Sensing Symposium, 2004. IGARSS'04. Proceedings. 2004 IEEE International Vol. 1, The ozone mapping and profiler suite (omps)

Foley C., Keene M., ter Brake H., Vrba J., , 2004, Squid system issues The SQUID Handbook ed J Clarke and AI Braginski

French A. P., Taylor E. F., 1979, An introduction to quantum physics. CRC Press

Gaisser T. K., 1990, Cosmic rays and particle physics. Cambridge University Press

Gom B. G., Naylor D. A., 2004, in Astronomical Telescopes and Instrumentation An update on the imaging fourier transform spectrometer for scuba-2. pp 695–704

Güsten R., Booth R., Cesarsky C., Menten K., Agurto C., Anciaux M., Azagra F., Belitsky V., Belloche A., Bergman P., et al., 2006, in Astronomical Telescopes and Instrumentation Apex: the atacama pathfinder experiment. pp 626714–626714

Holland W., Ade P., Griffin M., Hepburn I., Vickers D., Cunningham C., Hastings P., Gear W., Duncan W., Baillie T., et al., 1996, International journal of infrared and millimeter waves, 17, 669

Holland W., Bintley D., Chapin E., Chrysostomou A., Davis G., Dempsey J., Duncan W., Fich M., Friberg P., Halpern M., et al., 2013, Monthly Notices of the Royal Astronomical Society, 430, 2513

Holland W., MacIntosh M., Fairley A., Kelly D., Montgomery D., Gostick D., Atad-Ettedgui E., Ellis M., Robson I., Hollister M., et al., 2006, in Astronomical Telescopes and Instrumentation Scuba-2: a 10,000-pixel submillimeter camera for the james clerk maxwell telescope. pp 62751E–62751E

Holland W. S., Cunningham C. R., Gear W. K., Jenness T., Laidlaw K., Lightfoot J. F., Robson E., 1998, in Astronomical Telescopes & Instrumentation Scuba: a submillimeter camera operating on the james clerk maxwell telescope. pp 305–318

Holland W. S., Duncan W., Kelly B., Irwin K. D., Walton A. J., Ade P. A., Robson E., 2003, in Astronomical Telescopes and Instrumentation Scuba-2: a large-format submillimeter camera on the james clerk maxwell telescope. pp 1–18

Holland W. S., Robson E., Gear W. K., Cunningham C. R., Lightfoot J. F., Jenness T., Ivison R. J., Stevens J. A., Ade P. A., Griffin M., et al., 1999, Monthly Notices of the Royal Astronomical Society, 303, 659

Houghton J., 2002, The physics of atmospheres. Cambridge University Press

Houghton J. T., 1986, The Physics of Atmospheres. Cambridge University Press

Irwin K., Hilton G., 2005a, Topics Appl. Phys, 99, 63

Irwin K., Hilton G., 2005b, in , Cryogenic Particle Detection. Springer, pp 63–150

JAC, The filters profile of SCUBA-2 from the Joint Astronomy Centre, 'http://www.jach.hawaii.edu/JCMT/continuum/scuba2/filter/'

JAC, The image gallery of the Joint Astronomy Centre, 'http://outreach.jach.hawaii.edu/gallery/'

JAC, An image of the SCUBA-2 sub-arrays from the Joint Astronomy Centre, 'http://www.jach.hawaii.edu/JCMT/continuum/scuba2/scuba2_obsmodes.html'

Jacquinet-Husson N., Scott N., Chedin A., Bonnet B., Barbe A., Tyuterev V. G., Champion J., Winnewisser M., Brown L., Gamache R., et al., 1998, Journal of Quantitative Spectroscopy and Radiative Transfer, 59, 511

Johnstone D., 2013, in Protostars and Planets VI, Heidelberg, July 15-20, 2013. Poster# 1S003 Vol. 1, Jcmt in the post-herschel era of alma

Johnstone D., Bally J., 1999, The Astrophysical Journal Letters, 510, L49

Jones S. C., 2010, Master's thesis, University of Lethbridge, Dept. of Physics & Astronomy

JPL, Geocentric ephemeris for Venus from the Jet Propulsion Laboratory Development, 'http://astropixels.com/ephemeris/planets/venus2013.html'

Kutner M. L., 2003, Astronomy: A physical perspective. Cambridge University Press

Laird-Technologies, Eccosorb AN72, 'http://www.eccosorb.com/products-eccosorb-an.htm'

Lee A. T., Richards P. L., Nam S. W., Cabrera B., Irwin K., 1996, Applied Physics Letters, 69, 1801

Mcclung D., , 2003, Historical astronomy concepts, 'http://www.themcclungs.net/astronomy/concepts/ptolemywrong.html'

Melnick G. J., Stauffer J. R., Ashby M. L., Bergin E. A., Chin G., Erickson N. R., Goldsmith P. F., Harwit M., Howe J. E., Kleiner S. C., et al., 2000, The Astrophysical Journal Letters, 539, L77

MicroWorlds, The electromagnetic spectrum, http://www2.lbl.gov/MicroWorlds/ALSTool/EMSpec/EMSpec2.html

Mills F. P., Esposito L. W., Yung Y. L., 2007, Exploring Venus as a Terrestrial Planet, pp 73–100

Murdin P., 2000, Encyclopedia of Astronomy and Astrophysics, 1, 4160

Nave C. R., , 2012, 'http://hyperphysics.phy-astr.gsu.edu/hbase/astro/cosmic.html'

Naylor D., Clark T., Boreiko R., 1981, Infrared Physics, 21, 271

Naylor D. A., Gom B. G., van der Wiel M. H., Makiwa G., 2013, Canadian Journal of Physics, 91, 870

Naylor D. A., Gom B. G., Zhang B., 2006, in Astronomical Telescopes and Instrumentation Preliminary design of fts-2: an imaging fourier transform spectrometer for scuba-2. pp 62751Z–62751Z

Noel D., , 2012, The change in temperature and pressure with the altitude in the Venusian atmsophere, 'http://www.aoi.com.au/bcw/EarthTemp/'

Pascale E., Ade P., Bock J., Chapin E., Chung J., Devlin M., Dicker S., Griffin M., Gundersen J., Halpern M., et al., 2008, The Astrophysical Journal, 681, 400

Pickett H., Poynter R., Cohen E., Delitsky M., Pearson J., Müller H., 1998, Journal of Quantitative Spectroscopy and Radiative Transfer, 60, 883

Pilbratt G., Riedinger J., Passvogel T., Crone G., Doyle D., Gageur U., Heras A., Jewell C., Metcalfe L., Ott S., et al., 2010, arXiv preprint arXiv:1005.5331

Rieke M., , 2002, 'http://ircamera.as.arizona.edu/astr_250/Lectures/Lecture_15.htm'

Rogalski A., 2010, Infrared detectors. CRC Press

Rothman L., Gordon I., Babikov Y., Barbe A., Chris Benner D., Bernath P., Birk M., Bizzocchi L., Boudon V., Brown L., et al., 2013, Journal of Quantitative Spectroscopy and Radiative Transfer, 130, 4

Rothman L. S., Rinsland C., Goldman A., Massie S., Edwards D., Flaud J., Perrin A., Camy-Peyret C., Dana V., Mandin J.-Y., et al., 1998, Journal of Quantitative Spectroscopy and Radiative Transfer, 60, 665

Seinfeld J. H., Pandis S. N., 2012, Atmospheric chemistry and physics: from air pollution to climate change. John Wiley & Sons

Smith H., Buckle J., Hills R., Bell G., Richer J., Curtis E., Withington S., Leech J., Williamson R., Dent W., et al., 2008, in SPIE Astronomical Telescopes+ Instrumentation Harp: a submillimetre heterodyne array receiver operating on the james clerk maxwell telescope. pp 70200Z–70200Z

Stark A. A., Bally J., Balm S. P., Bania T., Bolatto A. D., Chamberlin R. A., Engargiola G., Huang M., Ingalls J. G., Jacobs K., et al., 2001, Publications of the Astronomical Society of the Pacific, 113, 567

Starr C., Evers C., Starr L., 2010, Biology: Concepts and Applications Without Physiology. Cengage Learning

Svedhem H., Titov D. V., Taylor F. W., Witasse O., 2007, Nature, 450, 629

Tremblin P., Schneider N., Minier V., Durand G. A., Urban J., 2012, Astronomy and Astrophysics, 548, 65

Turner J., 2006, IAU Special Session, 1, 1

Wikimedia, Atmospheric electromagnetic transmittance or opacity, 'http://commons.wikimedia.org/wiki/File:Atmospheric_electromagnetic_transmittance_or_opacity.jpg'

Wikimedia, Voltage flux curve, 'http://en.wikipedia.org/wiki/Scanning_SQUID_microscope'

Wikipedia, A schematic of a TES bolometer, 'http://en.wikipedia.org/wiki/File:TES_schematic.pdf'

Wolfram—Alpha, 2014, Venus location at 2013-08-14, 'http://www.wolframalpha.com/input/?i=venus+at+2013%2F08%2F14'

Young E., Becklin E., Marcum P., Roellig T., De Buizer J., Herter T., Güsten R., Dunham E., Temi P., Andersson B.-G., et al., 2012, The Astrophysical Journal Letters, 749, L17

Yung Y. L., DeMore W., 1982, Icarus, 51, 199

Zhang X., Liang M. C., Mills F. P., Belyaev D. A., Yung Y. L., 2012, Icarus, 217, 714